Computational Fluid Dynamics Assessment of Laminar-Turbulent Boundary Layer Transition and its Application to Rotorcraft

A Thesis presented for the

Master of Science

Degree

The University of Tennessee, Knoxville

Jared Alexander Carnes

May 2020

© by Jared Alexander Carnes, 2020
All Rights Reserved.

Acknowledgments

I would like to thank Dr. James Coder for the opportunity to work on this project. His programming skills and knowledge of CFD and transition modeling have proved integral to this work as a whole. I would also like to thank Dr. Kivanc Ekici, Dr. Ryan Glasby, and Dr. Devina Sanjaya for serving on my thesis committee and providing invaluable feedback and insight.

Special thanks go to Dr. Pieter Buning for serving as technical monitor on this project and his feedback throughout this work, along with his advice and expertise in running OVERFLOW. Additional thanks go to Mark Potsdam for his comments and suggestions from the VLRCOE yearly reviews.

I would like to thank my friends and co-workers in the volAIR lab for their support and light-hearted attitude. Thanks go to my family for pushing me to pursue and obtain my master's degree.

Finally, I would like to thank the AIAA Applied Aerodynamics Technical Committee's CFD Transition Modeling Discussion Group, the AIAA Applied Aerodynamics Technical Committee's Rotorcraft Simulations and Performance Predictions discussion group, and Ashwin Parwani for providing the grids for this work.

This research was partially funded by the Government under Agreement No. W911W6-17-2-0003. The U.S. Government is authorized to reproduce and distribute reprints for Government purposes notwithstanding any copyright notation thereon. The views and conclusions contained in this document are those of the authors and should not be interpreted as representing the official policies, either expressed or implied, of the Aviation Development Directorate or the U.S Government.

Abstract

The Amplification Factor Transport (AFT) transition modeling framework has been modified to include an algebraic model to account for crossflow transition. The effect of crossflow transition modeling is assessed for two rotors in hovering flight and on a rotor-fuselage system in forward flight conditions. Hover predictions for the S-76 and PSP rotor and forward flight predictions for the PSP-ROBIN system are made using computational fluid dynamics (CFD). Solutions were obtained using OVERLFOW 2.2n, a structured grid, overset, Reynolds-averaged Navier-Stokes (RANS) CFD solver developed by NASA. A hybrid RANS/LES methodology is used in order to more accurately capture off-body structures and turbulent scales. Grid generation and computational methods are described. Simulations were performed using a fully turbulent model, a transition model without crossflow, and a transition model with crossflow modeling enabled. Performance predictions and transition locations are qualitatively and quantitatively compared to results from experiments. Additional analyses include wake vortex structure examination, sectional loading, and integrated force and moment coefficient comparisons. For the S-76 rotor in hover, the transition model with crossflow showed early transition on the lower surface due to a blade-vortex interaction (BVI). When using the transition model without crossflow, BVI did not greatly affect predicted transition. Predicted rotor figure of merit for the PSP rotor in hover correlated well with experiments for both transition models. Thrust was overpredicted for the PSP-ROBIN system in forward flight; however, predicted transition locations showed good agreement with experiments.

Table of Contents

Chapter 1 Introduction **1**

1.1 Research Goals 6

Chapter 2 Background **8**

2.1 Early Aerodynamic Methods for Rotorcraft 8

2.1.1 Blade Element Momentum Theory 10

2.1.2 Blade Element Momentum Theory for Forward Flight 11

2.2 Early Rotorcraft CFD Techniques 12

2.2.1 More Complex CFD Methods 13

2.2.2 Navier-Stokes CFD Methods 15

2.3 RANS-based Turbulence Closure 20

2.3.1 Zero-equation Turbulence Closure Models 20

2.3.2 One-equation Turbulence Closure Models 21

2.3.3 Two-equation Turbulence Closure Models 23

2.3.4 Other Turbulence Closure Models 24

2.4 Developments in CFD-Compatible Transition Modeling 25

2.4.1 CFD-Compatible Transition Modeling 27

2.4.2 Crossflow Transition Modeling 29

2.5 Contemporary Fully Turbulent and Transitional Rotorcraft Simulations 31

2.5.1 S-76 Rotor in Hover 31

2.5.2 PSP Rotor in Hover 33

2.5.3 Forward Flight and CFD-CSD Coupling 35

Chapter 3 Experiments and Validation Cases **38**

3.1 Rotorcraft Experimental Tests 38

3.1.1 The Pressure Sensitive Paint Rotor Experiments 38

3.1.2 The S-76 Rotor Experiments 41

3.2 Crossflow Validation Test Cases 42

3.2.1 NLF(2)-0415 Infinite Swept Wing 42

3.2.2 6:1 Inclined Prolate Spheroid 42

3.2.3 TU Braunschweig Sickle Wing 43

Chapter 4 Computational Methodology **44**

4.1 Governing Equations 44

4.1.1 WENO Flux Reconstruction 46

4.1.2 Roe Flux-Difference Splitting 48

4.1.3 Diagonalized Diagonal Dominant Alternating Direction Implicit (D3ADI) Scheme 49

4.2 Turbulence Closure 50

4.2.1 Spalart-Allmaras Eddy Viscosity Model 50

4.2.2 Amplification Factor Transport Model 53

4.2.3 Crossflow Transition Modeling 56

4.2.4 Hybrid RANS/LES Framework 58

4.3 Geometries and Grid Generation 59

4.3.1 Isolated PSP Grid System in Hover 60

4.3.2 PSP-ROBIN Grid System in Forward Flight 62

4.3.3 Isolated S-76 Grid System in Hover 64

4.3.4 NLF(2)-0415 Infinite Swept Wing 67

4.3.5 6:1 Inclined Prolate Spheroid 68

4.3.6 TU Braunschweig Sickle Wing 68

4.4 Boundary Conditions 70

4.5 Post-processing 71

4.5.1 Proper Orthogonal Decomposition 71

Chapter 5 Results **73**

5.1 Crossflow Model Validation 73

5.1.1 NLF(2)-0415 Infinite Swept Wing 73

5.1.2 6:1 Inclined Prolate Spheroid 74

5.1.3 TU Braunschweig Sickle Wing 76

5.2 Isolated S-76 Rotor in Hover 79

5.3 Isolated PSP Rotor in Hover 92

5.4 PSP-ROBIN in Forward Flight 116

Chapter 6 Conclusions **134**

References **138**

Vita **151**

List of Tables

4.1 PSP rotor geometric properties 60
4.2 S-76 rotor geometric properties 65
5.1 TU Braunschweig sickle wing test parameters 76
5.2 S-76 rotor predicted performance in hover 82
5.3 PSP rotor predicted performance in hover 94
5.4 Summary of unsteady boundary layer transition investigation methods 101
5.5 PSP-ROBIN forward flight rotor trim variables 116
5.6 PSP rotor predicted performance in forward flight 118

List of Figures

1.1 Sikorsky R-4 in hovering flight 2
1.2 Rotor disk flowfield in forward flight 3
1.3 Experimentally measured PSP hover performance 5
2.1 Rotor wake with a near-body finite difference grid 14
2.2 Rotor blade-vortex interaction in forward flight 17
2.3 Predicted wake structure of a rotor in hover using TURNS 18
2.4 Overset grid system for the MD 30P/30N airfoil 19
2.5 Boundary layer profiles on a solid wall 26
2.6 3-D boundary layer on a swept wing 29
2.7 Sectional thrust as a function of blade radius for $M_{tip} = 0.65$ 32
2.8 Wake structure of the PSP rotor with ROBIN fuselage in hover visualized via isosurfaces of the Q-criterion, $C_T/\sigma = 0.085$, $M_{tip} = 0.58$ 33
2.9 Wake structure of the PSP rotor in hover using 2nd order and 4th order flux reconstruction 35
2.10 Sectional thrust versus azimuth at r/R = 0.97 predicted using coupled CFD-CSD for the AH-1G rotor 37
3.1 PSP hover test schematic 39
3.2 PSP-ROBIN experimental setup for forward flight 40
3.3 S-76 advanced tip geometries used in testing 41
3.4 TU Braunschweig sickle wing planform 43
4.1 PSP rotor blade planform 60
4.2 PSP blade near-body, structured, overset grid system 61
4.3 PSP off-body, Cartesian, overset grid system 62
4.4 ROBIN mod7 near-body, structured, overset grid system 63

4.5 PSP-ROBIN off-body, Cartesian, overset grid system 64
4.6 S-76 rotor blade planform 65
4.7 S-76 hub near-body, structured, overset grid system 66
4.8 S-76 rotor blade near-body, structured, overset grid system 66
4.9 S-76 off-body, Cartesian, overset grid system 67
4.10 NLF(2)-415 infinite swept wing structured grid 68
4.11 6:1 inclined prolate spheroid structured grid 69
4.12 TU Braunschweig sickle wing near-body, structured, overset grid system 70
5.1 Predicted transition locations on the upper surface of the NLF(2)-0415 wing 74
5.2 Predicted transition locations using AFT2019b+CF on the 6:1 inclined prolate spheroid at $Re = 6.5$ x 10^6, $M_\infty = 0.13$ 75
5.3 Predicted transition locations for Case A using AFT2019b+CF on the TU Braunschweig sickle wing 77
5.4 Predicted transition locations for Case B using AFT2019b+CF on the TU Braunschweig sickle wing 77
5.5 Predicted transition locations for Case C using AFT2019b+CF on the TU Braunschweig sickle wing 78
5.6 Predicted transition locations for Case D using AFT2019b+CF on the TU Braunschweig sickle wing 78
5.7 Thrust and torque history for the S-76 rotor using AFT2019b, θ_0 = 10° 80
5.8 Residual history for the S-76 rotor using AFT2019b, θ_0 = 10° 80
5.9 Comparison of thrust as a function of collective pitch for the S-76 rotor 82
5.10 Comparison of torque as a function of collective pitch for the S-76 rotor 83
5.11 Comparison of figure of merit as a function of thrust level for the S-76 rotor 83
5.12 Instantaneous predicted transition locations using AFT2019b on the S-76 rotor, $\theta_0 = 6°$ 85
5.13 Instantaneous predicted transition locations using AFT2019b+CF on the S-76 rotor, $\theta_0 = 6°$ 85
5.14 Instantaneous predicted transition locations using AFT2019b on the S-76 rotor, $\theta_0 = 10°$ 86

5.15 Instantaneous predicted transition locations using AFT2019b+CF on the S-76 rotor, $\theta_0 = 10°$ 86
5.16 Digitized instantaneous transition locations on the S-76 rotor 87
5.17 Contours of vorticity magnitude on the y = 0 plane using SA-neg-RC on the S-76 rotor, $\theta_0 = 10°$ 89
5.18 Contours of vorticity magnitude on the y = 0 plane using AFT2019b on the S-76 rotor, $\theta_0 = 10°$ 89
5.19 Contours of vorticity magnitude on the y = 0 plane using AFT2019b+CF on the S-76 rotor, $\theta_0 = 10°$ 90
5.20 Isosurfaces of the Q-criterion = 0.00009 using SA-neg-RC on the S-76 rotor, $\theta_0 = 10°$ 90
5.21 Isosurfaces of the Q-criterion = 0.00009 using AFT2019b on the S-76 rotor, $\theta_0 = 10°$ 91
5.22 Isosurfaces of the Q-criterion = 0.00009 using AFT2019b+CF on the S-76 rotor, $\theta_0 = 10°$ 91
5.23 Thrust and torque history for the PSP rotor using AFT2019b+CF, θ_0 = 6° 93
5.24 Residual history for the PSP rotor using AFT2019b+CF, θ_0 = 6° 93
5.25 Comparison of figure of merit as a function of thrust level for the PSP rotor 95
5.26 Instantaneous predicted transition locations using AFT2019b on the PSP rotor, $\theta_0 = 6°$ 97
5.27 Instantaneous predicted transition locations using AFT2019b+CF on the PSP rotor, $\theta_0 = 6°$ 97
5.28 Instantaneous predicted transition locations using AFT2019b on the PSP rotor, $\theta_0 = 10°$ 98
5.29 Instantaneous predicted transition locations using AFT2019b+CF on the PSP rotor, $\theta_0 = 10°$ 98
5.30 Digitized instantaneous transition locations on the PSP rotor 99
5.31 Comparison of unsteady transition detection techniques using AFT2019b on the PSP rotor, θ_0 = 6°, upper surface 103
5.32 Comparison of unsteady transition detection techniques using AFT2019b on the PSP rotor, θ_0 = 6°, lower surface 104

5.33 Comparison of unsteady transition detection techniques using AFT2019b+CF on the PSP rotor, θ_0 = 6°, upper surface . . . 106
5.34 Comparison of unsteady transition detection techniques using AFT2019b+CF on the PSP rotor, θ_0 = 6°, lower surface . . . 107
5.35 Comparison of unsteady transition detection techniques using AFT2019b on the PSP rotor, θ_0 = 10°, upper surface . . . 108
5.36 Comparison of unsteady transition detection techniques using AFT2019b on the PSP rotor, θ_0 = 10°, lower surface . . . 109
5.37 Comparison of unsteady transition detection techniques using AFT2019b+CF on the PSP rotor, θ_0 = 10°, upper surface . . . 110
5.38 Comparison of unsteady transition detection techniques using AFT2019b+CF on the PSP rotor, θ_0 = 10°, lower surface . . . 111
5.39 Contours of vorticity magnitude on the y = 0 plane using SA-neg-RC on the PSP rotor, $\theta_0 = 10°$ . . . 112
5.40 Contours of vorticity magnitude on the y = 0 plane using AFT2019b on the PSP rotor, $\theta_0 = 10°$ . . . 113
5.41 Contours of vorticity magnitude on the y = 0 plane using AFT2019b+CF on the PSP rotor, $\theta_0 = 10°$ . . . 113
5.42 Isosurfaces of the Q-criterion = 0.00009 using SA-neg-RC on the PSP rotor, $\theta_0 = 10°$ 114
5.43 Isosurfaces of the Q-criterion = 0.00009 using AFT2019b on the PSP rotor, $\theta_0 = 10°$ 114
5.44 Isosurfaces of the Q-criterion = 0.00009 using AFT2019b+CF on the PSP rotor, $\theta_0 = 10°$ . . . 115
5.45 Thrust history for the PSP-ROBIN in forward flight . . . 117
5.46 Torque history for the PSP-ROBIN in forward flight . . . 118
5.47 Residual history for the PSP-ROBIN in forward flight using AFT2019b+CF, ROBIN only . . . 119
5.48 Residual history for the PSP-ROBIN in forward flight using AFT2019b+CF, PSP only . . . 120
5.49 Instantaneous predicted transition locations using AFT2019 on the PSP rotor in forward flight, $\psi = 90°$ . . . 121

5.50 Instantaneous predicted transition locations using AFT2019b+CF on the PSP rotor in forward flight, $\psi = 90°$ . . . 121
5.51 Instantaneous predicted transition locations using AFT2019 on the PSP rotor in forward flight, $\psi = 150°$ . . . 122
5.52 Instantaneous predicted transition locations using AFT2019b+CF on the PSP rotor in forward flight, $\psi = 150°$ . . . 122
5.53 Instantaneous predicted transition locations using AFT2019 on the PSP rotor in forward flight, $\psi = 315°$ . . . 123
5.54 Instantaneous predicted transition locations using AFT2019b+CF on the PSP rotor in forward flight, $\psi = 315°$ . . . 123
5.55 Digitized instantaneous transition locations on the PSP rotor in forward flight . . . 125
5.56 Sectional thrust for the PSP-ROBIN in forward flight using SA-neg-RC . . . 127
5.57 Sectional thrust for the PSP-ROBIN in forward flight using AFT2019 . . . 127
5.58 Sectional thrust for the PSP-ROBIN in forward flight using AFT2019b+CF . . . 128
5.59 Thrust harmonics for the PSP-ROBIN in forward flight . . . 128
5.60 Sectional torque for the PSP-ROBIN in forward flight using SA-neg-RC . . . 129
5.61 Sectional torque for the PSP-ROBIN in forward flight using AFT2019 . . . 130
5.62 Sectional torque for the PSP-ROBIN in forward flight using AFT2019b+CF . . . 130
5.63 Torque harmonics for the PSP-ROBIN in forward flight . . . 131
5.64 Isosurfaces of the Q-criterion = 0.00005 using AFT2019b+CF on the PSP-ROBIN in forward flight, revolution 5.5 . . . 132
5.65 Isosurfaces of the Q-criterion = 0.00005 using AFT2019b+CF on the PSP-ROBIN in forward flight, revolution 6.0 . . . 133

Nomenclature

C_l	=	sectional lift coefficient
C_Q, C_P	=	rotor torque coefficient
C_T	=	rotor thrust coefficient
c	=	chord length
d	=	wall distance
e_0	=	total energy
h_0	=	total enthalpy
FM	=	figure of merit
k	=	turbulent kinetic energy
M_{tip}	=	rotor tip Mach number
N_b	=	number of blades
$\tilde{n}$	=	amplification factor
P	=	pressure
R	=	rotor radius
r	=	radial location
Re	=	Reynolds number based on chord length
Re_{SCF}	=	stationary crossflow Reynolds number
Re_θ	=	momentum thickness Reynolds number
$Re_{\theta c}$	=	critical momentum thickness Reynolds number
S	=	strain rate
u	=	velocity
α	=	angle of attack

γ	=	intermittency
$\tilde{\gamma}$	=	modified intermittency
ϵ	=	specific turbulent diffusion
θ_o	=	rotor collective pitch
λ	=	inflow ratio, Stokes' hypothesis
μ_t	=	eddy viscosity
ν_t	=	eddy viscosity
$\tilde{\nu}$	=	modified eddy viscosity
ρ	=	density
σ	=	rotor solidity
τ	=	shear stress
Ω	=	vorticity
ω	=	specific turbulence dissipation rate

Chapter 1: Introduction

A helicopter can be defined as a vehicle that uses rotating wings to produce vertical lift, propulsion, and control forces [1]. Such vehicles are capable of purely vertical take-off and lift (VTOL). When helicopters and rotary-wing aircraft are operating in VTOL mode, the vehicle can climb, descend, or hover, depending on the difference between the lift produced and the weight of the vehicle. Full six degree-of-freedom motion of the vehicle can be achieved by moving a series of pilot controls which can vary power, change the collective pitch of the rotor blades, and change the cyclic pitch of the rotor blades. By tilting the rotor toward the nose of the fuselage or away from the nose of the fuselage, the vehicle can fly forward or backward, respectively. Changing the pitch of the rotor via the collective or cyclic control can induce roll moments and yaw moments to aid in maneuverability. In operation, the rotor produces a torque in the opposite direction of rotation, which must be balanced by a tail rotor or an additional rotor rotating in the opposite direction. This requires additional power available to the rotor and increases its mechanical complexity. Tail rotors can provide directional stability in forward flight and can also be used as a source of yaw moment in order to re-orient the vehicle. Such maneuverability and VTOL capabilities have made helicopters and rotary-wing aircraft attractive for quick-response medical rescue, civilian commuting and transport, and military applications [1]. One of the first widespread usages of a helicopter was with the Sikorsky R-4, shown in Fig. 1.1. The Sikorsky R-4 was the first mass-produced helicopter, primarily used by the United States military and the United Kingdom military as a supply transport and rescue craft in the pacific theater of World War II. The R-4 featured a pilot seat, a passenger seat, a three-bladed rotor, and a tail rotor.

While rotating wings are especially useful in their VTOL capabilities, they are penalized in forward flight operation. Forward speed is not only limited by rotor drag and fuselage drag, but is also limited by compressibility effects on the rotor blade. On the advancing side of the rotor disk, where the oncoming blade advances into the freestream, the relative velocity of the blade increases



Fig. 1.1 Sikorsky R-4 in hovering flight [2]

and the local Mach number may exceed the drag divergence Mach number at regions near the blade tip, as shown in Fig. 1.2. This can result in large increases in drag, power required, and loss of lift for the advancing side of the rotor disk. Additionally, to maintain steady, level flight, the blades must be pitched cyclically, such that the advancing blade has a lower pitch angle than does the retreating blade. This is needed in order to compensate for the varying local Mach number in forward flight on each side of the rotor disk, The pilot must be attentive to the collective pitch and cyclic pitch controls in forward flight in order to prevent unintended attitude changes.

Accurate aerodynamic prediction of rotorcraft is difficult due to the complex flowfield in which they operate. In hover, the rotor operates in its own wake, and downwash from the rotor can move back up through the rotor disk with the presence of a fuselage or a solid surface below the rotor, such as during operation in ground effect [4]. The ability to predict the wake structure greatly affects the ability to predict rotor torque, as the wake is the primary determinant of rotor torque required. Traditionally, the wake can be predicted through empirical methods used to describe the wake, or basic vortex-filament analyses. These methods are often useful as a “first pass” in wake

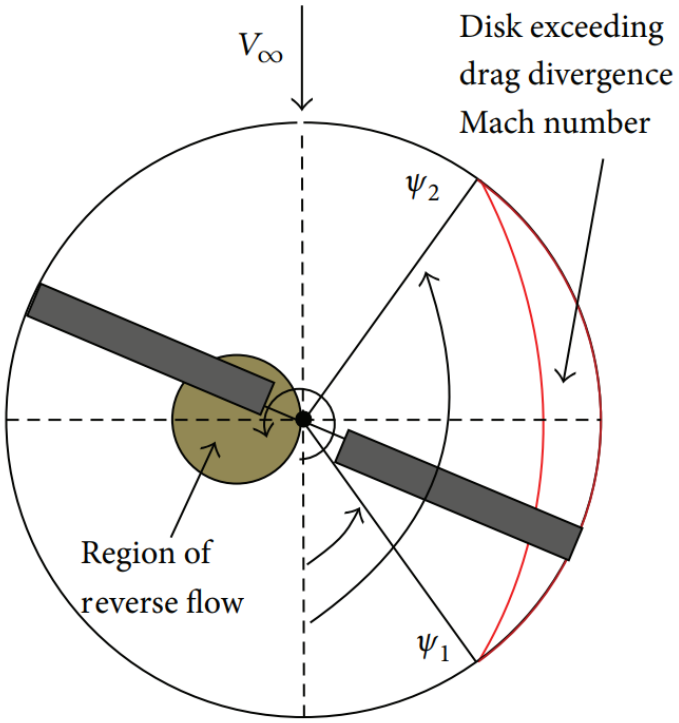


Fig. 1.2 Rotor disk flowfield in forward flight [3]

analysis, but have difficulties in predicting vortex diffusion and growth, along with other Reynolds number effects [1]. In forward flight, capturing the wake structure is not as important as the wake is convected downstream away from the rotor by the freestream velocity. However, for low advance ratios (i.e. the ratio of forward speed to tip speed), the young-age wake structure must be well predicted as blade-vortex interactions can occur, which makes difficult the prediction of vibratory loads and acoustic noise.

Many of these momentum-based, first-principles type phenomena can be predicted using inviscid aerodynamic methods. These inviscid methods unfortunately cannot account for viscous effects such as boundary layer transition and shear layers, which can lead to errant performance prediction [5]. Prediction of laminar and turbulent flow, dynamic stall effects, and rotor and fuselage drag effects are all viscous phenomena which require more complex computational fluid dynamics (CFD) methods. Contemporary CFD methods often use the full Navier-Stokes equations

to perform simulations. Full Navier-Stokes simulations were initially not tractable for rotorcraft flows, as the complex flowfield requires fine grid resolution in regions near the blades and also away from the blades in order to resolve wakes. This requirement in grid resolution made Navier-Stokes methods very expensive to compute, largely as a function of computing technology but also due to immature numerical methods. Thus, quicker, but more simplified, methods such as blade element momentum theory, vortex wake models, lifting line methods, potential flow methods, and Euler methods were more appealing and practical. Among these methods, Euler methods proved useful in predicting rotor wakes from a first-principles approach, although it showed difficulties in preserving vorticity, especially in the wake.

The next step from Euler methods came with the use of Navier-Stokes simulations for rotorcraft flows. Although Reynolds-averaged Navier-Stokes (RANS) methods were already in use for fixed-wing flows in the late 1980s to early 1990s, they had not yet been widely adopted for rotorcraft flows as the inherently complex flowfield necessitated significant computational resources. Navier-Stokes simulations, however, prove to be attractive as they can better preserve vorticity, viscous effects can be captured, and the overall solution is computed based on more accurate physics.

Automatically included in the Navier-Stokes equations are viscous effects, which must be computed or modeled throughout the flowfield. In a thin region near the wall, viscosity is the dominant aerodynamic phenomenon. This region can be assumed to contain all viscous effects and is called the boundary layer. The boundary layer is often modeled using a turbulence closure method, which seeks to model the Reynolds stresses of the Navier-Stokes equations in order to produce, destroy, and track viscous effects through the lens of turbulent eddies. Turbulence closure methods generally seek to compute the turbulent kinetic energy and turbulent diffusion or dissipation, or seek to compute a turbulent eddy viscosity that is analogous to molecular viscosity. These variables in turn are used to compute production, destruction, and convection of turbulent structures. Lamentably, turbulence models neglect an important type of boundary layer flows: laminar flow. Laminar flow over an airfoil generally promotes higher lift and less drag [5]. By assuming no turbulent production in the Navier-Stokes equations, the flowfield can be described as fully laminar, but there can be no turbulent flow. Fortunately, there exists an additional subset of turbulence closure methods that seeks to bridge the gap between these two flow regimes: laminar-turbulent boundary layer transition models. These models allow the capturing of laminar boundary

layers by initially assuming the flow is laminar. Then, instabilities in the laminar boundary layer are modeled and can be used to determine when the flow regime transitions from laminar to turbulent.

Experimental studies by Overmeyer and Martin on a rotor in hover [6] have shown that fully turbulent boundary layers exhibit poorer performance in hover than naturally transitioning boundary layers. Plotted in Fig. 1.3 is the hover efficiency (figure of merit, FM) as a function of thrust level. The figure of merit is the ratio of ideal rotor power to actual rotor power. With fully turbulent boundary layers, the measured FM is several counts (0.01) less than a boundary layer that transitions naturally. Thus, for the same thrust level, it follows that an untripped boundary layer requires less power than a fully turbulent boundary layer, meaning the engine need not produce as much power. This can enable increased payload, range, and endurance for the vehicle. The ability to capture and predict this transition phenomenon is then integral to accurately computing performance for rotorcraft.

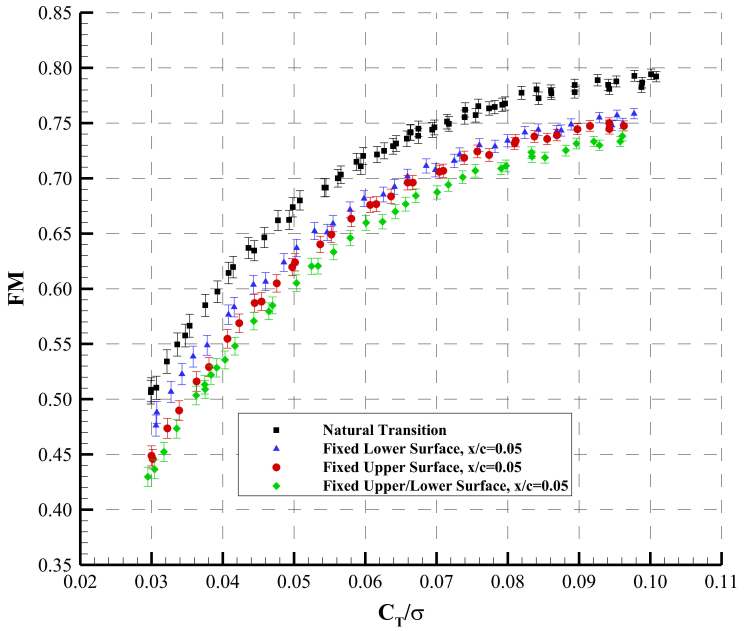


Fig. 1.3 Experimentally measured PSP hover performance [6]

Boundary layer transition can occur via several different modes such as Tollmien-Schlichting instabilities (natural transition), bypass instabilities, separation-induced transition, and crossflow transition [7]. Predicting transition as a function of one of these modes is in and of itself

mathematically complex. The linear stability theory of Smith and Gamberoni [8] is capable of computing transition via several of these modes, but is difficult to apply this theory to CFD methods [9]. Some sate-of-the-art CFD-compatible transition models are capable of predicting Tollmien-Schlichting type transition [10, 11]. Similarly, other models exist that are capable of predicting crossflow transition [7, 12–15] which must be accounted for in flows with high crossflow strength. For rotorcraft in hover, regions near the blade tip can experience strong crossflow due to local sweep and blade-vortex interactions. In forward flight, there is significant crossflow in most regions of the rotor disk, as the blade is not always moving normal relative to the freestream. Therefore, in order to accurately predict boundary layer transition for rotorcraft, it is necessary to account for natural transition and also crossflow transition.

1.1 Research Goals

The present work seeks to investigate the effects of laminar-turbulent transition on predicted rotorcraft performance using a computational fluid dynamics approach. The Amplification Factor Transport (AFT) transition modeling framework [11] is used as a turbulence closure method to make performance predictions and transition predictions for various rotorcraft test cases. In order to account for additional transition physics, the AFT model is modified to include transition induced by stationary crossflow instabilities and is used to make predictions for the same rotorcraft test cases. The primary objectives are summarized as,

1. Integrate a crossflow transition model with the AFT model and validate it for a range of transition test cases.

2. Simulate the S-76 rotor in hover using a fully turbulent model, a transition model, and a transition model with crossflow. Compare predicted performance with experimental results and determine the influence of transition with and without crossflow on the flowfield. The S-76 rotor is a four-bladed rotor for which rotor performance data exist. This rotor has seen widespread use in the CFD community for rotorcraft simulations.

3. Make performance predictions for the PSP rotor in hover using a fully turbulent model, a transition model, and a transition model with crossflow. Quantitatively compare predicted

transition locations with experimentally determined transition cases and discuss the influence of transition modeling on rotor performance. Experimental tests for the PSP rotor include rotor performance data and transition location data, making it a strong test case for rotorcraft CFD validation.

4. Perform simulations of a three-bladed PSP rotor with the ROBIN fuselage in forward flight using a fully turbulent model, a transition model, and a transition model with crossflow. Assess predicted rotor performance and transition locations as compared with experimentally reported data. Additionally, investigate the effects of each turbulence closure method on aerodynamic loading harmonics and blade sectional loading.

Chapter 2: Background

2.1 Early Aerodynamic Methods for Rotorcraft

The ability to predict the aerodynamic performance of a given rotor is critical to the design process of rotorcraft. In hovering flight or axial flight, a first-order approximation of rotor performance can be computed through the use of momentum theory generalized by Glauert [16]. Momentum theory treats the rotor as an infinitely thin disk that can support a thrust force caused by rotation of the disk for which power is supplied. The change in fluid properties across the rotor disk is assumed to occur instantaneously in an inviscid, one-dimensional process. Assuming a given thrust and atmospheric parameters, the velocity field below the rotor induced by the rotor disk can be computed, which can then be used to compute the ideal power required for hover. These parameters can be calculated quickly and efficiently, allowing the comparison of several different rotor designs. However, simple momentum theory has several drawbacks. Given the one-dimensional, first-order nature of momentum theory, the rotor wake has no vortical content and is treated as a slipstream of fluid moving downward away from the rotor. Additionally, it is an ideal analysis that assumes away many non-ideal effects in the formulation for power required, such as tip losses, wake swirl, and a finite number of blades. These non-ideal effects can be accounted for in the formulation for a power correction called induced power [1],

$$C_{Pi} = \frac{\kappa C_T^{3/2}}{\sqrt{2}} \tag{2.1}$$

where C_T is the thrust coefficient and the induced-loss factor κ is often set to 1.15 based on empirical data. Another drawback of simple momentum theory is in its ignorance of blade geometry, which is essential for accurate power prediction. This can be overcome by a correction to compute the profile power, i.e. power increase caused by the aerodynamic profile of the rotor

blade. Assuming basic elements of the rotor design are known such as blade chord, radius, and zero-lift drag coefficient of the airfoil, the profile power can be computed. From this, an efficiency can be estimated for a hovering rotor, known as the figure of merit (FM) [17]. The FM is defined as the ratio of ideal power required to actual power required and is given as,

$$FM = \frac{P_{ideal}}{P_{induced} + P_{profile}} = \frac{\frac{C_T^{3/2}}{\sqrt{2}}}{\frac{\kappa C_T^{3/2}}{\sqrt{2}} + \frac{\sigma C_{d0}}{8}} = \frac{{C_T}^{3/2}}{\sqrt{2}\, C_Q} \tag{2.2}$$

where σ is the blade solidity and C_{d0} is the zero-lift drag coefficient. Thus, with a basic blade design and thrust desired, the hover efficiency can be estimated. The FM can also be used to compare different rotor designs, assuming the rotors have the same disk loading, i.e. the ratio of thrust to disk area. Similar momentum theory analyses can be extended to other flight conditions such as axial climb, axial descent, and forward flight.

While simple momentum theory can account for the change in area, velocity, and pressure across the rotor-disk plane, it cannot predict the thrust coefficient for more advanced blade designs. More simply, momentum theory gives no insight in how the rotor should be designed to produce a given thrust [18]. Momentum theory assumes the inflow velocity field below the rotor is uniform. From a design standpoint, this insinuates the blade has a constant spanwise pitch, a consequence of assuming an infinitely thin disk. However, a constant spanwise blade pitch is a poor rotor design as it heavily contributes to the asymmetry of lift in hover [1]. By twisting the blade from the root to the tip, such that the blade pitch at the tip is lower than that at the root (negative blade twist or washout), higher lift can be produced at more-inboard sections compared to an untwisted blade. This in turn provides a more-uniform spanwise blade loading, which can greatly affect rotor FM [19]. The effects of twist can be accounted for using blade element analysis, which is capable of more accurately computing the induced velocity field, from which rotor forces and moments may be computed [1]. For a blade with linear twist, by knowing the pitch angle θ at the 75% radius ($r/R = 0.75$), then thrust is computed as

$$C_T = \frac{1}{2}\sigma C_{l\alpha}\left[\frac{\theta_{75}}{3} - \frac{\lambda}{2}\right] \tag{2.3}$$

where C_{l_α} is the lift-curve slope of the given airfoil. Power can then be computed as a function of incremental spanwise changes of thrust dC_T and the inflow ratio λ,

$$\int_{r/R=0}^{r/R=1} \lambda dC_T \; d\Big(\frac{r}{R}\Big) + \int_{r/R=0}^{r/R=1} \frac{1}{2}\sigma C_d r^3 \; d\Big(\frac{r}{R}\Big) \tag{2.4}$$

This formulation assumes that the blade tip is capable of producing thrust, which is not physical. At the blade tips, a tip-vortex is released which increases the local inflow ratio and reduces local thrust, called tip-losses [1], summarized by Prandtl and Betz in 1927 [20]. To include these tip-losses in blade element analysis, the blade tip can be considered not to produce lift, as was done by Gessow [21] and Gessow and Myers [18]. These tip-losses add additional non-uniformity to the inflow field and can be accounted for by increasing the value of κ given in Eq. 2.2.

2.1.1 Blade Element Momentum Theory

Building further upon basic theory, Gessow [21] and Gustafson and Gessow [22] assimilated blade element analysis and momentum theory in a formulation known as blade element momentum theory (BEMT), another method to estimate spanwise inflow distribution. BEMT differs from previous models by discretizing the rotor disk in a series of annuli, over which the mass flux and differential thrust may be computed. A consequence of this is that BEMT takes into account the angular momentum imparted on the wake by the blades which more physically captures the wake [1]. However, in practicality, the effect of swirl on predicted performance is minimal and can be neglected [16] . For hover, this simplifies the computations of thrust and power, given by Glauert [16] as,

$$C_T = \int_{r/R=0}^{r/R=1} \lambda^2 \frac{r}{R} \; d\Big(\frac{r}{R}\Big) \tag{2.5}$$

$$C_{P_i} = \int_{r/R=0}^{r/R=1} \lambda^3 \frac{r}{R} \; d\Big(\frac{r}{R}\Big) \tag{2.6}$$

Now, the radial inflow λ is required to solve Eq. 2.5 and 2.6. In hover, the radial inflow is

$$\lambda(r) = \frac{\sigma C_{l_\alpha}}{16}\left(\sqrt{1 + \frac{32}{\sigma C_{l_\alpha}}\theta r} - 1\right) \tag{2.7}$$

By discretizing the blade into differential radial sections, the radial inflow distribution may be attained and integrated to compute thrust and power required. The value of BEMT lies in that performance can be estimated for arbitrary blade designs with respect to planform and twist. Conversely, momentum theory is ignorant of these parameters and blade element theory cannot account for radially-varying inflow. BEMT can be used to determine the required lift coefficient distribution across the span by using the radial inflow distribution, which can aid in the airfoil selection process. Additionally, the effective angle of attack can be determined as a function of radial inflow and the twist distribution, assuming the small angle approximation is valid. BEMT can be further improved with a blade tip loss correction factor suggested by Prandtl [20], improved by Goldstein [23], and also with a compressibility correction outlined by Leishman [1] based on the Prandtl-Glauert rule [24].

2.1.2 Blade Element Momentum Theory for Forward Flight

BEMT can also be used in forward flight, where the inflow field is more difficult to estimate. This inflow field becomes additionally a function of the azimuthal position ψ of the rotor blade and its flapping angle β (i.e. the angle between the blade tip and hinge) [1]. In forward flight, there is both a chordwise velocity component and a radial velocity component due to the rotor rotating in a freestream velocity field. This, however, adds complexity to the inflow field as it is now necessarily asymmetric. As a remedy, several models exist to predict inflow and close the system of equations, such as a suite of linear inflow models validated by the experimental results of Brotherhood and Stewart [25]. These models take the general form of

$$\lambda_i = \lambda_o \left(1 + k_x \frac{x}{R} + k_y \frac{y}{R} \right) \tag{2.8}$$

where k_x and k_y have various forms but generally are functions of the wake skew angle and advance ratio [26–30]. A more complex inflow model is offered by Mangler [31], Squire [32], and Mangler and Squire [33], which is formulated via the linearized, incompressible, Euler equations and uses the pressure difference across the disk to estimate inflow. Another method is the actuator disk model of Ormiston [34] which uses bound circulation to compute inflow. More recently, Peters et al. [35] and Peters and He [36] expressed inflow distribution in an infinite series which can then be

substituted into the Euler equations and solved as a first-order differential equation. Although these models can predict rotor wakes in forward flight, they require an *a priori* assumption or estimate of blade loading, a distinct disadvantage of these first-principles methods.

2.2 Early Rotorcraft CFD Techniques

From these first-order aerodynamic methods stems the desire to more accurately model rotor flowfields. Historically, these low-fidelity, inexpensive methods proved useful for the basics of rotor design. However, these methods cannot, or poorly, take into account the wake system of the rotor which continually influences rotor performance [37]. Early methods of wake capturing were built on an extended form of Prandtl's lifting line theory [38, 39]. One of these methods is the prescribed wake model, which uses the wake age (i.e. the flowfield history stored in the wake) to fix the positions of tip vortices [1]. Landgrebe formulated a prescribed wake model for hover as a function of blade geometric parameters such as twist and radius, along with performance parameters such as thrust [40]. From this, the positions of the tip vortex system and vortex sheets can be described via the aforementioned input parameters. Then, the inflow field can be computed and rotor performance can be estimated. Similarly, Kocurek and Tangler [41] formulated a prescribed wake model that ignores the more radially-inward regions of the vortex sheet, but attempts to include the number of blades and the twist distribution. For forward flight, there exist prescribed wake methods that can exactly solve the induced velocity field [28, 42], and generalized wake models that seek to compute vertical displacement of tip vortices with a modification to the modeling of rigid wakes [43, 44].

A distinct disadvantage of these prescribed wake models is the necessity of experimental data to formulate the required correlations. In an effort to circumvent this, there exist free-vortex wake models [45–50] that do not require experimental results on the basis of various critical assumptions. These methods model vortices as inviscid, line vortex filaments, which are convected and tracked throughout the flowfield using the substantial derivative of the motion of vortex filaments, given as

$$\frac{\partial r}{\partial t} + \frac{\partial r}{\partial x} = V(r) \tag{2.9}$$

By spatially discretizing the domain, the spatial derivative term drops out, and the position of the convected vortex filaments can be computed as a system of linear, time-dependent, ordinary differential equations. From this reduced system of equations, the full velocity field can be computed by integrating the Biot-Savart law. A distinct advantage of free-vortex wake methods is the ability to account for vortex-vortex interactions in the wake. However, integrating the Biot-Savart law over each vortex filament demands a much higher computational cost in comparison to prescribed wake methods. Free-vortex methods, however, can be accelerated in terms of computational time, as shown by Sarpkaya [51] and Brooks et al. [52]. Nevertheless, the free-vortex wake method is an improvement over prescribed wake methods, particularly in its ability to predict the wake structure without experimental correlations.

In order to validate these wake models, experimental data is required. However, to match experimental aeroelastic conditions, the simulated rotor must be trimmed. In rotorcraft control, the collective and cyclic control inputs can trim the rotor to a quasi-steady state, such as constant thrust in hover or forward flight. To trim the rotor, a vector of control inputs $\vec{X}$ must be coupled to a vector of rotor responses $\vec{Y}$ [1].

$$\vec{X} = \begin{bmatrix} \theta_0 \\ \theta_{1c} \\ \theta_{1s} \end{bmatrix} \quad \vec{Y} = \begin{bmatrix} C_T \\ \beta_{1c} \\ \beta_{1s} \end{bmatrix} \tag{2.10}$$

An initial guess for control input allows for an initial rotor response. By perturbing each value of the control vector and iterating, the desired rotor response can be achieved, such as a given thrust level or a given flapping response. Coupling a rotor trim model with an aerodynamic model is known as comprehensive rotor analysis [53, 54] and can estimate trim variables in order to validate wake models for various flight regimes.

2.2.1 More Complex CFD Methods

With the availability of more powerful computational resources came the tractability of using more sophisticated, complex CFD methods. One of the earliest of these methods is the full-potential method. The potential flow equations come from the assumption that the flow is irrotational so that the velocity field can be expressed via some potential function,

$$\vec{V} = \nabla\phi \tag{2.11}$$

This formulation is agnostic to compressibility effects, though the full-potential equations outlined by Strawn and Caradonna [55] can account for compressibility effects and transonic effects. By coupling a near-blade, finite-difference grid with the full-potential equations to a prescribed wake or free-vortex make model, illustrated in Fig. 2.1, more robust solvers could be developed that could more accurately capture transonic effects and shocks [55–59].

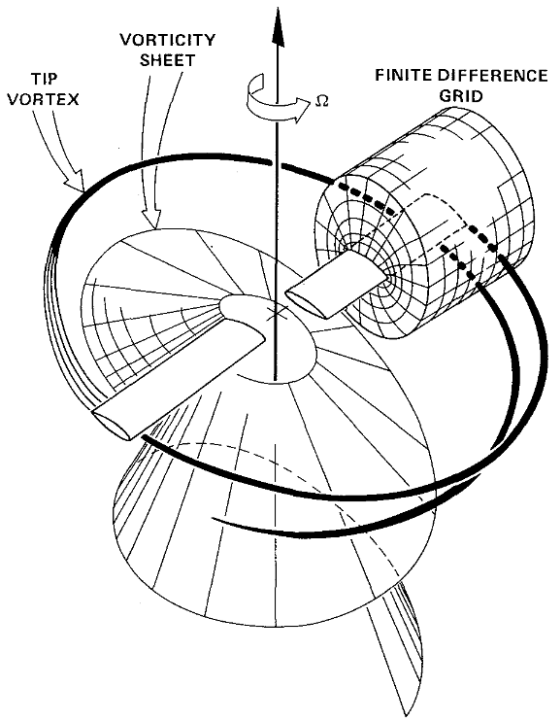


Fig. 2.1 Rotor wake with a near-body finite difference grid [55]

Caradonna and Isom [60] modified these equations and assumed these transonic effects are small, spawning the transonic small disturbance equations, a particular sub-family of the full-potential equations. This method allows for the study of tip speed effects in the transonic regimes, particularly useful when analyzing forward flight, but is limited to low lift and lower transonic Mach numbers [55].

Around the same time, Euler methods gained traction due to their ability to capture shocks in an inviscid, non-isentropic manner. The Euler equations are a particular subset of Navier-Stokes and are written in conservative form as,

$$\frac{\partial}{\partial t}\begin{bmatrix}\rho\\ \rho u\\ \rho e_0\end{bmatrix} + \frac{\partial}{\partial x}\begin{bmatrix}\rho u\\ \rho u^2 + P\\ \rho u h_0\end{bmatrix} = 0 \tag{2.12}$$

Such an assumption is valid for high Reynolds number flows around rotors, as the viscous term of the Navier-Stokes equation scales with the inverse of the Reynolds number. However, by neglecting the viscous effects, vorticity in the flowfield is conserved without diffusion nor dissipation, which is non-physical, particularly with respect to rotor wakes. But, when discretizing the equations, an artificial dissipation term is added which aims to prevent spurious oscillations in regions of strong pressure gradients [61]. This artificial dissipation acts as an artificial viscosity, which allows circulation to be generated about some aerodynamic body, enabling prediction of lift. Such implicit, upwind schemes lend themselves to lower dissipation, which is more numerically robust [62]. Kroll [63] used an explicit method to solve the Euler equations, simulating a rotor and wake in hover conditions. The blade was discretized into a grid that encompassed the blade itself and a large portion of the wake. However, the coarseness of this grid underpredicted the inflow to the rotor and was exacerbated by significant dissipation of the rotor wake. Studies by Kramer et al. [64] used an upwinded scheme on the same data used by Kroll, finding similar predicted performance. Chen and McCroskey [65] showed similarly poor predictions compared to experiments, citing a highly dissipative flowfield with the coarse grids due to computational resource restrictions. In general, early Euler methods had difficulties in preserving vorticity, which is especially important in the wake, due to the numerics of artificial dissipation and diffusion.

2.2.2 Navier-Stokes CFD Methods

For rotor flowfields, capturing the wake is essential to enabling the best possible predicted performance when using computational methods [1]. Early methods largely ignored viscosity, or treated it by proxy of artifical dissipation, as in Euler methods. However, the Navier-Stokes equations can explicitly treat the viscosity present in the flowfield. The Navier-Stokes equations

are a highly non-linear set of coupled partial differential equations, which can be costly to compute, especially if an unsteady solution is desired. One difficulty in solving the Navier-Stokes equations for rotorcraft applications is the requirement for sufficiently fine grids. A rotor in hover experiences various physical scales of turbulence and vortices which must be captured in order to provide valuable computational results. A sufficiently fine grid must then be capable of capturing these scales; however, this increases the required computational time. The Reynolds-averaged Navier-Stokes (RANS) equations [66] can be used to ease computational cost by effectively smoothing out turbulent length scales. This allows for computational solutions for steady problems, as the unsteady quantities are eliminated by the averaging. But, smoothing out these terms removes an equation from the system, leaving one additional unknown. This unknown can be accounted for by assuming fully-laminar flow or by applying a turbulence model to close the system. However, one of the biggest advantages of Navier-Stokes based methods is the ability to model vortex roll-up, essential for capturing rotor-tip vortices.

One of the first application of the RANS equations to rotor flows was done by Sankar and Tang [67]. They used the second-order, implicit Beam-Warming scheme [68] to discretize the unsteady RANS equations. This method uses a constant time step at each point in the flowfield, allowing the capturing of fluctuations in the mean flow. A NACA 0012 airfoil was simulated in various flight conditions, including pitching, low-subsonic, viscous conditions. The pitching airfoil showed good agreement with experiments and was able to capture the hysteresis in force and moment coefficients shown in the test data. Additionally, a simulated interaction between a passing vortex and the airfoil at transonic conditions was performed, based on an assumed vortex position, motion, strength, and structure. The results showed that airfoil lift was affected by the vortex impinging on the airfoil surface. This study exhibited that these blade-vortex interaction (BVI) events can be captured in CFD solutions. This phenomenon is common in rotorcraft flows, as the tip-vortex released by a blade often collides with the surface of the advancing blade, a diagram of which is shown in Fig. 2.2. Rai expanded upon the numerical study of BVI by increasing the order of accuracy of the employed discretization scheme and modifying the scheme to eliminate *a priori* knowledge of the vortex size, structure, or trajectory [69]. By increasing the order of the method, a vortex traveling through space can be conserved for longer, as there is less dissipation required for the scheme. This

method showed good agreement with experimental data and demonstrated the motivation in using higher-order methods for improved solution accuracy.

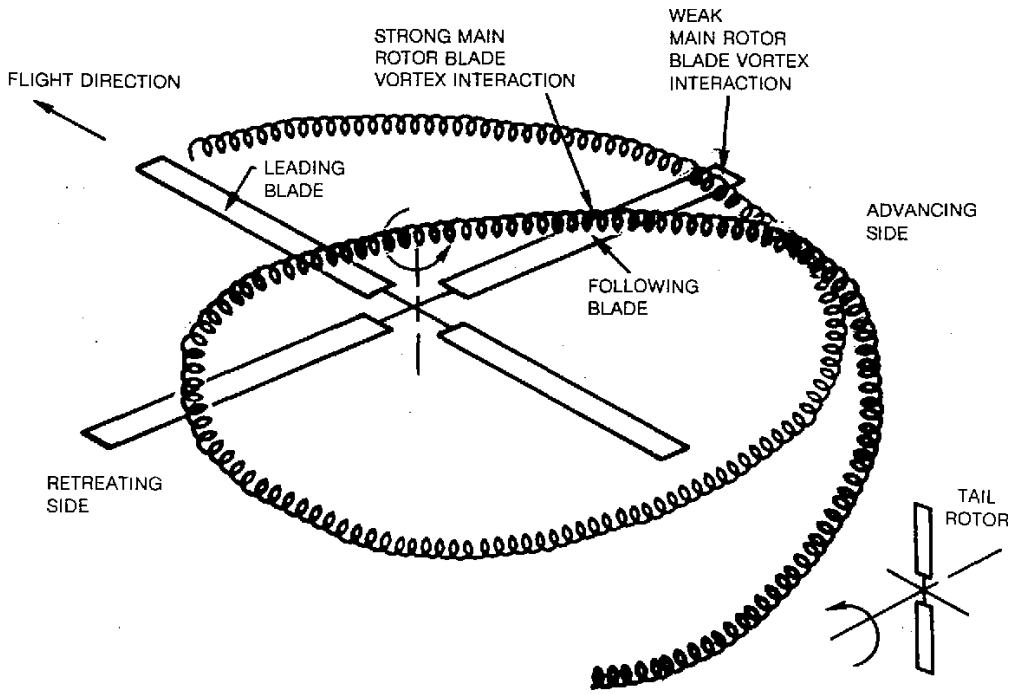


Fig. 2.2 Rotor blade-vortex interaction in forward flight [70]

With the limited computational resources at the time, early RANS-based rotorcraft simulations sought to minimize computational time by coupling near-body Navier-Stokes solutions to pre-existing, validated, lower-fidelity methods. One technique is to solve the RANS equations for a hovering rotor, but computes the wake using a free-vortex wake method [71–73], such as that built into CAMRAD. But, this weak coupling introduces errors into the predicted flowfield, especially with respect to rotor inflow at high thrust levels. Removing the need for a wake model, Srinivasan et al. simulated rotors in hover using a Navier-Stokes method for the full flowfield (i.e. no external wake models) [74], building upon that of Srinivasan and McCroskey [73]. The developed code, TURNS (Transonic Unsteady Rotor Navier-Stokes), captures the entirety of the rotor wake and uses a periodic boundary condition, modeling only one blade of the rotor, saving significant computational time. The third-order upwind Roe scheme was used, which allows for higher-order accuracy determinations of the fluxes [75]. Predicted spanwise slices of pressure distribution

showed improved agreement with experiments over a code that used an external wake model and an Euler code. The wake was captured well, accurately predicting the wake position and wake contraction as a function of wake age, as shown in Fig. 2.3. Further studies with TURNS showed good prediction of sectional loading characteristics and the ability to capture separated flow [76] as well as the ability to predict rotor noise in hover and forward flight [77]. Similarly, Duque performed a 3-D RANS simulation using the LANS3D code of JAXA in order to study planform effects of a stationary BERP rotor in transonic conditions [78].

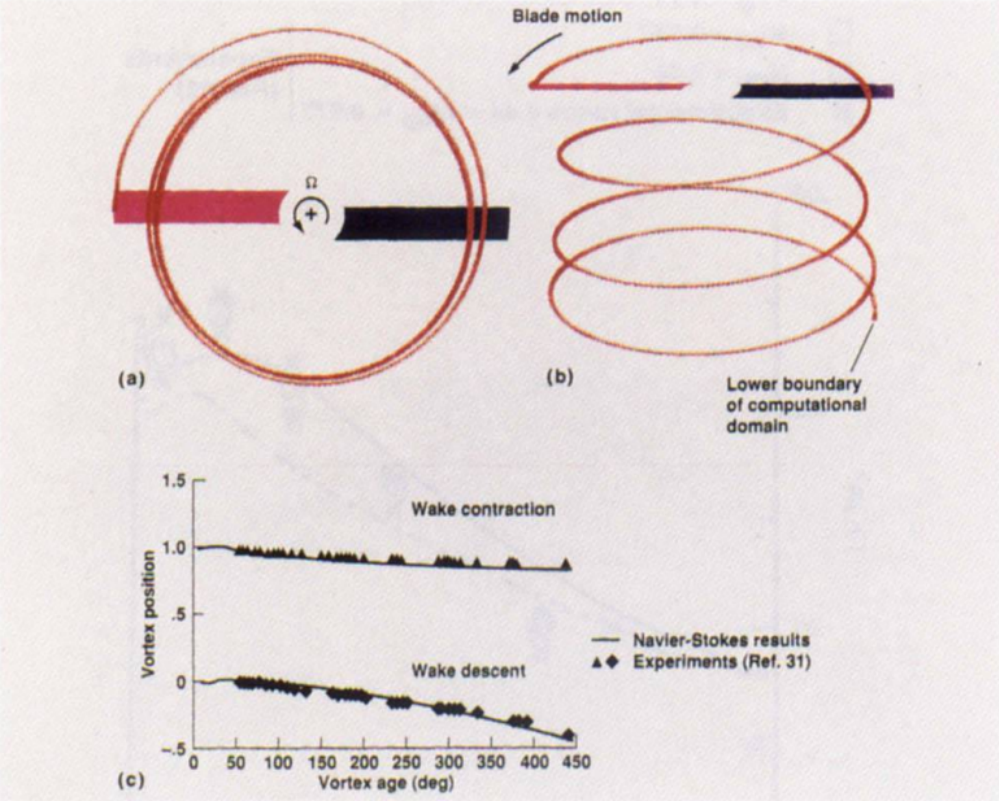


Fig. 2.3 Predicted wake structure of a rotor in hover using TURNS [74]

A further advancement in rotorcraft CFD came in the creation of overset grid methods. The overset, or Chimera, grid technique uses sets of grids embedded within each other [79]. A major grid encompasses the full domain, from the object of interest to the farfield. Then, minor, sub-grids are overset into the major grid without additional mesh boundary requirements. This allows the resolving of flow features on scales smaller than that of the scale of the major grid. Such a method

allows for quick grid generation of complex configurations, such as a wing-body junction, and can minimize mesh distortion [80]. Unfortunately, overset methods also increase the complexity of the code. If two points near each other in space belong to different grids, then the solver must enforce the communication between these points in order to splice together the flow solution between each grid, called "overset boundary interpolation". An example overset grid [81] is shown in Fig. 2.4. The MD 30P/30N airfoil features a slat, main element, and a flap. Using the overset method allows each element to move independently relative to other grids. Changing the slat position and angle, or the flap position and angle, is as simple as specifying coordinates in the input deck and does not require the user to remake any grids. However, in such a configuration, additional difficulties arise when solving the system, specifically with communication between grids. For example, if the flap position is moved more forward relative to the main element, a portion of the flap grid may lie on top of the impermeable surface of the main element. In this region, the points in the flap grid that overlap the surface must be "blanked out", and the solver ignores those points in its calculations. This technique is called "overset hole-cutting" [80].

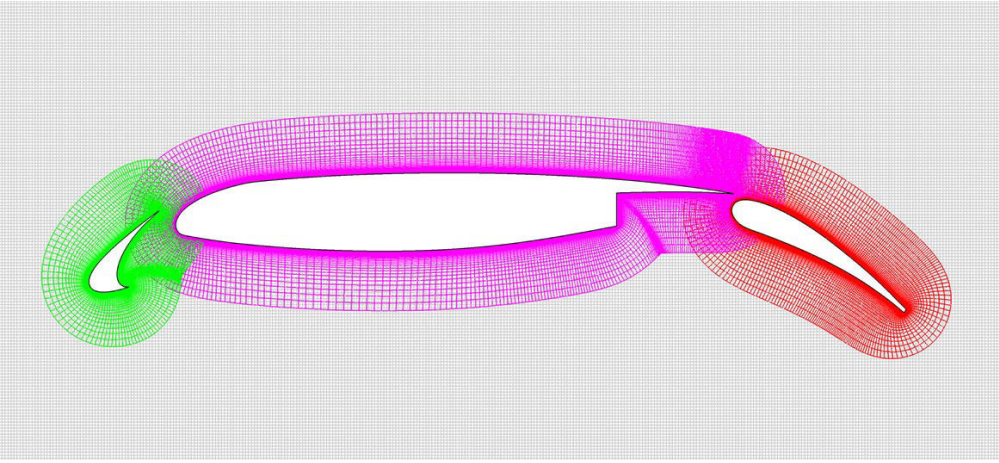


Fig. 2.4 Overset grid system for the MD 30P/30N airfoil [81]

McCroskey first identified the utility in overset methods for rotorcraft systems, specifically due to overset methods' flexibility in gridding and ability to better capture tip-vortices [82]. Using overset methods could allow for separate rotor grids and airframe grids, allowing for prediction of

rotor/airframe interactions. Meakin applied novel hole-cutting techniques to the overset method and simulate a V-22 tiltrotor in forward flight [83]. This grid system properly captured the wake structure and pressure distributions, proving that overset methods can be used for complex, rotorcraft systems.

2.3 RANS-based Turbulence Closure

When applying Reynolds-averaging to the Navier-Stokes equations, a method for turbulence closure is required in order to account for the Reynolds stresses. The incompressible RANS equations are given as,

$$\frac{\partial \overline{u_i}}{\partial t} + \overline{u_j}\frac{\partial \overline{u_i}}{\partial x_j} = \frac{-1}{\rho}\frac{\partial \overline{P}}{\partial x_i} + \frac{\partial}{\partial x_j}\left[\nu\frac{\partial \overline{u_i}}{\partial x_j} - \overline{u_i' u_j'}\right] \tag{2.13}$$

where the final term, the mean of the product of velocity perturbations, accounts for the Reynolds stresses and serves as a source of turbulence. This term is difficult to compute and introduces the turbulence closure problem. This problem is typically solved via a turbulence model, which seeks to model the production and destruction of turbulence as a surrogate to the Reynolds stress terms. The Reynolds stresses are often modeled using the Boussinesq approximation, where the momentum transfer due to turbulence can be modeled using a turbulent eddy viscosity, ν_t, given in Eq. 2.14. This relies on the assumption that the deviatoric portion of the Reynolds stress is proportional to the mean strain rate [84]. The difficulty in this approximation is the determination of the turbulent eddy viscosity.

$$-\overline{u_i' u_j'} = \nu_t\left(\frac{\partial u_i}{\partial x_j} + \frac{\partial u_j}{\partial x_i} - \frac{2}{3}\frac{\partial u_k}{\partial x_k}\delta_{ij}\right) \tag{2.14}$$

2.3.1 Zero-equation Turbulence Closure Models

One of the first turbulence models is Prandtl's mixing-length model [84]. For quasi-parallel viscous flows, the eddy viscosity is given as,

$$\nu_t = \ell_m^2\left|\frac{\partial u}{\partial y}\right| \tag{2.15}$$

where ℓ_m is the mixing length and is the distance in which a turbulent eddy travels before it is destroyed by mixing. For turbulent boundary layers, this mixing length is often assumed to be a function of normal distance from the wall.

Smith and Cebeci developed a turbulence model based on the profile of a turbulent boundary layer [85]. By splitting the boundary layer profile into an inner and an outer region, the eddy viscosity can be computed in each region. The regions are then stitched together by performing a search to determine where the inner eddy viscosity is equal to the outer eddy viscosity. This model functions well for high-speed flows, but requires an *a priori* specification of the boundary layer edge.

Baldwin and Lomax formulated a turbulence model [86] based on the Cebeci-Smith model by generalizing the mixing length hypothesis and restricting it to the "inner" region of a turbulent boundary layer. This model performs well for attached boundary layers, but requires a specification of the mixing length function, which is difficult to determine for flows with large separated regions and high curvature or rotation. One distinct disadvantage of these algebraic (zero-equation) turbulence models is that they assume the production of turbulent kinetic energy is equivalent to the dissipation rate, meaning that eddy viscosity is purely a function of the mean flowfield [87].

2.3.2 One-equation Turbulence Closure Models

A class of one-equation, partial differential equation (PDE) based turbulence models arose in a desire to directly compute the eddy viscosity by means of a single transport equation, which can properly account for upstream flow history. Building upon his mixing length model, Prandtl postulated that the eddy viscosity could be computed as a function of the turbulent kinetic energy k and turbulent length scale ℓ [88]. The turbulent dissipation ϵ is assumed to be a function of some closure coefficient, turbulent kinetic energy, and length scale.

$$\epsilon = C_D \, k^{3/2} \, / \ell \tag{2.16}$$

With an assumption of the closure coefficient and an estimate of the length scale, the turbulent kinetic energy must be computed by means of a transport equation, which takes the form of the substantial derivative of diffusion. This model performs reasonably well when the flow is in

equilibrium, where k and ϵ are balanced [89]. Another one-equation model based on turbulent kinetic energy is that of Bradshaw et al. [90]. They argued that the Reynolds shear stress varies linearly with turbulent kinetic energy, where k is solved via a transport equation. Townsend confirmed this hypothesis experimentally, noting that the ratio of Reynolds shear stress to turbulent kinetic energy is nearly the same for a wide range of flows [91]. This model showed significant improvement over the contemporary algebraic models, but was not applicable to a wide range of flows. Nee and Kovasznay were the first to formulate a one-equation model to directly compute the eddy viscosity, rather than computing eddy viscosity based on k and ϵ [92]. This model has seen little use, but each term in its formulation is based on the underlying physics, where each term has a physical meaning. Similarly, Baldwin and Barth developed a more elaborate one-equation eddy viscosity model [93]. The transported quantity in this case is a characteristic turbulence Reynolds number, from which the eddy viscosity is computed with an algebraic equation.

$$\frac{\partial}{\partial t}(\nu\tilde{R_T}) + u_j \frac{\partial}{\partial x_j}(\nu\tilde{R_T}) = \left(C_{\epsilon 2} f_2 - C_{\epsilon 1}\right)\sqrt{\nu\tilde{R_T} P} + \left(\nu + \frac{\nu_t}{\sigma_\epsilon}\right)\frac{\partial^2(\nu\tilde{R_T})}{\partial x_k \partial x_k} - \frac{1}{\sigma_\epsilon}\frac{\partial \nu_t}{\partial x_k}\frac{\partial(\nu_t\tilde{R_T})}{\partial x_k} \tag{2.17}$$

where the eddy viscosity is,

$$\nu_t = C_\mu \nu \tilde{R_T} D_1 D_2 \tag{2.18}$$

This model is dubbed a "complete" model in that it requires no tweaking of coefficients or functions to provide a physically-valid closure model. The final term in Eq. 2.17 is a dissipation term for the eddy viscosity which explicitly bypasses the need to estimate mixing length. Consequently, for cases with a uniform stream, such as a flat plate, the eddy viscosity will remain constant rather than decay, as the gradient terms go to zero. Additionally, the Baldwin-Barth model tends to be highly sensitive to freestream conditions. Spalart and Allmaras developed a one-equation eddy viscosity model that uses wall distance as its length scale [94]. The model was designed for wall-bounded flows for aerospace applications. The Spalart-Allmaras (SA) model treats the turbulent boundary layer by blending a formulation for the viscous sublayer to a formulation for the logarithmic layer. This blending necessitates that the grids be able to resolve the viscous sublayer, utilizing $y^+ \leq 1$.

The transported, modified eddy viscosity is easily converted to the actual eddy viscosity via a damping function based on the kinematic viscosity.

$$\nu_t = \tilde{\nu} f_{v1} \tag{2.19}$$

An additional function of the SA model is the inclusion of a trip term, which allows for specification of laminar-turbulent transition locations. Numerous variants exist which add additional functionality to the model, such as negative values of the modified eddy viscosity (SA-neg) [95], rotation/curvature corrections [96], and formulations that do not use the Bousinessq approximation to model the Reynolds stresses [97, 98]. An in-depth discussion of the full formulation of the Spalart-Allmaras model will be discussed in the following chapter.

2.3.3 Two-equation Turbulence Closure Models

In a departure from the methods to compute eddy viscosity of the zero-equation and one-equation models, the class of two-equation PDE-based turbulence models seek to construct eddy viscosity based on two distinct scales of the turbulent flowfield. These models typically solve a transport equation for the turbulent kinetic energy k and another equation for either the dissipation rate ϵ or the specific dissipation rate ω. The formulation for the eddy viscosity generally takes the form [99]

$$\nu_t = C_\mu f_\mu \frac{k^2}{\epsilon} \tag{2.20}$$

where C_μ is a structural constant and f_μ is a near-wall damping function. The most widely-used formulation of a $k-\epsilon$ model is that of Launder and Sharma [100]. The transported turbulent kinetic energy and dissipation rate are then used to compute the eddy viscosity using Eqn. 2.20 without the damping function. Generally, the $k-\epsilon$ model behaves well for turbulent shear flows, but does not behave as well in highly adverse pressure gradients and separated flows [89]. One facet of the model is that ϵ exhibits local extrema near the wall as it does not properly treat boundary conditions at the wall [99]. Some of these issues are alleviated in the Realizable $k-\epsilon$ [101] and the Renormalization Group (RNG) $k-\epsilon$ models [102]. The Realizable model treats C_μ as a variable rather than a constant and uses a different formulation for the transport of ϵ, which has shown improved predictions for

turbulent jets, mixing layers, and separated flows [101]. The RNG model renormalizes the Navier-Stokes equations to account for smaller turbulence scales [102]. The formulation modifies some constants and coefficients in the production term of the ϵ equation in order to improve the prediction of scales in recirculating, separated flows [99]. However, it remains that the $k-\epsilon$ class of turbulence models is still difficult to integrate at the wall [103].

Another popular two-equation model is the class of $k-\omega$ models, where ω is the specific turbulence dissipation rate and is given as the ratio of dissipation ϵ to turbulent kinetic energy k. In order to maintain proper dimensionality, the eddy viscosity is computed as

$$\nu_t = \alpha \frac{k}{\omega} \tag{2.21}$$

where α is some constant. This formulation was first suggested by Kolmogorov [104]. A suite of changes and improvements to Kolmogorov's model have been proposed by Launder and Spalding [105] and Wilcox [106, 107]. These models keep Kolmogorov's transport equation for k largely unchanged, but greatly modify the equation for ω. In the transport of ω, there is an additional destruction term to account for vortex stretching. These models tend to perform better in highly adverse pressure gradients and can be more-easily applied to the viscous sublayer [89]. Nevertheless, they are very sensitive to specified freestream values of ω which greatly affected the models' ability to predict inlet-type flows [103]. A remedy exists for these behaviors by accounting for the transport of shear stress, which is accomplished by blending the best parts of algebraic, $k-\epsilon$, and $k-\omega$ models, as proposed by Menter [108]. This model, known as $k-\omega$ Shear Stress Transport (SST) uses a blending function to maintain $k-\omega$ type behavior near the wall, and switches to $k-\epsilon$ type behavior far from the wall. Thus, the model can be fully integrated into the viscous sublayer near the wall, while properly capturing circulating, shear flows. The $k-\omega$ SST model is one of the most widely used two-equation turbulence models and has been the subject of several improvements since its inception [103, 109].

2.3.4 Other Turbulence Closure Models

There exist turbulence closure models that employ more than two equations, but it should be noted they become increasingly complex and expensive to implement in CFD methods. Durbin's $\overline{v^2}-f$

model adds two equations to the $k-\epsilon$ model, one for a turbulent velocity scale and one for an elliptic relaxation function, respectively [110]. The formulation does not require wall functions as it is valid all the way down to solid surfaces and can be classified as a "low Re model". By changing the velocity scale variable to $\zeta = \overline{v^2}/k$, the $\zeta - f$ model is attained, which has shown improved computational performance [111]. More complicated models exist that seek to directly compute the Reynolds stress tensor rather than use the Boussinesq approximation, called Reynolds Stress Transport Models (RSM) [112, 113]. The class of two-or-fewer equation turbulence modes fail to naturally capture the physics for anisotropic flows or flows with streamline curvature [114]. The RSM models can capture these physics as they are second-order equations and can capture second-moment terms relevant to turbulence [99]. Generally, these models feature seven equations: six for the unique Reynolds stresses and one for a relevant turbulence scale, such as ϵ [115] or ω [116]. These additional equations lend to their unpopularity for CFD-applications due to the increased computational cost an complexity to implement. However, the class of Explicit Algebraic Reynolds Stress Models (EARSM) reduces the size of the system by computing the Reynolds stresses algebraically as a function of relevant turbulence scales. Pope developed the first EARSM limited to two-dimensional flows [117], which was later extended to three-dimensions [118, 119] and has seen some use in aerodynamic analyses. The EARSMs bridge the gap between eddy viscosity models and RSM, allowing a more computationally efficient method for determination of the Reynolds stresses.

2.4 Developments in CFD-Compatible Transition Modeling

Transition is the phenomenon in which a fluid flow changes from laminar to turbulent. Nearly every external, solid surface is affected by transition and this phenomenon must be accounted for in order to properly capture the flow physics [5]. The inability to capture transition may improperly predict skin friction and heating caused by energy transfer. Traditionally in CFD, turbulence closure is achieved using a fully-turbulent model, which neglects laminar flow. One method to enforce laminar flow in the RANS equations is by omitting the use of a turbulence model. However, then the flowfield becomes fully-laminar and transition cannot be predicted. Thus, there exists a need for transition modeling that is compatible with turbulence models for CFD application.

Prandtl postulated that in fluid flows there is a thin region near a solid surface where all the viscous effects are contained [120]. By performing a scaling argument, he proved that many of the terms in the Navier-Stokes equations can be neglected inside this thin region, called the boundary layer. These equations are known as Prandtl's boundary layer equations and are given as, for two-dimensional flow,

$$\frac{\partial u}{\partial x} + \frac{\partial v}{\partial y} = 0 \tag{2.22}$$

$$u\frac{\partial u}{\partial x} + v\frac{\partial u}{\partial y} = -\frac{1}{\rho}\frac{\partial P}{\partial x} + \nu\frac{\partial^2 u}{\partial y^2} \tag{2.23}$$

$$\frac{\partial P}{\partial y} = 0 \tag{2.24}$$

For high Reynolds numbers, the flowfield can be split into a viscous, inner region governed by the boundary layer equations, and an inviscid, outer region governed by the Euler equations. A diagram of this "decoupling" of the flowfield, along with laminar and turbulent velocity profiles, is given in Fig. 2.5.

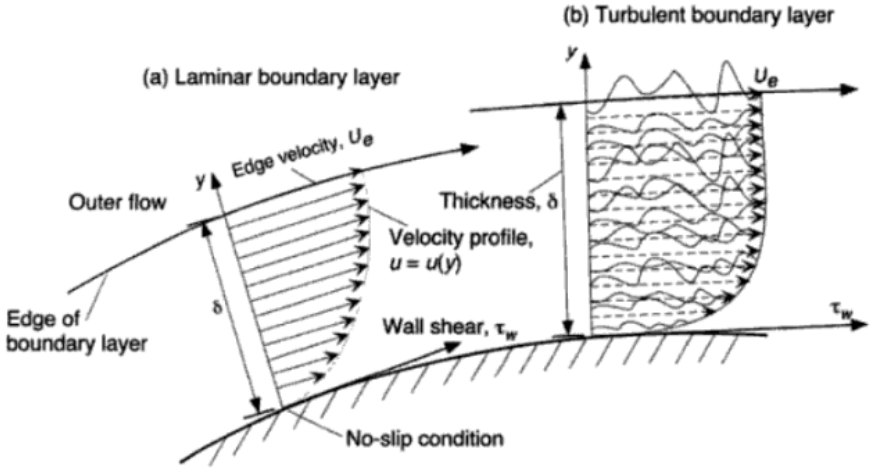


Fig. 2.5 Boundary layer profiles on a solid wall [1]

Transition itself is a complex process that can occur via different modes, such as natural transition, bypass transition, and separation-induced transition [121]. Natural transition can occur in flows with low freestream turbulence intensity and is caused by the amplification of velocity perturbations in a linear manner [9]. In two-dimensions, natural transition occurs via the growth of Tollmien-Schlichting (T-S) instabilities [122, 123], described by the Orr-Sommerfeld equations, which describes the stability characteristics of the Navier-Stokes equations [124–126]. Additional prominent modes of natural transition are those induced by Görtler instabilities [127] and cross-flow instabilities [128].

One of the chief difficulties in predicting transition using RANS-based CFD methods is that Reynolds-averaging ignores the effects of linear instability growth, which necessitates additional methods in order to capture transition [121]. The e^N method of Smith and Gamberoni [8] and van Ingen [129] side-steps these RANS limitations by assuming transition occurs when the most unstable wave reaches an amplification ratio equal to e^N, where N is some critical value based on freestream conditions. Although this method is accurate in determining transition, it is difficult to integrate with CFD methods due to the evaluation of non-local quantities and strong grid dependency [121]. Aside from the stability methods, local correlation methods employ characteristic boundary layer parameters to determine transition, based on experimental correlations. These methods often use pressure gradient parameters or characteristic Reynolds number to determine transition [130–133]. It is of note that since these methods are local and correlation-based, they cannot account for upstream flow history.

2.4.1 CFD-Compatible Transition Modeling

PDE-based methods are another class of transition prediction methods which may be more easily integrated with CFD as the framework for solving PDEs numerically is already built into the given CFD solver. Steelant and Dick designed a transport equation to compute turbulent intermittency in order to predict bypass transition [134, 135]. In CFD application, turbulent intermittency serves as a logical operator, where a value of zero is laminar and a value of one is turbulent, where values between zero and one can be used in terms for turbulence production. Although this model is relatively accurate at predicting bypass transition, it uses a non-local criterion to determine transition onset and requires the determination of the boundary layer edge [136]. Walters and

Leylek developed a CFD-compatible, one-equation transition model coupled to a $k-\epsilon$-type model [137]. By splitting the transport equation for k, there becomes one equation for the turbulent kinetic energy and one equation for the so-called laminar kinetic energy. This laminar kinetic energy can account for "splatting", where solid surfaces direct wall-normal fluctuations in the boundary layer into the streamwise direction, amplifying the growth of streamwise instabilities and triggering transition.

The Langtry-Menter model is a two-equation PDE-based transition model capable of accounting for a wide range of transition mechanisms [10, 103]. This model is most often coupled with the $k-\omega$ SST model and produces turbulence via an intermittency equation and a momentum thickness Reynolds number equation, given as,

$$\frac{\partial(\rho\gamma)}{\partial t}+\frac{\partial(\rho u_j\gamma)}{\partial x_j}=P_\gamma-E_\gamma+\frac{\partial}{\partial x_j}\left[\left(\mu+\frac{\mu_t}{\sigma_f}\right)\frac{\partial\gamma}{\partial x_j}\right] \tag{2.25}$$

$$\frac{\partial(\rho\tilde{Re}_{\theta t})}{\partial t}+\frac{\partial(\rho u_j\tilde{Re}_{\theta t})}{\partial x_j}=P_{\theta t}+\frac{\partial}{\partial x_j}\left[\sigma_{\theta t}(\mu+\mu_t)\frac{\partial\tilde{Re}_{\theta t}}{\partial x_j}\right] \tag{2.26}$$

The equation for momentum thickness Reynolds number determines the transition criterion and is used in the production term for the intermittency equation in order to grow and track turbulence. One distinct advantage over previous models is that it can properly account for different transition mechanisms and can be easily implemented due to its largely algebraic, correlation-based framework. However, this model is not formulated fully independent of the coordinate system [103]; that is, the model is not Galilean-invariant. This lack of Galilean-invariance can introduce uncertainties in flows with moving reference frames, such as rotorcraft flows, turbomachinery flows, and flows with high streamline curvature.

A more recent transition model is the Amplification Factor Transport (AFT) model developed by Coder [138] and Coder and Maughmer [139]. The AFT model is a PDE-based, two-equation transition model derived from the approximate envelope simplification of e^N theory. This allows the use of a single variable, the amplification factor $\tilde{n}$, to track the envelope of the instabilities in order to determine transition onset. By using a transport equation to compute the growth of the amplification factor, the upstream flow history is automatically tracked and accounted for. One drawback of this method is that in order to compute the amplification factor, certain integral

boundary layer quantities must be estimated, namely the momentum thickness and the shape factor. However, this is overcome by some clever correlations that estimate these quantities in an entirely local, Galilean-invariant formulation. This model has been implemented in several CFD solvers and is compatible with both the Spalart-Allmaras model and Menter's $k-\omega$ SST model [140]. A more in-depth discussion of the AFT model will appear in the following chapter.

2.4.2 Crossflow Transition Modeling

All of the aforementioned models are capable of determining transition for two-dimensional boundary layers. But, there exists another set of transition mechanisms for three-dimensional boundary layers for which these models do not account. For swept wings and rotating disks, a surface streamline has both a chordwise and a spanwise component, meaning that for viscous, shear flows, the boundary layer profile is three-dimensional [141]. A basic schematic of a three-dimensional boundary layer on a swept wing is given in Fig. 2.6. Modeling such flows using a transition model that does not account for crossflow can result in erroneous predictions of transition, force, and moment coefficients.

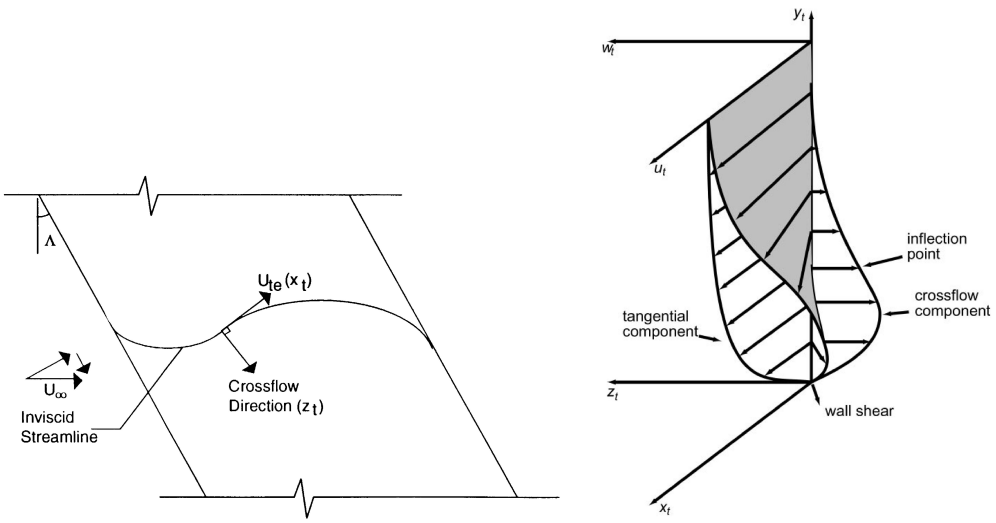


Fig. 2.6 3-D boundary layer on a swept wing [142]

Transition for three-dimensional boundary layers is not only caused by bypass, separation induced, and Tollmien-Schlichting (natural) transition, but can also be caused by crossflow instabilities.

One of the most prevalent and most dominating crossflow instabilities is the stationary crossflow instability [143], in which streamwise vortices form at the leading edge of a wing, sweep breaks, or other swept regions, and dominate transition onset. Additionally, this stationary crossflow instability can interact with Tollmien-Schlichting waves on the surface of a wing or solid body, which compounds the difficulties in predicting transition. For most CFD methods, this interaction is not modeled, and the crossflow instability is treated separately from Tollmien-Schlichting transition, often via an additional transport equation or by modifying existing transport equations to account for crossflow. Linear stability theory can account for crossflow instabilities but is still difficult to couple with CFD methods. Grabe et al. [7] have implemented the empirical C1 crossflow criterion and a helicity-based crossflow criterion in the DLR TAU solver. The C1 criterion is restricted to wing-like flows, but the helicity criterion can be applied more generally. An additional advantage of using helicity as a crossflow transition criterion is that helicity tracks streamwise vortices well, the primary mode of stationary crossflow transition. Helicity is defined as,

$$H = u_j \cdot \Omega_{ij} \tag{2.27}$$

and is inherently not Galilean-invariant due to its use of the velocity vector. A helicity Reynolds number can be correlated empirically to the integral boundary layer shape factor, which can then be used as a transition criterion. The implementation of Grabe et al. is restricted to subsonic flows, as the determination of the boundary layer edge is necessary and is computed using isentropic relations. Langtry et al. derived a helicity-based crossflow model and coupled it algebraically with the Langtry-Menter transition model [12], showing promise for a suite of test cases. The helicity approach is presently the most common method of accounting for crossflow instabilities and has seen widespread implementation with favorable results [13, 14]. Xu et al. [15] have developed a transport equation for the crossflow amplification factor, based on linear stability theory, and have successfully coupled it with the AFT model. This crossflow model shows excellent agreement with experiments and traditional linear stability theory, but is based on the 2014 version of the AFT model, which is not Galilean-invariant and is applicable primarily for low-speed flows.

2.5 Contemporary Fully Turbulent and Transitional Rotorcraft Simulations

Full Navier-Stokes solutions of rotorcraft problems are the decades-long culmination of efforts in improving turbulence and transition modeling, CFD codes, and CFD methods. Paired with modern computing power, high-fidelity rotorcraft solutions are more tractable for industry, academia, and others. Contemporary rotorcraft simulations focus on a variety of flight regimes such as hover and forward flight, and phenomena such as wake fidelity, vortex travel, turbulence and transition modeling, and geometry effects.

2.5.1 S-76 Rotor in Hover

Before the advent of CFD-compatible transition modeling, and due to computational restrictions, rotorcraft simulations were generally performed using a fully turbulent approach. One common rotor for CFD validation is the S-76 rotor in hover, a rotor with extensive wind tunnel testing [144]. Jain and Potsdam [145] simulated a rigid (no deformation) S-76 rotor in hover over a range of tip Mach numbers and collective pitches using the HPCMP CREATE^{TM}-AV component Helios [146]. In these predictions, only the fully turbulent Spalart-Allmaras model was used for turbulence closure. In order to maintain physical time accuracy, the solution was marched with a time step corresponding to 0.25° of rotor rotation with 40 Newton subiterations to improve temporal convergence. These simulations showed an underprediction of figure of merit (FM) as a function of thrust level for both tip Mach numbers in comparison to experiments. The collective pitch angles simulated were integers, whereas the collective pitch angles in experiments were offset by $\pm$ 0.5°. Additionally, this underprediction may be exacerbated by the turbulence modeling since it neglects laminar flow. The inclusion of laminar flow may provide an increase in predicted thrust and a decrease in predicted torque. To further investigate predicted thrust, sectional thrust distributions were computed for $M_{tip} = 0.65$. Spanwise thrust level was relatively constant, except near the root where the local angle of attack is high, and at the tip where the streamwise vortices released at the sweep break and tip non-linearly affect the produced lift. As seen in Fig. 2.7 thrust level gradually increases outboard of $r/R = 0.9$, culminating in a spike in thrust at $r/R = 0.95$, the location of the sweep break. Baeder et al. [147] performed fully turbulent simulations on the S-76

rotor, finding good agreement with experiments over a collective sweep. However, there was a slight underprediction in FM, generally less than a one count difference.

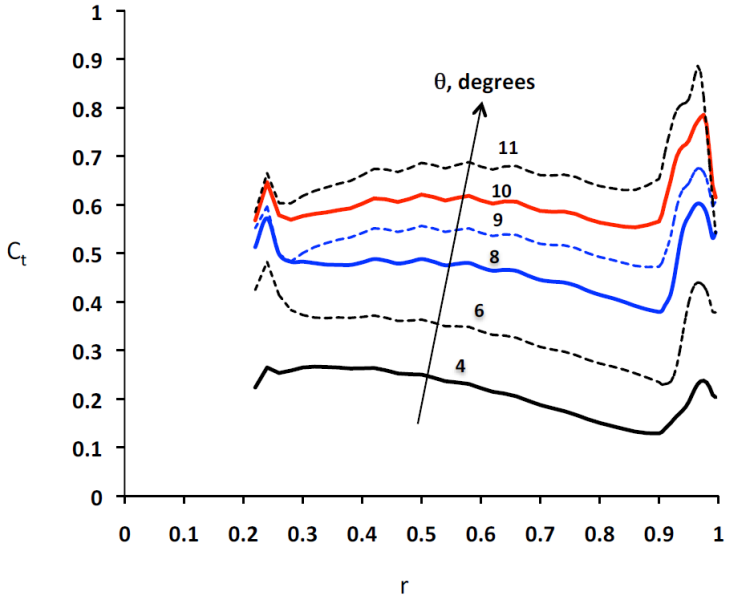


Fig. 2.7 Sectional thrust as a function of blade radius for $M_{tip} = 0.65$ [145]

Sheng et al. [148] investigated the S-76 rotor over several collective pitch angles using the Langtry-Menter transition model. A stall delay modification was implemented into the transition model to suppress flow separation that can occur prematurely in hovering rotor flows. With the transition model, both thrust and torque were overpredicted as a function of collective pitch, which resulted in underpredicting FM by several counts. The addition of the stall delay modification was found to give improved predictions for thrust and torque compared to that of experiments. It was concluded that for low to moderate collective pitch angles, transition prediction is necessary to more accurately predict rotor performance. Similar studies by Min et al. [149] have shown that when using a transition model, predicted FM can vary by several counts for different values of freestream turbulence intensity. Jain later revisited the S-76 rotor [150], simulating the rotor with various tip shapes and a transition model. A hub was added to the rotor system as it was found to damp out the vortex system forming about the root of the rotor, which aided solution convergence and did not affect predicted performance. The transition model greatly overpredicted FM while the fully

turbulent models did not. This suggests that, for the S-76 rotor, the fully turbulent approximation may be more favorable.

2.5.2 PSP Rotor in Hover

Another common rotor in CFD predictions is the pressure sensitive paint (PSP) rotor [6]. Experiments were performed with a four-bladed rotor installed on a ROBIN mod7 fuselage, but many CFD predictions were performed on an uninstalled, isolated rotor. Jain [151] simulated an isolated and installed PSP rotor in hover with and without transition modeling enabled. With the inclusion of the fuselage, there was a one-to-three percent increase in rotor thrust. This can be ascribed to additional upwash through the center of the rotor disk, increasing the effective angle of attack near the root of the blade. This upwash due to the root vortex system interaction with the fuselage can be seen in the rotor wake structure, shown in Fig. 2.8. Predicted thrust was nearly the same for turbulence models with and without transition; however, predicted torque was notably higher when a fully turbulent model was used. The transition model overpredicted FM by about one count for every thrust level, whereas the fully turbulent approach underpredicted FM by three to seven counts.

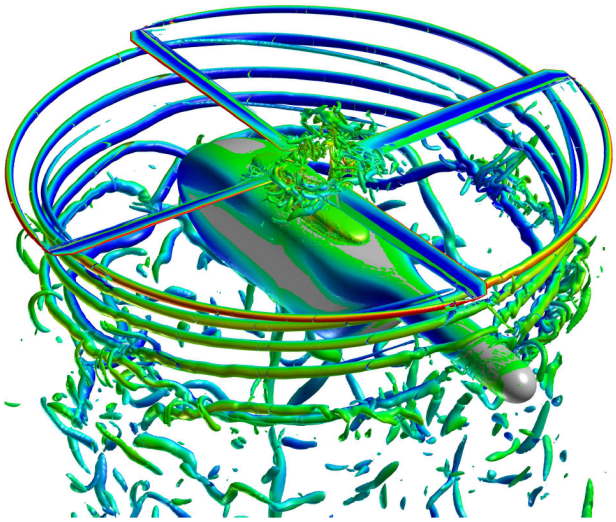


Fig. 2.8 Wake structure of the PSP rotor with ROBIN fuselage in hover visualized via isosurfaces of the Q-criterion, $C_T/\sigma = 0.085$, $M_{tip} = 0.58$ [151]

Vieira et al. [140] simulated the PSP rotor in hover using the AFT transition model of Coder [139]. The transition model overpredicted FM, but transition predictions showed excellent agreement with experimentally determined transition locations, especially for moderate to high collective pitches. In a similar effort, Parwani and Coder [152] simulated the PSP rotor in hover in isolated conditions, finding that the AFT model predicted improved performance over a fully turbulent model. When installing the rotor on the fuselage [153], predicted thrust was higher than for the isolated case. Additionally, fuselage upwash was determined to affect transition locations on the blade surface, especially in the near-root region. Sheng et al. [154] performed transitional simulations on the PSP rotor in hover using 2nd and 4th order WENO reconstruction schemes. When comparing skin friction contours between the two schemes, the 2nd order scheme showed a "smoother" contour, whereas the 4th order scheme showed a more jagged contour, which may be a result of less numerical dissipation. For the higher order scheme, at low to moderate collective pitches, there was a streakiness in the chordwise direction with respect to the transition line, suggesting a stall region near the leading edge or underconverged results. The higher order scheme showed improved tip vortex coherence, shown in Fig. 2.9 compared to the lower order scheme. Additionally, predicted performance correlated well with experiments, suggesting the use of higher order schemes is needed to capture off-body flow features and more accurately predict rotor performance.

Rotors in hover can experience regions of strong crossflow, especially in regions with sweep and BVI events. With transitional rotorcraft simulations becoming more common, accounting for crossflow was the logical next step. Lee et al. [155] simulated the PSP rotor in hover using a transition model with crossflow [156]. The crossflow model showed more turbulent flow on the blade surface, but did not substantially change performance predictions compared to a model without crossflow. Additionally, both the upper and lower surface exhibited irregular behavior in reported transition location using the crossflow model, but this may be due to the use of intermittency surface contours as the transition metric. Hwang and Kwon [157] and Park and Kwon [158] simulated the PSP rotor in hover using a crossflow model that used local sweep angle as the metric to compute the stationary crossflow Reynolds number. Figure of merit was underpredicted by two to six counts in comparison to experiments. Predicted transition location correlated slightly better with experiments when accounting for crossflow. At high collective pitches, the differences

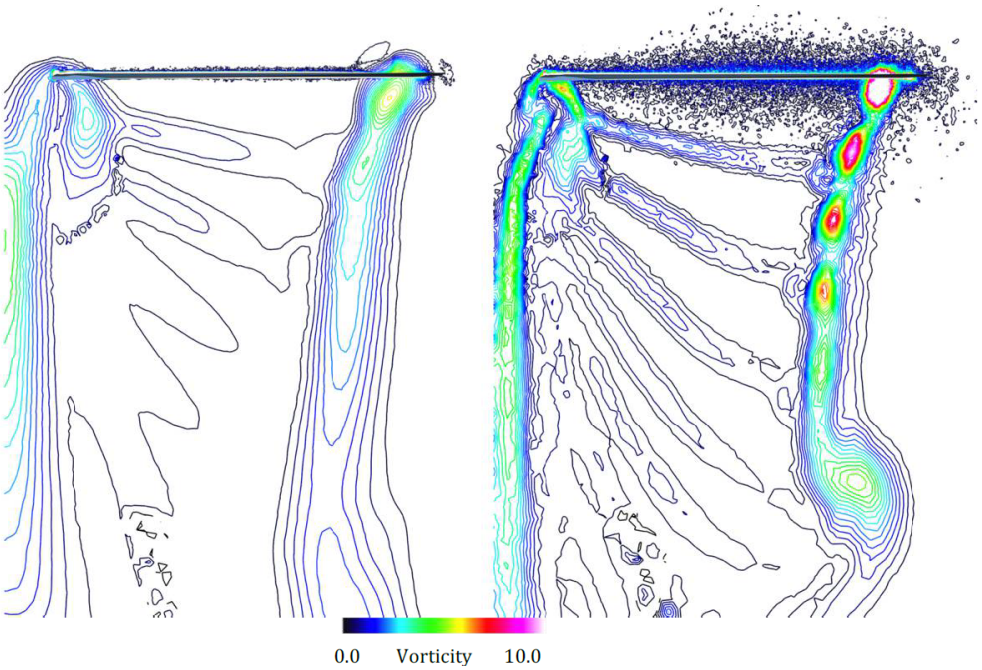


Fig. 2.9 Wake structure of a PSP rotor in hover using 2nd order and 4th order flux reconstruction [154]

in predicted transition between a model with crossflow and without crossflow were negligible on both the upper and lower surfaces, suggesting crossflow may not be needed at high thrust levels.

2.5.3 Forward Flight and CFD-CSD Coupling

The inherent difficulties of rotorcraft simulation are especially confounded for rotorcraft in forward flight. The grids need to be resolved several blade radii in the aft direction in order to capture the wake vortex structure, and also must be resolved below the rotor in order to capture wake travel downward due to wake skew. The rotor must be trimmed to the desired flight envelope, for which these variables can be computed by coupling a CFD solver with a computational structural dynamics (CSD) solver. This coupling method passes aerodynamic information from the CFD solution to the CSD solver (such as CAMRAD or RCAS), which uses a low-fidelity aerodynamic method to estimate the required trim variables. This information typically is exchanged every quarter to full revolution in an approach dubbed “loose-coupling”. The concept of CFD-CSD coupling was pioneered in the 1980s by Tung et al. [159] who coupled a finite-difference solver

to the comprehensive rotor analysis software CAMRAD II [53]. By passing lift information from the CFD solver to the CSD solver, the predicted inflow between the two solvers can be matched and the rotor can be trimmed. Later, Strawn and Tung [160] improved such a coupling procedure by coupling CAMRAD II to a full potential rotor code. This method coupled the two solvers over the full rotor azimuth and exhibited good prediction of surface pressure distributions for a model BVI problem. Attempts to improve solution physicality by including pitching moments caused divergence in predicted blade torsion [161, 162]. These divergence issues were not a function of the coupling procedure, but were a result of inadequate prediction of pitching moments in transonic conditions and inconsistencies between grid motion and blade deformation [163]. When coupling a CSD code to Euler codes, airload prediction becomes considerably more accurate [164, 165]. Unfortunately, Euler codes have shown that predicted pitching moments do not match well with experiments, ascribed to the inviscid assumption. When using a Navier-Stokes solver, the predicted pitching moments and sectional loads show slightly improved correlation with experimental data [165]. Such a comparison is shown in Fig. 2.10.

Potsdam et al. [166] coupled the robust, Navier-Stokes solver OVERFLOW-D with CAMRAD II using a loose coupling approach. Predicted force and moment coefficients using only CAMRAD II gave poor results versus the loose coupling approach with OVERFLOW-D. This approach passed information between solvers once every rotor revolution and proved to be computationally inexpensive. This loose coupling procedure has been applied for a range of rotorcraft flows such as forward flight [167], blade-vortex interaction airload predictions [168], morphing rotor blade technology [169], co-axial rotors [170], rotor-airframe interactions [171], and rotor acoustics [172]. Such procedures are considered state-of-the-art for rotorcraft in forward flight conditions. However, these contemporary works utilize fully turbulent models and do not account for boundary layer transition. Experiments have shown this may be an incorrect assumption [173] and the influence of transition modeling should be investigated.

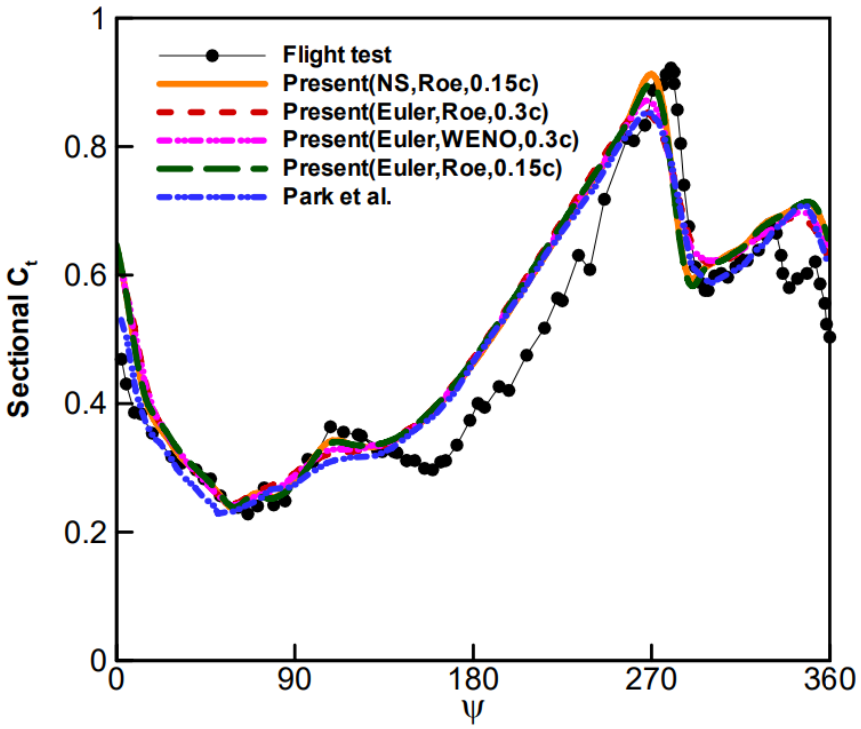


Fig. 2.10 Sectional thrust versus azimuth at r/R = 0.97 predicted using coupled CFD-CSD for the AH-1G rotor [165]

Chapter 3: Experiments and Validation Cases

Experimental studies in the aerodynamics community are necessary in order to validate novel and existing CFD methods. Such experiments can encompass force and moment data, acoustic noise, geometric variation, and boundary layer transition locations. This study focuses on transition prediction and thus discussed here are validation experiments and test cases suggested by Coder [174] that include boundary layer transition data in addition to computational experiments performed on two different rotor geometries.

3.1 Rotorcraft Experimental Tests

3.1.1 The Pressure Sensitive Paint Rotor Experiments

The Pressure Sensitive Paint (PSP) was designed by NASA and the United States Army to test novel methods of surface pressure visualization. Testing by Overmeyer and Martin [6] at NASA Langley collected hovering rotor performance data in addition to boundary layer transition locations for a four-bladed PSP rotor. Transition locations were determined using the infrared thermography technique. This technique is based on the difference in heat transfer between a laminar and a turbulent boundary layer, which can be detected visually using an infrared camera. About 575 images were taken at each thrust condition, which were subsequently averaged together to create a composite image. This average was then used to extract the chordwise transition locations as a function of blade radius. It is of note that the reported transition location is not transition onset, but is at the end of the transition region, where the flow is fully turbulent. To quantify the effect of laminar flow, trip dots were placed near the leading edge of the blade ($0.05c$) during some experiments. This fixes the transition location on the surface on which trip dots are placed. Thus, any combination of natural transition and fixed transition on each blade surface is possible. These hover tests were performed with a tip Mach number of 0.58 and examined thrust conditions ranging

between $C_T/\sigma = 0.03 - 0.10$. Each thrust condition tested has a reported collective pitch, torque coefficient, figure of merit (FM), and transition locations along the blade span. Additionally, each thrust condition was performed with all combinations of natural transition and fixed transition boundary layers. A schematic of the test setup is shown below in Fig. 3.1.

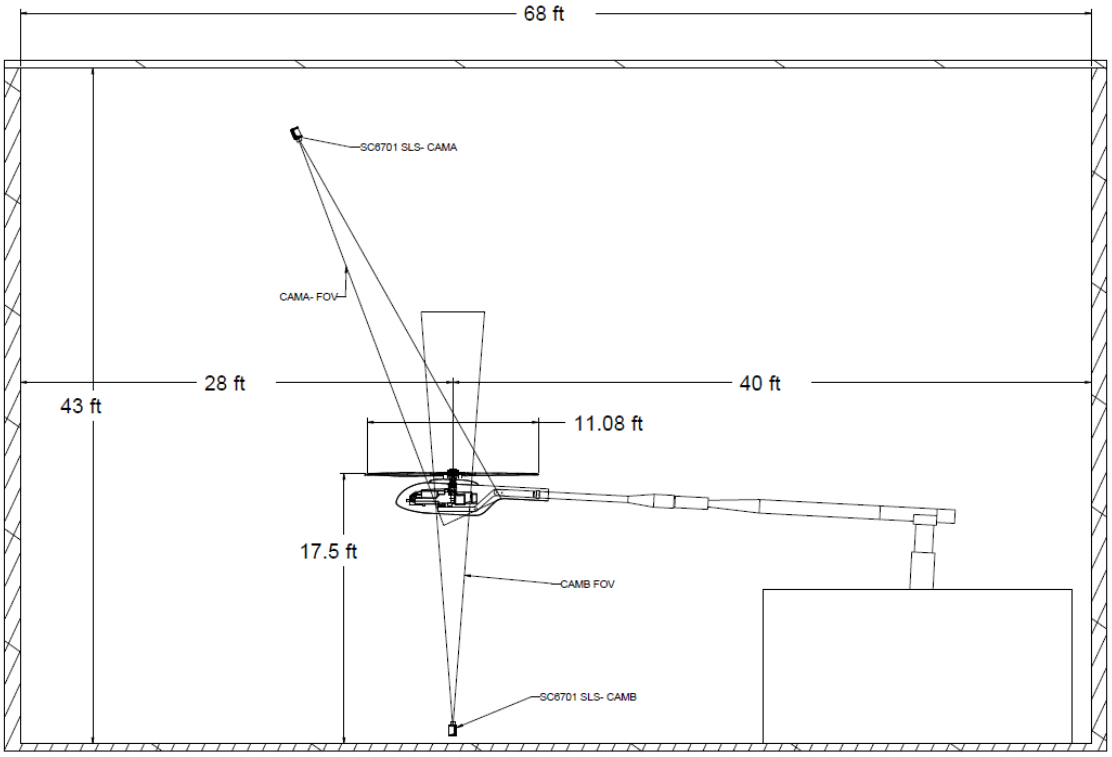


Fig. 3.1 PSP hover test schematic [6]

The fuselage used was the Rotor Body Interaction mod7 (ROBIN) fuselage [175], which was designed to represent a generic transport-class helicopter and was initially used for active flow control experimental studies. The four-bladed PSP rotor was mounted at the center of the hub. To keep the tip path plane horizontal, the fuselage was pitched down -3.5°.

Additional experimental studies on the PSP rotor in forward flight were performed by Overmeyer et al. [173] at the NASA Langley 14 by 22 foot subsonic tunnel. A three-bladed PSP rotor was installed onto a ROBIN mod7 fuselage and was trimmed to zero 1/rev flapping in forward flight. The hub of the ROBIN fuselage was removed and the blades were moved radially outward by 0.5" due to a different choice of hub hinge. A range of advance ratios, thrust conditions, and rotor

shaft angles were tested for which boundary layer transition data were gathered. In forward flight, boundary layer transition is additionally a function of azimuthal position and has its own motion, and is thus considered to be unsteady. Traditional infrared thermography techniques are insufficient for bodies in motion as they cannot properly account for the moving transition line across the rotor azimuth. Thus, a technique called differential infrared thermography (DIT) is used. DIT is based on the difference between two given thermographic images and analyzes this difference to capture unsteady boundary layer transition motion. The optical setup consisted of a high-speed infrared camera with a rotating mirror assembly to reduce motion blur. The camera was capable of imaging every 3.3° degrees of rotor rotation, with a shutter speed corresponding to 1.5° of rotor rotation. The camera system was mounted to a turntable which could encompass 45° of the rotor disk. After data were collected over this range, the turntable was moved to collect data on a different region of the rotor disk. Due to facility limitations, infrared images were only taken on the lower surface of the rotor and thus only lower surface transition locations are known. A picture of the PSP-ROBIN system in the tunnel is given in Fig. 3.2.

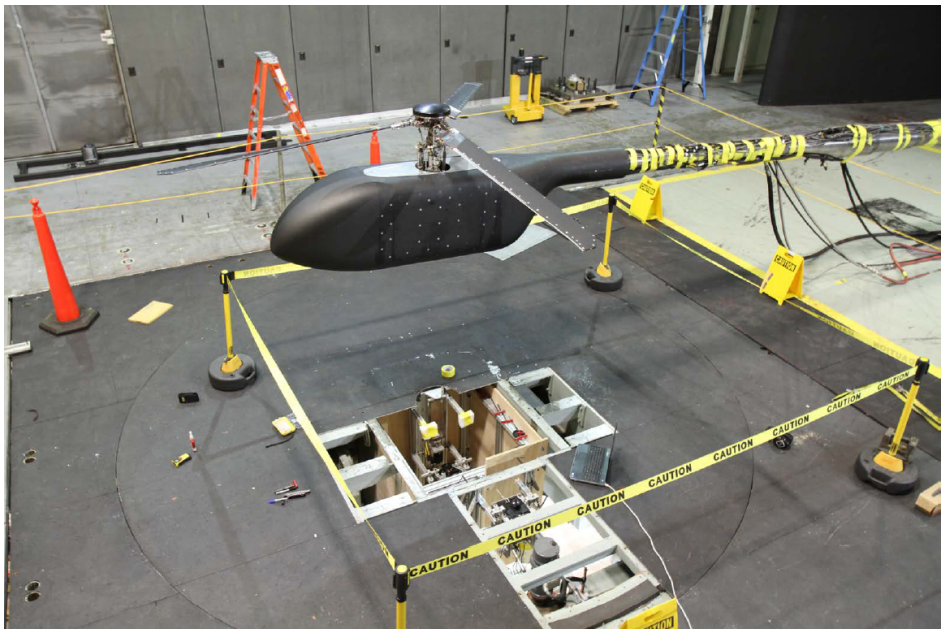


Fig. 3.2 PSP-ROBIN experimental setup for forward flight [173]

3.1.2 The S-76 Rotor Experiments

The S-76 rotor was tested at the Sikorsky Model Hover Test Facility by Balch and Lombardi in order to study advanced main rotor tip geometries and their interactional effects on the tail rotor for rotorcraft vehicles [144]. These tests collected hover performance data for a four-bladed rotor in isolation and in the presence of a tail rotor for a range of hover tip Mach numbers and tip geometries. The data acquisition system was capable of recording the collective pitch, thrust generated, and torque required, from which force and moment coefficients were computed. The Sikorsky Model Hover Test Facility had walls which could be rolled-up in order to allow rotor testing largely in free air. The height of the rotor could be varied by 25 feet in order to perform tests in-ground-effect (IGE) and out-of-ground-effect (OGE). OGE tests were performed at a non-dimensional height of $z/R = 3.0$, which was about 14 feet. The isolated S-76 rotor was tested with five different tip geometries: swept tapered tip, rectangular tip, unswept tapered tip, swept untapered tip, and a swept tapered tip with anhedral, shown in Fig. 3.3. All tips were tested at three tip Mach numbers OGE and one tip Mach number for two IGE conditions. Although the S-76 experiments do not include boundary layer transition, the suite of test data serves as a valuable repository for CFD model validation and is used as such in this study.

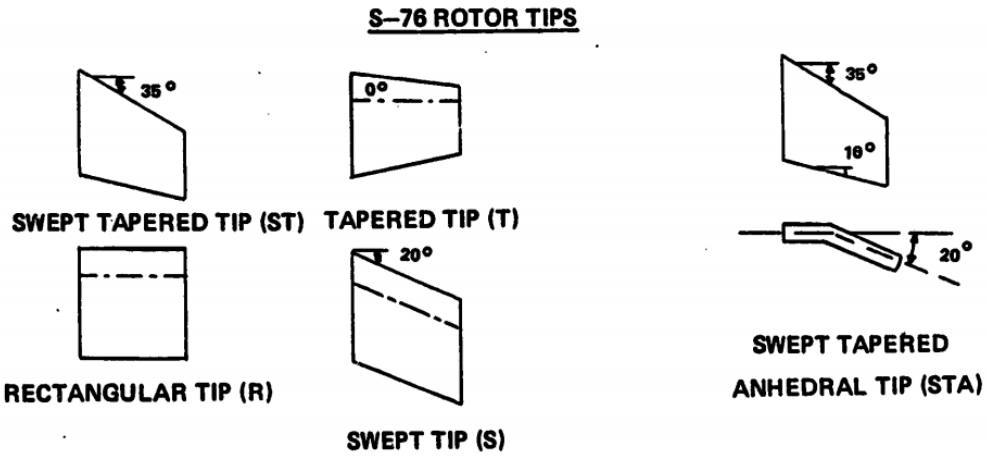


Fig. 3.3 S-76 advanced tip geometries used in testing [144]

3.2 Crossflow Validation Test Cases

3.2.1 NLF(2)-0415 Infinite Swept Wing

Experimental tests by Dagenhart et al. [176] and Radeztsky et al. [177] using an NLF(2)-0415 wing with 45° of sweep, operating at conditions where the growth of stationary crossflow instabilities is amplified, while the growth of Tollmien-Schlichting instabilities is minimized. Tested over a range of Reynolds number at -4° angle of attack, the crossflow instabilities grow such that transition should occur upstream of the pressure minimum at $x/c = 0.71$, especially as Reynolds number increases. Transition locations were recorded using a naphthalene visualization technique with a 9 μm surface roughness. This roughness is a small fraction of the crossflow wavelength, which serves to ensure the initial amplitude of the wave grows due to a small streamwise vortex. The swept wing was installed in the tunnel such that it spanned the full width, which renders the wing as an infinite swept airfoil. These experiments and their data serve as a common test case for crossflow transition model validation [7, 12] and are used as such herein.

3.2.2 6:1 Inclined Prolate Spheroid

The 6:1 inclined prolate spheroid was designed and tested at DFVLR (now DLR) in Göttingen in order to study three-dimensional boundary layers for CFD model validation [178–180]. The spheroid features a semi-major axis six times larger than its semi-minor axis described by the equation,

$$x^2 + 36y^2 + 36z^2 = \frac{1}{4} \tag{3.1}$$

where $x = [-0.5, 0.5]$ and can be scaled accordingly to arbitrary dimensions. The model was tested in the 3 by 3 meter Low Speed Wind Tunnel at the DFVLR Aerodynamics Research Institute over a sweep of angles of attack, Reynolds numbers, and Mach numbers. Predicting transition for this test case is especially difficult due to its fuselage-like geometry, whereas transition models are often calibrated and designed for wing-like geometries. Its curvature also lends to strong crossflow due to streamwise vortices rolling up the surface, rendering it an especially difficult transition predicting test case.

3.2.3 TU Braunschweig Sickle Wing

Petzold and Radespiel [181] designed and tested a sickle-shaped wing in order to study amplification of crossflow instabilities and provide another challenging test case for CFD model validation. The wing features spanwise varying sweep angles such that crossflow instabilities are amplified outboard. As shown in Fig. 3.4, there are three increasingly swept sections of the wing in addition to an unswept section at the root to prevent contamination from the tunnel wall boundary layer. Experiments on the sickle wing were performed over a range of angles of attack, Reynolds numbers, and freestream Mach numbers, each of which has transition locations measured using infrared thermography. The large changes in sweep at section breaks challenge conventional methods of crossflow transition prediction and lends itself to a difficult transition modeling test case.

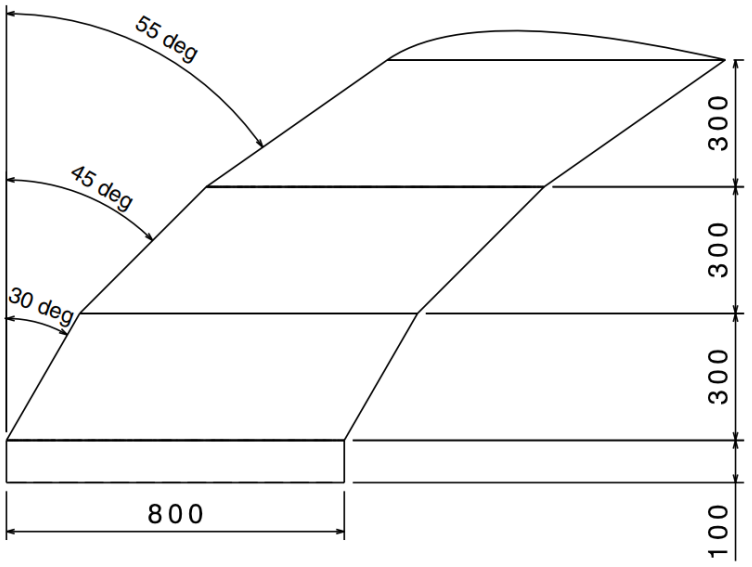


Fig. 3.4 TU Braunschweig sickle wing planform [181]

Chapter 4: Computational Methodology

4.1 Governing Equations

Computational experiments in this study utilize OVERFLOW 2.2n [182], a density-based, node-centered, Reynolds-averaged Navier-Stokes solver developed and maintained by NASA. OVERFLOW uses structured, overset grids with implicit time marching and is capable of simulating axisymmetric, two-dimensional, and three-dimensional geometries. The code supports six degree-of-freedom motion and automated off-body grid generation, rendering it useful for rotorcraft. OVERFLOW solves the Navier-Stokes equations in generalized, curvilinear coordinates [183],

$$\frac{\partial \vec{q}}{\partial t} + \frac{\partial}{\partial \xi}\left(\vec{E} - \vec{E_v}\right) + \frac{\partial}{\partial \eta}\left(\vec{F} - \vec{F_v}\right) + \frac{\partial}{\partial \zeta}\left(\vec{G} - \vec{G_v}\right) = 0 \tag{4.1}$$

where $\vec{q}$ is the vector of conserved variables and the inviscid fluxes $\vec{E}, \vec{F}, \vec{G}$ are given as,

$$\vec{q} = J^{-1}\begin{bmatrix} \rho \\ \rho u \\ \rho v \\ \rho w \\ \rho e_0 \end{bmatrix}, \quad \vec{E} = J^{-1}\begin{bmatrix} \rho U \\ \rho u U + \xi_x P \\ \rho v U + \xi_y P \\ \rho w U + \xi_z P \\ U(\rho e_o + P) - \xi_t P \end{bmatrix}, \quad \vec{F} = J^{-1}\begin{bmatrix} \rho V \\ \rho u V + \eta_x P \\ \rho v V + \eta_y P \\ \rho w V + \eta_z P \\ V(\rho e_o + P) - \eta_t P \end{bmatrix},$$

$$\vec{G} = J^{-1}\begin{bmatrix} \rho W \\ \rho u W + \zeta_x P \\ \rho v W + \zeta_y P \\ \rho w W + \zeta_z P \\ V(\rho e_o + P) - \zeta_z P \end{bmatrix} \tag{4.2}$$

for which the contravariant velocities U, V, W, are the equivalent of cell face-normal velocities,

$$\begin{aligned} U &= \xi_t + \xi_x u + \xi_y v + \xi_z w \\ V &= \eta_t + \eta_x u + \eta_y v + \eta_z w \\ W &= \zeta_t + \zeta_x u + \zeta_y v + \zeta_z w \end{aligned} \tag{4.3}$$

subscript v denotes the viscous flux terms,

$$\vec{E_v} = J^{-1} \begin{bmatrix} 0 \\ \xi_x \tau_{xx} + \xi_y \tau_{xy} + \xi_z \tau_{xz} \\ \xi_x \tau_{yx} + \xi_y \tau_{yy} + \xi_z \tau_{yz} \\ \xi_x \tau_{zx} + \xi_y \tau_{zy} + \xi_z \tau_{zz} \\ \xi_x \beta_x + \xi_y \beta_y + \xi_z \beta_z \end{bmatrix}, \quad \vec{F_v} = J^{-1} \begin{bmatrix} 0 \\ \eta_x \tau_{xx} + \eta_y \tau_{xy} + \eta_z \tau_{xz} \\ \eta_x \tau_{yx} + \eta_y \tau_{yy} + \eta_z \tau_{yz} \\ \eta_x \tau_{zx} + \eta_y \tau_{zy} + \eta_z \tau_{zz} \\ \eta_x \beta_x + \eta_y \beta_y + \eta_z \beta_z \end{bmatrix},$$

$$\vec{G_v} = J^{-1} \begin{bmatrix} 0 \\ \zeta_x \tau_{xx} + \zeta_y \tau_{xy} + \zeta_z \tau_{xz} \\ \zeta_x \tau_{yx} + \zeta_y \tau_{yy} + \zeta_z \tau_{yz} \\ \zeta_x \tau_{zx} + \zeta_y \tau_{zy} + \zeta_z \tau_{zz} \\ \zeta_x \beta_x + \zeta_y \beta_y + \zeta_z \beta_z \end{bmatrix} \tag{4.4}$$

and

$$\begin{aligned} \tau_{xx} &= \lambda(u_x + v_y + w_z) + 2\mu u_x & \tau_{xy} &= \tau_{yx} = \mu(u_y + v_x) \\ \tau_{xz} &= \tau_{zx} = \mu(u_z + w_x) & \tau_{yy} &= \lambda(u_x + v_y + w_z) + 2\mu v_y \\ \tau_{yz} &= \tau_{zy} = \mu(v_z + w_y) & \tau_{zz} &= \lambda(u_x + v_y + w_z) + 2\mu w_z \\ \beta_x &= \gamma\kappa Pr^{-1}\partial_x e_1 + u\tau_{xx} + v\tau_{xy} + w\tau_{xz} & \beta_y &= \gamma\kappa Pr^{-1}\partial_y e_1 + u\tau_{yx} + v\tau_{yy} + w\tau_{yz} \\ \beta_z &= \gamma\kappa Pr^{-1}\partial_x e_1 + u\tau_{zx} + v\tau_{zy} + w\tau_{zz} & e_1 &= e\rho^{-1} - \frac{1}{2}(u_2 + v^2 + w^2) \end{aligned}$$

where λ is Stokes' hypothesis ($\lambda = -2/3\,\mu$), μ is the dynamic viscosity, κ is the thermal conductivity, and Pr is the Prandtl number. Pressure is given by the ideal gas law as,

$$P = (\gamma - 1)\Big[e - \frac{1}{2}\rho(u^2 + v^2 + w^2)\Big] \tag{4.5}$$

The spatial gradients of velocity can be computed from the Jacobian matrix and transformation derivatives. The Jacobian is given as,

$$J^{-1} = x_\xi y_\eta z_\zeta + x_\zeta y_\xi z_\eta + x_\eta y_\zeta z_\xi - x_\xi y_\zeta z_\eta - x_\eta y_\xi z_\zeta - x_\zeta y_\eta z_\xi \tag{4.6}$$

Finally, the transformation derivatives are,

$$\begin{aligned}
\xi_x &= J(y_\eta z_\zeta - y_\zeta z_\eta) & \zeta_x &= J(y_\xi z_\eta - z_\xi y_\eta) \\
\xi_y &= J(z_\eta x_\zeta - x_\eta z_\zeta) & \zeta_y &= J(x_\eta z_\xi - x_\xi z_\eta) \\
\xi_z &= J(x_\eta y_\zeta - y_\eta x_\zeta) & \zeta_z &= J(x_\xi y_\eta - y_\xi x_\eta) \\
\eta_x &= J(z_\xi y_\zeta - y_\xi z_\zeta) & \xi_t &= -x_t\xi_x - y_t\xi_y - z_t\zeta_z \\
\eta_y &= J(x_\xi z_\zeta - x_\zeta z_\xi) & \eta_t &= -x_t\eta_x - y_t\eta_y - z_t\eta_z \\
\eta_z &= J(y_\xi x_\zeta - x_\xi y_\zeta) & \zeta_t &= -x_t\zeta_x - y_t\zeta_y - z_t\zeta_z
\end{aligned}$$

4.1.1 WENO Flux Reconstruction

In order to compute the flux terms of Eq. 4.1, an approximate Riemann solver must be employed in order to compute the cell interface flux for discontinuous, piecewise constant data. Right-running waves from the left side of the interface combine with the left-running waves from the right side of the interface in order to communicate data between cells. In the ξ direction, Eq. 4.1 simplifies to a hyperbolic conservation law that can be solved using a Riemann solver,

$$\frac{\partial \vec{q}}{\partial t} + \hat{A}\frac{\partial q}{\partial \xi} = 0 \tag{4.7}$$

where $\hat{A}$ is some matrix that is constant across the cell interface. The formal accuracy of such Riemann solvers is restricted by the accuracy of the values computed at just to the left and right

of the grid cell face, which are used to reconstruct the flux at the interface between cells. By achieving a higher-order reconstruction of the flux values adjacent to the cell face, the order of overall solution accuracy can be improved. Thus, there is a desire to employ higher-order reconstruction methods when possible. However, higher-order reconstruction methods can exhibit oscillations in regions of high gradients, such as shocks, which are inherently non-physical. The weighted essentially non-oscillatory (WENO) flux reconstruction scheme [184] achieves a higher-order reconstruction by using a convex sum of lower-order reconstruction stencils with carefully chosen weights, minimizing solution oscillations. A 5$^{\text{th}}$ order WENO scheme is achievable by a weighted sum of three parabolic reconstructions which are used to compute the fluxes at the left and right side of the interface. These three reconstructions are [185],

$$\begin{aligned} {f_{j+\frac{1}{2}}}^{(1)} &= \frac{1}{3}f_{j-2} - \frac{7}{6}f_{j-1} + \frac{11}{6}f_j \\ {f_{j+\frac{1}{2}}}^{(2)} &= \frac{-1}{6}f_{j-1} - \frac{5}{6}f_j + \frac{1}{3}f_{j+1} \\ {f_{j+\frac{1}{2}}}^{(3)} &= \frac{1}{3}f_j - \frac{5}{6}f_{j+1} + \frac{-1}{6}f_{j+2} \end{aligned} \tag{4.8}$$

which is then used to compute the flux at the interface $j + \frac{1}{2}$, taking the form,

$${f_{j+\frac{1}{2}}}^{L} = \omega_1 {f_{j+\frac{1}{2}}}^{(1)} + \omega_2 {f_{j+\frac{1}{2}}}^{(2)} + \omega_3 {f_{j+\frac{1}{2}}}^{(3)} \tag{4.9}$$

where

$$\omega_k = \frac{\tilde{\omega_k}}{\sum \tilde{\omega_k}} \tag{4.10}$$

$$\tilde{\omega_k} = \frac{\gamma_k}{\epsilon + {\beta_k}^2} \tag{4.11}$$

$$\gamma_1 = \frac{1}{10}, \quad \gamma_2 = \frac{3}{5}, \quad \gamma_k = \frac{3}{10}$$

$${\beta_k}^{(1)} = \frac{13}{12}\Big(f_{j-1} - 2f_j + f_{j+1}\Big)^2 + \frac{1}{4}\Big(f_{j-1} - 4f_j + 3f_{j+1}\Big)^2 \tag{4.12}$$

$${\beta_k}^{(2)} = \frac{13}{12}\Big(f_{j-1} - 2f_j + f_{j+1}\Big)^2 + \frac{1}{4}\Big(f_j - f_{j+2}\Big)^2 \tag{4.13}$$

$${\beta_k}^{(3)} = \frac{13}{12}\Big(f_{j+1} - 2f_{j+2} + f_{j+3}\Big)^2 + \frac{1}{4}\Big(3f_{j+1} - 4f_{j+2} + 3f_{j+3}\Big)^2 \tag{4.14}$$

WENO uses the smoothness indicators β_k to account for contributions from each stencil and adapts the weights ω_k to always sum to one. A symmetric procedure is repeated for ${f_{j+\frac{1}{2}}}^R$ reflected about $f_{j+\frac{1}{2}}$. Because of this, three interpolation points are required on either side of $j+\frac{1}{2}$, called fringe points. For overset methods, it is important to maintain at least three fringe points in order to interpolate the flux at overset boundaries. Then, the fluxes computed using Eq. 4.9 can be fed into a Riemann solver and the process is completed.

4.1.2 Roe Flux-Difference Splitting

In this study, the Roe flux-difference splitting scheme [75] was used, an approximate Riemann solver. The Roe scheme seeks to solve hyperbolic conservation laws, such as Navier-Stokes, by locally linearizing the equation through the cell interface. Given the fluxes computed to the left and right side of the interface from a flux reconstruction scheme such as WENO, the interface flux can be computed and the solution can be stitched together. From Eq. 4.7, $\hat{A}$ in the Roe scheme is the Roe-averaged inviscid flux Jacobian and is constant between adjacent cells. This vector must be diagonalizable such that

$$\hat{A} = \hat{T}\hat{\Lambda}\hat{T}^{-1} \tag{4.15}$$

In order to compute $\hat{A}$, the conserved variables $\vec{q}$ must be averaged across the interface. This weighted average retains the ability to capture shocks and satisfies the Rankine-Hugoniot relations. In one-dimension, these Roe-averaged states are,

$$\hat{\rho} = \sqrt{\rho_L \rho_R} \quad , \quad \hat{u} = \frac{\sqrt{\rho_L}\, u_L + \sqrt{\rho_R}\, u_R}{\sqrt{\rho_L} + \sqrt{\rho_R}} \quad , \quad \hat{h_0} = \frac{\sqrt{\rho_L}\, h_{0_L} + \sqrt{\rho_R}\, h_{0_R}}{\sqrt{\rho_L} + \sqrt{\rho_R}} \tag{4.16}$$

which are then used to compute $\hat{T}$ and $\hat{T}^{-1}$, from which $\hat{A}$ can be computed. With this, the interface flux can be computed as a linear combination of the fluxes from left-running and right-running waves about some interface point $j+\frac{1}{2}$,

$$f_{j+\frac{1}{2}} = \frac{1}{2}(f_L + f_R) - \frac{1}{2}\left|\hat{A}\right|\Big(q_R - q_L\Big) \tag{4.17}$$

where the second term is a dissipation term based on the jump in solution state. This procedure is repeated for both the left and right interface of the cell in question. Next, the difference between

the fluxes with respect to the change in position is used to compute the update in the state vector, that is,

$$\Delta q = \frac{f^R_{j+\frac{1}{2}} - f^L_{j+\frac{1}{2}}}{\Delta x}\,\Delta t \tag{4.18}$$

4.1.3 Diagonalized Diagonal Dominant Alternating Direction Implicit (D3ADI) Scheme

To fully discretize the Navier-Stokes equations and march forward in time, Eq. 4.1 is solved implicitly by assuming the general form $Ax = b$. This allows for an algebraically simple solution method, but the procedure to invert the A matrix can be computationally expensive and numerically stiff. The implicit form of Eq. 4.1 is written using an approximate Jacobian as [186],

$$\begin{aligned}\left[I + \frac{\Delta t}{(1+\theta)\Delta\tau} + \frac{\Delta t}{1+\theta}\Big(\partial_\xi A + \partial_\eta B + \partial_\zeta C\Big)\right]\Delta q^{n+1,m+1} = \\ -\left[\Big(q^{n+1,m} - q^n\Big) - \frac{\theta}{1+\theta}\Delta q^n + \frac{\Delta t}{1+\theta} RHS^{n+1,m}\right]\end{aligned} \tag{4.19}$$

where θ is set to 0 for first-order time marching and is set to $1/2$ for second-order time marching. The variable τ allows for pseudo time marching such that the local timestep may vary at a given point in the flowfield. The term RHS is the right hand side of the Navier-Stokes equation, more specifically,

$$RHS = \frac{\partial}{\partial\xi}\Big(\vec{E} - \vec{E_v}\Big) + \frac{\partial}{\partial\eta}\Big(\vec{F} - \vec{F_v}\Big) + \frac{\partial}{\partial\zeta}\Big(\vec{G} - \vec{G_v}\Big) \tag{4.20}$$

The change in the conserved variables $\Delta q^{n+1,m+1}$ is computed for each iteration in time n and each subiteration m. The implicit solve is performed individually for each grid. At the end of each subiteration, the overset grid boundaries are updated explicitly. Thus, with subiterations, this explicit solve can improve convergence by allowing additional informational exchanges between grids. In order to solve Eq. 4.19, the left-hand side can be approximately factored in space, a problem for which several solution procedures exist. In this work, the diagonalized, diagonally dominant alternating direction implicit (D3ADI) scheme is used [187]. The diagonal alternating

direction implicit (DADI) scheme of Pulliam and Chaussee [188] is given as,

$$X_A\left[I+\frac{\Delta t}{1+\theta}\delta_\xi\Lambda_A\right]{X_A}^{-1}X_B\left[I+\frac{\Delta t}{1+\theta}\delta_\eta\Lambda_B\right]{X_B}^{-1}X_C\left[I+\frac{\Delta t}{1+\theta}\delta_\zeta\Lambda_C\right]{X_C}^{-1}\Delta q^{n+1.m+1}=$$
$$-\left[\left(q^{n+1,m}-q^n\right)-\frac{\theta}{1+\theta}\Delta q^n+\frac{\Delta t}{1+\theta}RHS^{n+1,m}\right] \tag{4.21}$$

The inviscid flux Jacobians are decomposed into their eigenvalues and eigenvectors as,

$$\begin{aligned}\partial_q E=A&=X_A\Lambda_A{X_A}^{-1}\\ \partial_q F=B&=X_B\Lambda_B{X_B}^{-1}\\ \partial_q G=C&=X_C\Lambda_C{X_C}^{-1}\end{aligned} \tag{4.22}$$

By separating Eq. 4.21 into diagonal and off-diagonal terms and then factoring the scheme, the diagonally dominant ADI scheme (DDADI) is obtained. Diagonalizing this scheme gives D3ADI, with full form

$$\begin{aligned}&X_A\left[I+\frac{\Delta t}{1+\theta}{\delta_\xi}^u\Lambda_A+{X_A}^{-1}\Big(D_\eta+D_\zeta\Big)X_A\right]{X_A}^{-1}D^{-1}\\ &X_B\left[I+\frac{\Delta t}{1+\theta}{\delta_\eta}^u\Lambda_B+{X_B}^{-1}\Big(D_\xi+D_\zeta\Big)X_B\right]{X_B}^{-1}D^{-1}\\ &X_C\left[I+\frac{\Delta t}{1+\theta}{\delta_\zeta}^u\Lambda_C+{X_C}^{-1}\Big(D_\xi+D_\eta\Big)X_C\right]{X_C}^{-1}\Delta q^{n+1,m+1}=\\ &-\left[\left(q^{n+1,m}-q^n\right)-\frac{\theta}{1+\theta}\Delta q^n+\frac{\Delta t}{1+\theta}RHS^{n+1,m}\right]\end{aligned} \tag{4.23}$$

where D is a matrix containing all of the diagonal terms of Eq. 4.21 and δ^u is a differencing operator that is either forward or backward, depending on whether the eigenvalue Λ is positive or negative.

4.2 Turbulence Closure

4.2.1 Spalart-Allmaras Eddy Viscosity Model

For turbulence closure of the Navier-Stokes equations, the Spalart-Allmaras (SA) [94] eddy viscosity model is used. More specifically, the SA-neg [95] variant of the model is used, which handles cases where the working variable $\tilde{\nu_t}$ is negative. When $\tilde{\nu_t}<0$ the eddy viscosity is set to

zero, and for $\tilde{\nu_t} > 0$ the original SA formulation is unchanged. Additionally, this formulation is energy stable and forces negative transient values eventually to zero. The baseline SA model is,

$$\frac{D\tilde{\nu}}{Dt} = c_{b1}\tilde{S}\tilde{\nu}(1 - f_{t2}) - \left(c_{w1}f_w - \frac{c_{b1}}{\kappa^2}f_{t2}\right)\left(\frac{\tilde{\nu}}{d}\right)^2 + \frac{1}{\sigma}\left[\frac{\partial}{\partial x_j}\left((\nu + \tilde{\nu})\frac{\partial\tilde{\nu}}{\partial x_j}\right) + c_{b2}\frac{\partial\tilde{\nu}}{\partial x_j}\frac{\partial\tilde{\nu}}{\partial x_j}\right] \quad (4.24)$$

For which the eddy viscosity is defined as.

$$\nu_t = \tilde{\nu_t} f_{\nu 1} \quad (4.25)$$

where these subfunctions are a damping function

$$f_{\nu 1} = \frac{\chi^3}{\chi^3 + {c_{\nu 1}}^3} \quad (4.26)$$

and a turbulent Reynolds number

$$\chi = \frac{\tilde{\nu}}{\nu} \quad (4.27)$$

The first term on the right-hand side of Eq. 4.24 is for turbulence production as a function of the vorticity magnitude and modified eddy viscosity, where

$$\tilde{S} = \Omega + \frac{\tilde{\nu}}{\kappa^2 d^2} f_{v1} \quad (4.28)$$

$$f_{\nu 2} = 1 - \frac{\chi}{1 + \chi f_{v1}} \quad (4.29)$$

The term f_{t2} allows for a laminarization effect of the boundary layer and can be used to explicitly specify a transition location and is modified when coupling a transition model to the SA model. The original, unmodified formulation is,

$$f_{t2} = c_{t3} \exp\Big(- c_{t4}\, \chi^2 \Big) \quad (4.30)$$

The destruction term is based on shear stress destruction due to the blocking effect of the wall and directly uses wall-distance. Although the destruction term also features f_{t2}, this term serves to cancel its own effects in fully turbulent boundary layers without affecting the stability of a laminar

solution. The formulations used in the production term are,

$$f_w = g(r)\left(\frac{1+{c_{w3}}^6}{g(r)^6+{c_{w3}}^6}\right)^{1/6} \tag{4.31}$$

where

$$g(r) = r + c_{w2}(r^6 - r) \tag{4.32}$$

$$r = \min\left[\frac{\tilde{\nu}}{\tilde{S}\kappa^2 d^2}, 10\right] \tag{4.33}$$

Calibration constants for this model are suggested as,

$$\sigma = 2/3\,, \quad c_{b1} = 0.1355\,, \quad c_{b2} = 0.622\,, \quad \kappa = 0.41\,, \quad c_{w2} = 0.3 \tag{4.34}$$

$$c_{w3} = 2\,, \quad c_{v1} = 7.1\,, \quad c_{t3} = 1.2\,, \quad c_{t4} = 0.5 \tag{4.35}$$

$$c_{w1} = \frac{c_{b1}}{\kappa^2} + \frac{1+c_{b2}}{\sigma} \tag{4.36}$$

Linear eddy viscosity models do not well account for rotation or curvature which can greatly impact turbulent shear flows. To account for such effects, the rotation/curvature (RC) correction of Spalart and Shar is used [96], which is an empirical formulation that can account for RC effects in a Galilean-invariant manner. This method tracks the principal axes of the strain rate tensor which allows for such Galilean invariance. Tracking rotation effects in a Galilean-invariant manner is especially important for rotorcraft flows due to the inherently vortical flowfield. The RC effects are accounted for by multiplying the production term of Eq. 4.24 by

$$f_{r1} = (1+c_{r1})\frac{2r^*}{1+r^*}\left[1 - c_{r3}\tan^{-1}(c_{r2}\,\tilde{r})\right] - c_{r1} \tag{4.37}$$

for which

$$r^* = S/\omega \tag{4.38}$$

$$\tilde{r} = \frac{2\omega_{ik}S_{jk}}{D^4}\left(\frac{DS_{ij}}{Dt} + (\epsilon_{imn}S_{jn} + \epsilon_{jmn}S_{in})\Omega_m{}'\right) \tag{4.39}$$

where the tensor terms are written as,

$$S_{ij} = \frac{1}{2}\left(\frac{\partial u_i}{\partial x_j} + \frac{\partial u_j}{\partial x_i}\right) \tag{4.40}$$

$$\omega_{ij} = \frac{1}{2}\left[\left(\frac{\partial u_i}{\partial x_j} - \frac{\partial u_j}{\partial x_i}\right) + 2\epsilon_{mji}\Omega_m{}'\right] \tag{4.41}$$

$$S = \sqrt{2S_{ij}S_{ij}} \tag{4.42}$$

$$\omega = \sqrt{2\omega_{ij}\omega_{ij}} \tag{4.43}$$

$$D = \sqrt{\frac{1}{2}\left(S^2 + \omega^2\right)} \tag{4.44}$$

Finally, the calibration constants are,

$$c_{r1} = 1.0\,, \quad c_{r2} = 12.0\,, \quad c_{r3} = 1.0 \tag{4.45}$$

4.2.2 Amplification Factor Transport Model

In order to more accurately model flow physics, a transition model is used to account for laminar flow. Coder [11] and Coder and Maughmer [139] developed the amplification factor transport (AFT) model, which is a CFD-compatible transition model that is capable of predicting laminar-turbulent boundary layer transition. The model seeks to track the family of linear instabilities in a two-dimensional (i.e. streamwise-oriented) boundary layer based on e^N theory by use of a transported amplification factor $\tilde{n}$ used to determine transition onset. The first transport equation is

$$\frac{\partial \rho\tilde{n}}{\partial t} + \frac{\partial \rho u_j\tilde{n}}{\partial x_j} = \rho\Omega F_{crit}F_{growth}\frac{d\tilde{n}}{dRe_\theta} + \frac{\partial}{\partial x_j}\left[\sigma_n(\mu + \mu_t)\frac{\partial\tilde{n}}{\partial x_j}\right] \tag{4.46}$$

However, this equation relies on computation of integral boundary layer parameters such as the shape factor and momentum thickness. These values are inherently difficult to compute in CFD methods as non-local searches must be performed in order to define a boundary layer edge. The AFT model circumvents this by estimating the integral boundary layer parameters via a local characteristic shape factor,

$$H_L = \frac{d^2}{\nu}\left[\nabla(\vec{u}\cdot\nabla d)\cdot\nabla d\right] \tag{4.47}$$

This shape factor is Galilean-invariant and is used to estimate the integral boundary layer properties, which are then used to compute the production term. Based on this, the integral boundary layer shape factor is,

$$H_{12} = \min[\,\max(0.26H_L + 2.4, 20.0), 2.2\,] \tag{4.48}$$

which has a minimum value of 2.2 to maintain physicality and ensure that growth of the amplification factor is not inadvertently destroyed. The working variable $\tilde{n}$ is largely defined by its growth with respect to the momentum thickness Reynolds number,

$$\frac{d\tilde{n}}{dRe_\theta} = 0.028\Big(H_{12} - 1\Big) - 0.0345\exp\bigg[-\bigg(\frac{3.87}{H_{12}-1} - 2.52\bigg)^2\bigg] \tag{4.49}$$

Thus, the momentum thickness need not be explicitly computed in this formulation. However, the critical momentum thickness Reynolds number is still needed, which is accounted for in,

$$F_{crit} = \begin{cases} 0, & Re_{\mathbf{V}} < Re_{\mathbf{V},0} \\ 1, & Re_{\mathbf{V}} \geq Re_{\mathbf{V},0} \end{cases} \tag{4.50}$$

where $Re_{\mathbf{V}}$ is the vorticity Reynolds number

$$Re_{\mathbf{V}} = \frac{\rho S d^2}{\mu + \mu_t} \tag{4.51}$$

$$Re_{\mathbf{V},0} = k_{\mathbf{V}} Re_{\theta,0} \tag{4.52}$$

$k_{\mathbf{V}}$ describes the proportionality of the vorticity Reynolds number and momentum thickness Reynolds number,

$$k_{\mathbf{V}} = \frac{1}{0.4036{H_{12}}^2 - 2.5394H_{12} + 4.3273} \tag{4.53}$$

$$\log_{10}\Big(Re_{\theta,0}\Big) = 0.7\tanh\bigg(\frac{14}{H_{12}-1} - 9.24\bigg) + \frac{2.492}{(H_{12}-1)^{0.43}} + 0.62 \tag{4.54}$$

The physical growth of the boundary layer is taken into account with,

$$F_{growth} = D(H_{12})\frac{1+m(H_{12})}{2}\,l(H_{12}) \tag{4.55}$$

$$D(H_{12}) = \frac{2.4\,H_{12}}{H_{12}-1} \tag{4.56}$$

$$l(H_{12}) = \frac{6.54\,H_{12}-14.07}{{H_{12}}^2} \tag{4.57}$$

$$m(H_{12}) = \frac{1}{l(H_{12})}\left[0.058\,\frac{(H_{12}-4)^2}{H_{12}-1} - 0.068\right] \tag{4.58}$$

The second transported quantity is the modified intermittency, defined as the natural logarithm of the actual intermittency. Intermittency is used to suppress turbulent production in laminar boundary layers and also activates turbulent production in turbulent boundary layers. This equation is given as,

$$\frac{\partial\rho\tilde{\gamma}}{\partial t}+\frac{\partial\rho u_j\tilde{\gamma}}{\partial x_j} = c_1\rho S F_{onset}\Big[1-\exp(\tilde{\gamma})\Big]+c_2\rho\Omega F_{turb}\Big[c_3\exp(\tilde{\gamma})-1\Big]+\frac{\partial}{\partial x_j}\left[\Big(\mu+\frac{\mu_t}{\sigma_y}\Big)\frac{\partial\tilde{\gamma}}{\partial x_j}\right] \tag{4.59}$$

The calibration constants are given as $c_1 = 100$, $c_2 = 0.6$, and $c_3 = 50$. The function for turbulence onset, F_{onset}, is a measure of the transition criterion and also the turbulence in the boundary layer.

$$F_{onset,1} = \frac{\tilde{n}}{N_{crit}} \tag{4.60}$$

where N_{crit} is the critical amplification factor and is used to indicate transition once $\tilde{n}$ exceeds this value. The critical amplification factor is suggested by Mack [189] as,

$$N_{crit} = -8.43 - 2.4\ln\Big(\frac{\tau}{100}\Big) \tag{4.61}$$

where τ is given by Drela and Youngren [190] as,

$$\tau = 2.5\tanh\left(\frac{Tu(\%)}{2.5}\right) \tag{4.62}$$

To limit excessive production,

$$F_{onset,2} = \min(F_{onset1}, 2.0) \tag{4.63}$$

As a measure of turbulence in the boundary layer,

$$F_{onset,3} = \max\left[1 - \left(\frac{R_T}{3.5}\right)^3, 0\right] \tag{4.64}$$

which is designed to be zero in turbulent boundary layers. The characteristic turbulence Reynolds number is,

$$R_T = \frac{\mu_t}{\mu} \tag{4.65}$$

Finally,

$$F_{onset} = \max\Big[F_{onset,2} - F_{onset,3}, 0\Big] \tag{4.66}$$

The destruction term aims to prevent re-laminarization in turbulent boundary layers where the turbulence Reynolds number R_T is large, but allows re-laminarization in boundary layers where the turbulence Reynolds number is small.

$$F_{turb} = \exp\left[-\left(\frac{R_T}{2}\right)^4\right] \tag{4.67}$$

The AFT model is paired with the SA model in order to model turbulence production. This coupling is achieved through modifying the f_{t2} term of the SA model.

$$f_{t2} = c_{t3}[1 - \exp(\tilde{\gamma})] \tag{4.68}$$

where $c_{t3} = 1.2$. This ensures that as intermittency grows, the production term of the SA model grows, which in turn incites turbulence growth such that when intermittency is one, the solution becomes fully turbulent.

4.2.3 Crossflow Transition Modeling

The AFT model in its full form is capable of predicting boundary layer transition as a function of streamwise instabilities. For highly swept or curved geometries or highly rotational flows, transition can be caused by crossflow instabilities. To account for stationary crossflow instabilities, the crossflow model of Langtry et al. [12] is integrated with the AFT model. This model uses local helicity as its measure of crossflow strength, meaning that coupling the crossflow model to

AFT is not a Galilean-invariant formulation due to the explicit use of streamwise vorticity and velocity magnitude. Although this introduces additional uncertainties for rotorcraft flows due to the rotating reference frame, helicity tracks streamwise vortices well and has proven its merit in predicting crossflow transition. The crossflow instabilities are tracked by computing a crossflow shape factor, analogous to a pressure gradient parameter,

$$H_{crossflow} = \frac{y\left|\vec{U}\cdot\vec{\Omega}\right|}{U} \tag{4.69}$$

Additionally, grid motion is subtracted from the velocity vector in the current implementation. On the infinite swept NLF(2)-0415 wing, against which the model was calibrated by Langtry et al. [12], the crossflow shape factor reaches a high value near the leading edge due to curvature effects, after which the shape factor is nearly linear with chordwise position. Additionally, as airfoil sweep increases, the crossflow shape factor also increases, highlighting its use as an indicator for crossflow strength. This shape factor is used to compute a stationary crossflow Reynolds number,

$$Re_{SCF} = \frac{\theta_t \rho\left(\frac{U}{0.82}\right)}{\mu} = -35.088\ln\frac{h}{\theta_t} + 319.51 + f\Big(+\Delta H_{crossflow}\Big) - f\Big(-\Delta H_{crossflow}\Big) \tag{4.70}$$

where h is the surface roughness. The velocity magnitude is divided by 0.82 to account for the difference between freestream velocity and local velocity at which the vorticity Reynolds number reaches its peak value and enforces transition onset. Although the crossflow model was calibrated based on a specific experiment, crossflow strengths less than and greater than that of the NLF(2)-0415 experiment are accounted for with some shift functions for the crossflow shape factor.

$$\Delta H_{Crossflow} = H_{Crossflow}\left(1.0 + \min\Big[1.0\,R_T,\ 0.4\Big]\right) \tag{4.71}$$

As eddy viscosity increases, the crossflow shape factor can decrease, introducing robustness so transition does not falter. This would in turn cause a decrease in crossflow strength, which may induce transition farther downstream than desired. Multiplying by R_T in Eq. 4.71 damps out the inverse relationship between $H_{Crossflow}$ and μ_t, ensuring transition is not consequently delayed.

The up-shift and down-shift in crossflow strength relative to the calibration experiment are,

$$+\Delta H_{Crossflow} = \max\Big[(0.1066 - \Delta H_{Crossflow}),\, 0\Big] \tag{4.72}$$

$$f(+\Delta H_{Crossflow}) = 6200\,(+\Delta H_{Crossflow}) + 50000\,(+\Delta H_{Crossflow})^2 \tag{4.73}$$

$$-\Delta H_{Crossflow} = \max\Big[-(0.1066 - \Delta H_{Crossflow}),\, 0\Big] \tag{4.74}$$

$$f(-\Delta H_{Crossflow}) = 75\tanh\left(\frac{-\Delta H_{Crossflow}}{0.0125}\right) \tag{4.75}$$

To provide an interface with AFT, the stationary crossflow Reynolds number is used to trigger an additional transition criterion. This effect is realized by modifying $F_{onset,1}$ accordingly,

$$F_{onset,1} = \max\left[\frac{\tilde{n}}{N_{crit}}, \frac{Re_v}{2.2Re_{SCF}}\right] \tag{4.76}$$

where Re_v is slightly different from the formulation in Eq. 4.51 in that the eddy viscosity is excluded,

$$Re_v = \frac{\rho S d^2}{\mu} \tag{4.77}$$

In the original formulation of Eq. 4.76, Langtry et al. suggested the crossflow transition criterion be a scaled ratio of vorticity Reynolds number to critical momentum thickness Reynolds number. However, the critical momentum thickness number is a quantity specific to the Langtry-Menter transition model and requires an additional transport equation for its computation. Through testing of the crossflow model, it was found that the stationary crossflow Reynolds number is a viable surrogate and renders the crossflow model fully algebraic.

4.2.4 Hybrid RANS/LES Framework

Intrinsic issues with RANS-based turbulence modeling exist in its ability to predict smooth-body separation. Such inadequacies may be overcome by modifying the length scale in the wake and separated shear layers in order to keep RANS behavior in near wall regions and LES behavior in off-body regions. This effect is realized by using delayed, detached eddy simulation (DDES) [191]. DDES seeks to maintain RANS-like behavior in attached boundary layers through the use

of a shielding function to switch between RANS and LES length scales. This length scale switch is suggested by Coder and Ortiz-Melendez to be [81],

$$\tilde{d} = d - \gamma_{lim}\, f_d \max[0, d - C_{DES}\Delta] \tag{4.78}$$

which explicitly replaces the length scale d appearing in the Spalart-Allmaras model. The shielding function f_d is designed to be equal to 1 in LES-like regions,

$$f_d = 1 - \tanh[(8r_d)^3] \tag{4.79}$$

where r_d is the ratio of a characteristic turbulence model length scale to a wall-distance length scale,

$$r_d = \frac{\nu + \nu_t}{\sqrt{U_{ij}U_{ij}}\kappa^2 d^2} \tag{4.80}$$

and

$$\gamma_{lim} = \min[\exp(\tilde{\gamma}), 1] \tag{4.81}$$

This maintains that when intermittency is 0, the length scale is simply the base SA length scale. But when intermittency flips to 1, the length scale becomes a function of the grid cell size and r_d. Other parameters appearing in Eq. 4.78 are $C_{DES} = 0.65$ and Δ is equal to the length of the longest dimension of the grid cell in question.

Formally, the aforementioned variants of the AFT model are referred to as SA-neg-RC-DDES-AFT2019b or SA-neg-RC-DDES-AFT2019b+CF. For brevity, in this study, the variant of the AFT model without crossflow is referred to as "AFT2019b" and variant of the AFT model with crossflow is referred to as "AFT2019b+CF".

4.3 Geometries and Grid Generation

OVERFLOW solves the Navier-Stokes equations on grid systems using the overset grid topology. The user generates three-dimensional near-body grids, called near-body volume grids. Then, routines internal to OVERFLOW can automatically generate overset, three-dimensional, off-body grids about the near-body grids, if the user so specifies. It is important that the near-body grids are

large enough to have some overlap with off-body grids in order to facilitate interpolation on overset boundaries.

4.3.1 Isolated PSP Grid System in Hover

The Pressure Sensitive Paint (PSP) rotor tested at NASA Langley [6] was Mach-scaled for hover performance data and boundary layer transition data. The Mach-scaled blade planform has a nominal radius of 66.5" with a reference chord of 5.45" and has a swept, tapered tip. A diagram of the rotor blade and its geometric properties are given in Fig. 4.1 and Table 4.1, respectively.

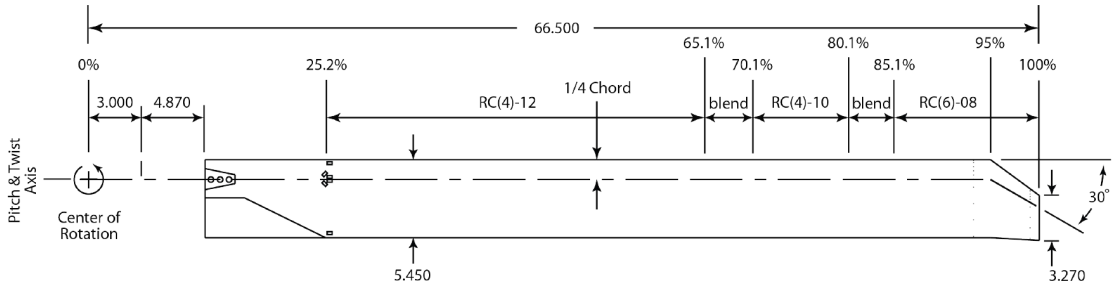


Fig. 4.1 PSP rotor blade planform [6]

Table 4.1 PSP rotor geometric properties [6]

Number of blades, N_b	4
Radius, R	66.5"
Reference chord, c	5.45"
Rotor solidity, σ	0.1043
Twist, linear	-14°
Tip taper	0.6
Tip sweep (c/4)	30°
Airfoils	RC(4)-10 RC(4)-12 RC(6)-08

Surface grids for the PSP rotor blade were provided by the AIAA Applied Aerodynamics Technical Committee Rotorcraft Simulation Discussion Group [192]. Each blade features three

separate, overset grids: a main planform grid, a root cap grid, and a tip cap grid. Cap grids improve spatial resolution in regions with difficult-to-resolve flow features, such as the vortex system at the root and vortices released at the blade tip. The main planform grid has 517 points in the chordwise direction with 251 points in the radial direction. Volume grids were generated using Chimera Grid Tools [193], a software suite capable of manipulating and generating surface grids and volume grids for overset capabilities. The volume grids were based on static sea-level conditions, with a tip Mach number of 0.58 and a Reynolds number of 384,000 per inch. Initial wall-spacing was determined using a y^+ of 0.67 based on flat plate boundary layer theory, corresponding to approximately 3.48 x 10^{-5} inches. This provides sufficient grid resolution in the boundary layer in order to properly capture the scales occurring in this region. The grid is then extruded 6" ($1.1c$) hyperbolically in the wall-normal direction using 73 points in order to achieve a suitable stretching ratio and sufficient overlap with the off-body grid system, as shown in Fig. 4.2. This procedure was repeated for the main planform grid and both cap grids such that each blade is comprised of three volume grids, aggregating to about 12.4 million points per blade. This set of volume grids was copied three more times to create all four blades, which were then phase-shifted by 90° relative to each other blade. The full, four-bladed rotor system contains then 49.5 million points.

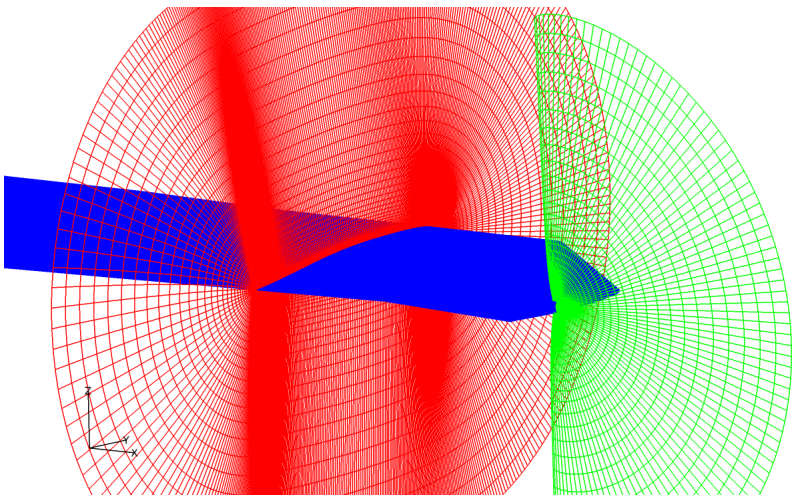


Fig. 4.2 PSP rotor blade near-body, structured, overset grid system

In order to capture flow features away from the near-body grid system, a nested, Cartesian, off-body grid system was automatically created using routines built in to OVERFLOW. Setting the dimensions and spacing of the nearest off-body grid along with the farfield distance fixes the size and number of off-body grids generated. The nearest off-body grid is specified to be a rectangle in the x-y plane extending in the z-direction with isotropic grid cells. The origin is set as the center of the rotor disk. The nearest off-body grid spacing is 0.5" (0.09c) in order to accurately capture the size and strength of blade tip vortices. The nearest grid extends from -1.13R to 1.13R in the x-direction and y-direction and from -0.72R to 0.18R in the z-direction with farfield distance set to 22.6R, as shown in Fig. 4.3. The full off-body system is comprised of 52 grids and 15.4 million points. Thus, the full grid system contains approximately 64.9 million points.

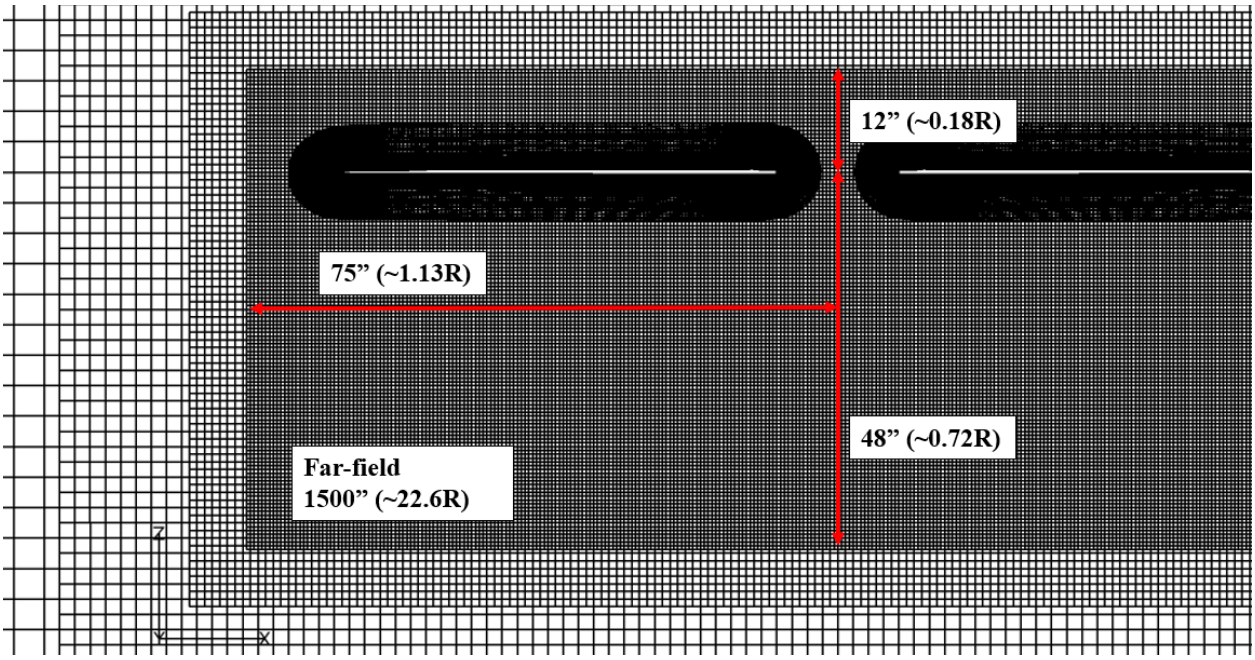


Fig. 4.3 PSP off-body, Cartesian, overset grid system

4.3.2 PSP-ROBIN Grid System in Forward Flight

A Mach-scaled, three-bladed PSP rotor was installed on the ROBIN mod7 fuselage and tested at NASA Langley in forward flight conditions [173]. To be consistent with experiments, the fuselage

was pitched down 3° and the blade grids were moved radially outward by 0.5” due to additional hinge offset in experiments. The PSP volume grids were designed in the same manner as for the isolated hover case. However, these grids were based off a hover tip Mach number of 0.57 and a Reynolds number of 373,000 per inch. Initial wall-spacing was based on a y^+ of 0.67, about 3.58 x 10^{-5} inches. Grids were extruded 6” in the wall-normal direction using 73 points. Each blade grid system contains then 12.4 million points, totaling 37.2 million points for the three-bladed rotor.

The ROBIN mod7 fuselage surface and volume grid was provided by Parwani and Coder [153]. The ROBIN grid system contains three grids: a main fuselage body grid, a nose cap grid, and a tail cap grid. The cap grids were designed to patch surface singularities during the surface grid generation process. These fuselage surface grids were extruded 9” using 65 points in the wall-normal direction, with initial wall spacing based on y^+ of 0.67, as shown in Fig. 4.4. The ROBIN near-body grid system contains approximately 8.9 million points.

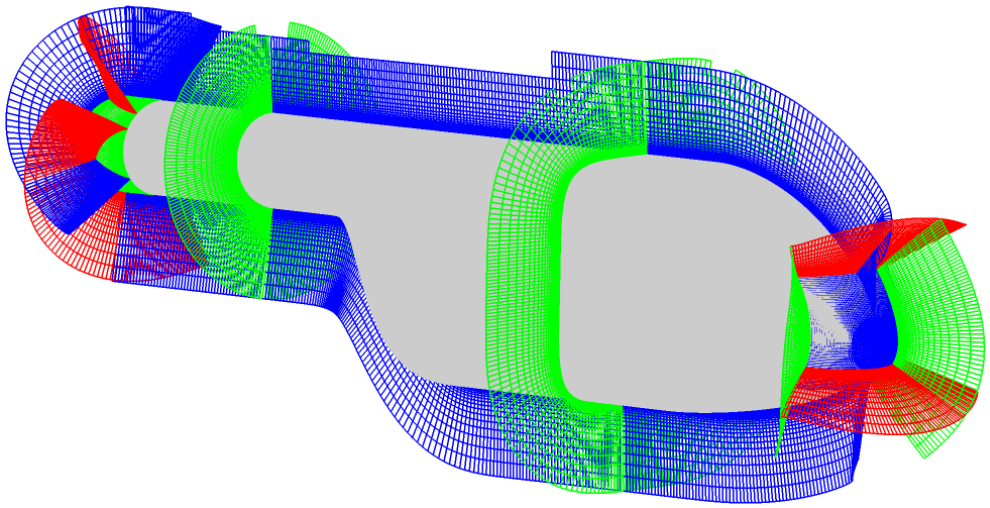


Fig. 4.4 ROBIN mod7 near-body, structured, overset grid system

The off-body grid system features additional refinement in the freestream direction in order to capture the wake structure, as shown in Fig. 4.5. Given that in forward flight the wake is convected downstream of the rotor disk, rather than below the rotor disk, little refinement is needed below the rotor disk, allowing a more-refined grid in the wake. The nearest off-body grid has a cell size of 0.4” in order to match the size of the outermost cell of the near-body grids. This aids in reducing

interpolation error at the overset boundary between the blade grids and off-body grids. The nearest grid extends from -1.12R to 1.79R in the freestream direction, -1.12R to 1.12R in the transverse direction, and -0.72R below the rotor disk and 0.18R above the rotor disk. The farfield distance is specified as 22.4R. The off-body grid system is comprised of 54 grids and 34.1 million grid points. The full near-body and off-body grid system contains 80.2 million points.

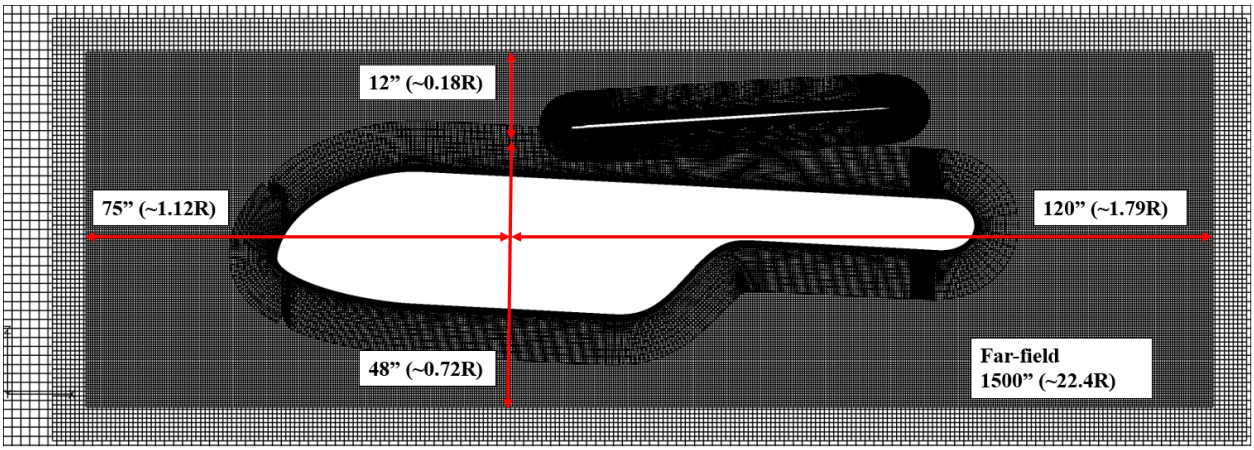


Fig. 4.5 PSP-ROBIN off-body, Cartesian, overset grid system

4.3.3 Isolated S-76 Grid System in Hover

The S-76 rotor designed by Sikorsky was tested at a model scale in hover [144]. The scaled blade has a radius of 56.04" with a reference chord of 3.1". Experimental studies examined several tip shapes, but in this study only the swept tapered tip is employed. The planform of the S-76 blade with the swept tapered tip is given in Fig. 4.6. Additionally, geometric properties are outlined in Table 4.2.

Surface grids for the S-76 rotor blade were provided by the AIAA Applied Aerodynamics Technical Committee Rotorcraft Simulation Discussion Group [192]. Each blade features three separate, overset grids: a main planform grid, a root cap grid, and a tip cap grid. The main planform grid features 377 points in the chordwise direction and 133 points in the radial direction. The provided grid system also features a notional teardrop hub [150]. This hub provides a blockage effect near the root, leading to improved convergence with respect to the root vortex system while

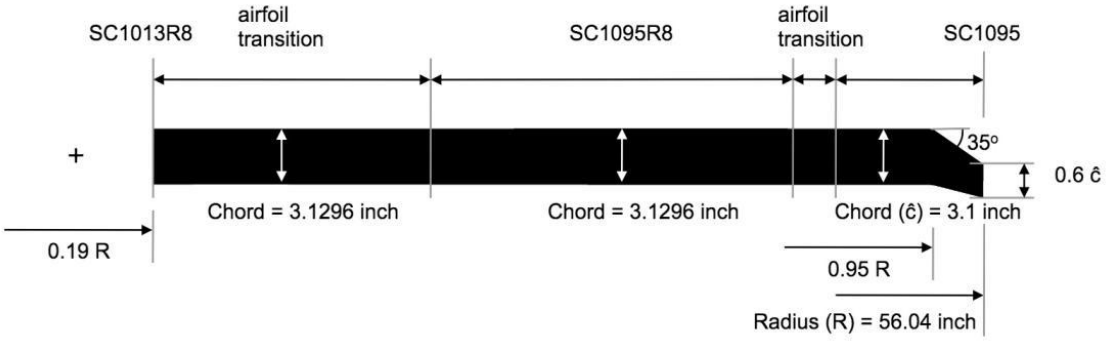


Fig. 4.6 S-76 rotor blade planform [194]

Table 4.2 S-76 rotor geometric properties [144]

Number of blades, N_b	4
Radius, *R*	56.04”
Reference chord, *c*	3.10”
Rotor solidity, σ	0.07043
Twist, linear	-10°
Tip taper	0.6
Tip sweep (leading edge)	35°
Airfoils	SC1013-R8 SC1095-R8 SC1095

minimally affecting predicted forces and moments [150]. The hub is an axisymmetric, tapered ellipsoid with 361 points on the axis of revolution and 71 points in the vertical direction, as shown in Fig. 4.7. Near-body volume grids for the blades and hubs were based on a tip Mach number of 0.65 and a Reynolds number of 390,000 per inch. Initial wall spacing was 3.20 x 10^{-5} inches based on a y^+ of 0.67 from flat plate boundary layer theory. The volume grids were extruded 3.5” (1.13c) in the wall-normal direction using 65 points, as shown in Fig. 4.8. Each blade grid system

contains about 4.2 million points while the hub contains about 1.6 million points. Thus, the full four-bladed rotor and hub system contains 18.4 million points.

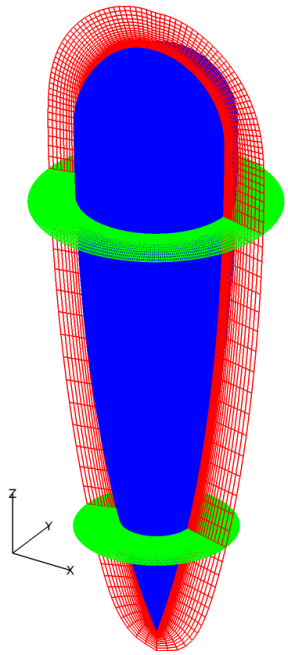


Fig. 4.7 S-76 hub near-body, structured, overset grid system

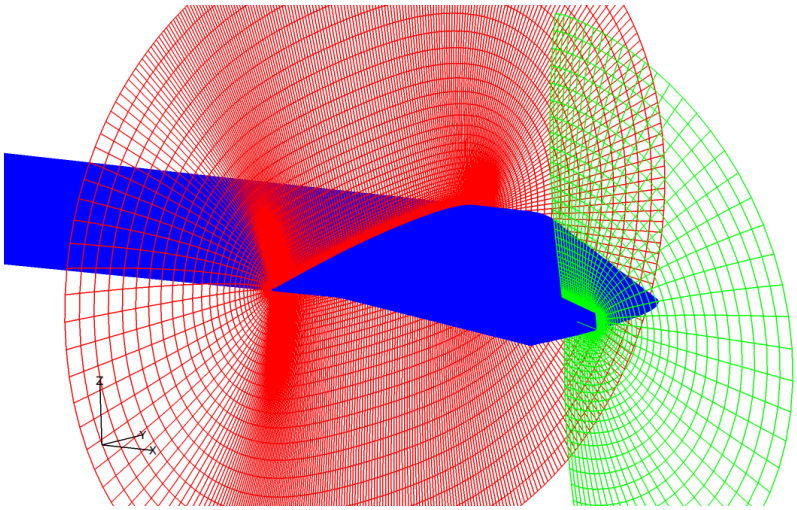


Fig. 4.8 S-76 rotor blade near-body, structured, overset grid system

The off-body grids were automatically generated using OVERFLOW. The spacing of the nearest off-body grid is 0.4", consistent with the cell size of the near-body grids at the overset boundary. This grid spans -1.07R to 1.07R in the x-direction and y-direction and from -0.86R to 0.21R in the z-direction. The farfield distance is set to 26.8R. The off-body system contains about 18.8 million points. Thus, the full grid system contains 37.2 million points, given in Fig. 4.9.

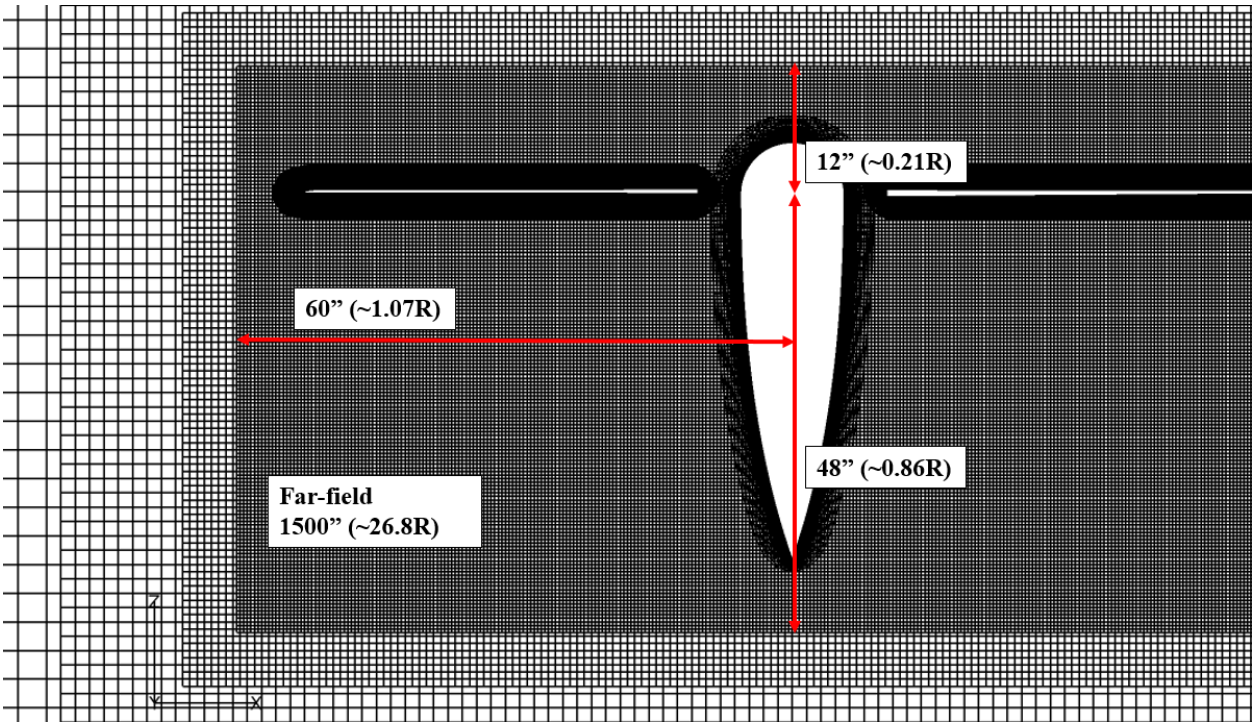


Fig. 4.9 S-76 off-body, Cartesian, overset grid system

4.3.4 NLF(2)-0415 Infinite Swept Wing

The NLF(2)-0415 airfoil tested by Dagenhart [176] and Radeztsky [177] serves as a test case for crossflow transition model validation that is pre-built into OVERFLOW. The grid system is designed as a two-dimensional airfoil grid, which is then copied four times and offset some distance in the spanwise direction. Three-dimensional relief effects at the wingtips are excluded by using a periodic flow boundary condition applied to the first and last spanwise plane, rendering the airfoil

grid system as “infinite”. The airfoil itself features 513 points in the chordwise direction, 5 points in the spanwise direction, and 97 points in the wall-normal direction, shown in Fig. 4.10.

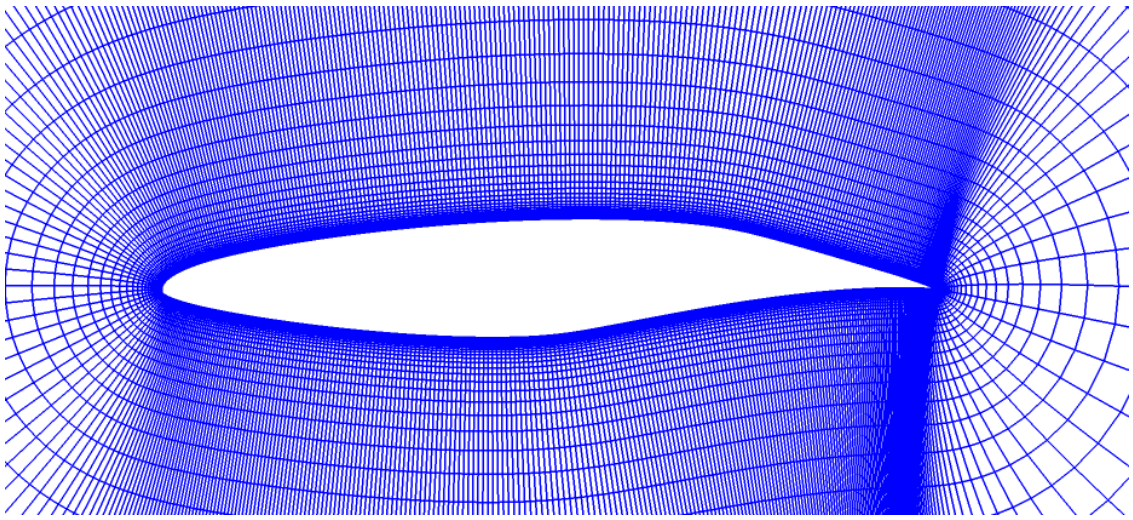


Fig. 4.10 NLF(2)-415 infinite swept wing structured grid

4.3.5 6:1 Inclined Prolate Spheroid

Grids for the 6:1 inclined prolate spheroid were provided by the AIAA CFD Transition Modeling Discussion Group. Only the right side of the prolate spheroid is modeled in the current grid system as experiments have shown the transition line is symmetric along the central axis. Thus, a symmetry plane boundary condition is applied in the axial and radial direction. The grid features 257 points in the axial direction, 129 points in the radial direction, and 129 points in the wall-normal direction as shown in Fig. 4.11.

4.3.6 TU Braunschweig Sickle Wing

The sickle wing tested at TU Braunschweig by Petzold and Radespiel [181] serves as a test case for crossflow model validation that is pre-built into OVERFLOW. The grid system is comprised of two near-body grids: a main planform grid and a tip cap grid, shown in Fig. 4.12. In order to model the tunnel wall, a symmetry plane with no reflection boundary condition is specified at the

root of the wing. The main planform features 497 points in the chordwise direction, 233 points in the spanwise direction, and 59 points in the wall-normal direction. It is of note that the grid system features a C-grid type wake cut which is comprised of 61 points. Thus, the grid features 557 points in the chordwise direction where 497 of those points are on the surface. Wall-normal spacing is based on a y^+ of 0.33, about 2.5 x 10^{-6} inches in order to sufficiently resolve the lower regions of the boundary layer. The tip cap grid features 279 points from the leading edge to the trailing edge with dense clustering near the leading edge, 73 points wrapping from the upper surface to the lower surface, and 59 points in the wall-normal direction. The near-body grids total approximately 8.9 million points. The Cartesian off-body grid system was automatically generated with 0.05" spacing for the nearest off-body grid. The farfield distance was set to 50" (50c). The full off-body, Cartesian grid system contains 43 grids and approximately 0.3 million points.

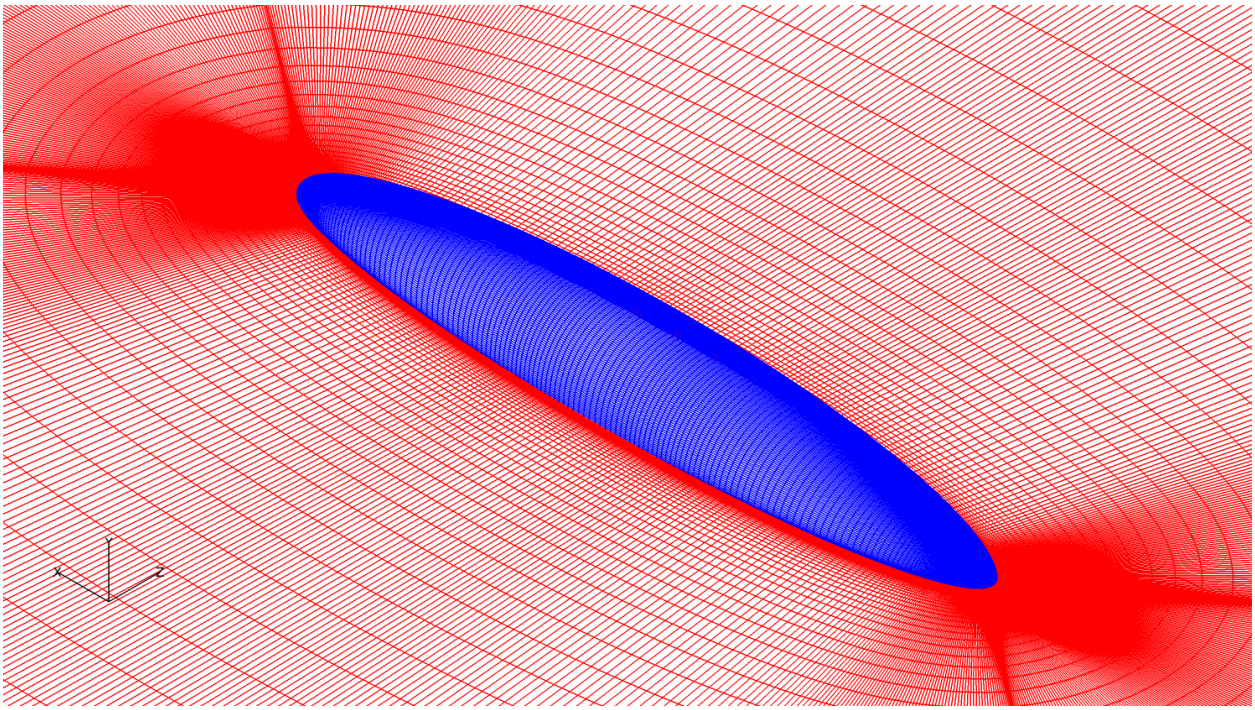


Fig. 4.11 6:1 inclined prolate spheroid structured grid

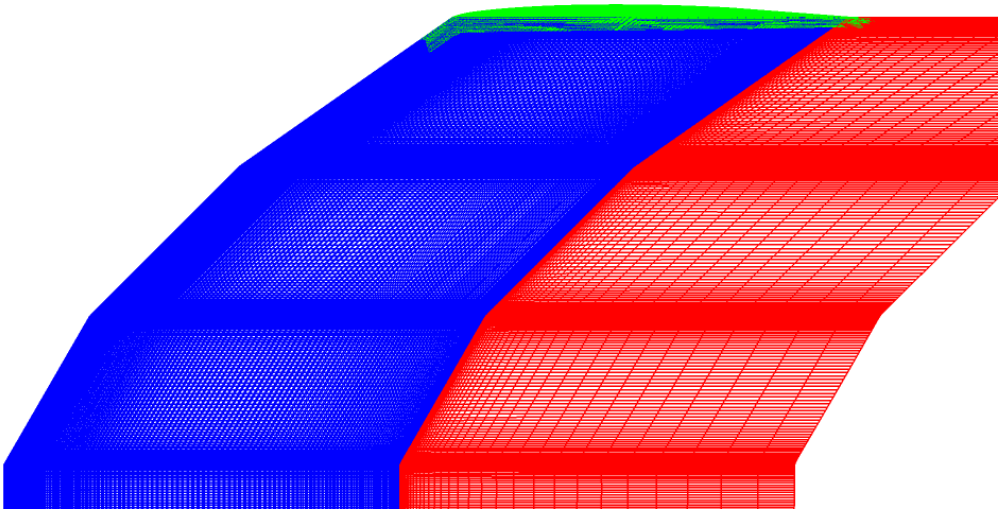


Fig. 4.12 TU Braunschweig sickle wing near-body, structured, overset grid system

4.4 Boundary Conditions

For each grid, overset connectivity was computed using XRAYS [195], an overset hole-cutting routine internal to Chimera Grid Tools [193]. In order to facilitate the higher-order upwinding required for the WENO stencil, three fringe layers were specified. Viscous stencil repair was employed in the wall-normal direction for the first 24 points for the S-76 blade and the first 32 points for the PSP blade and ROBIN fuselage. This allows interpolation between overlapping grids that lie on the same surface, such as a root cap grid on a main planform grid. To account for solid surfaces, a viscous, no-slip boundary condition with pressure extrapolation was employed. Force and moment coefficients were computed using USURP [196]. USURP is capable of calculating integrated force and moment coefficients, along with mass flow rates, over viscous, overlapped surface grids. For the S-76 and PSP rotors in hover, given the rotationally symmetric nature of a rotor in hover, each blade should produce the same force and moment coefficients. Thus, performance data are computed for only a single blade. However, for the PSP-ROBIN system in forward flight, force and moment coefficients are computed for each blade and summed together.

4.5 Post-processing

Force, moment, and residual post-processing was performed using Chimera Grid Tools [193] for data extraction and Tecplot [197] for data manipulation and plotting. Wake structures and transition locations were computed graphically using FieldView 18 [198]. Transition locations were then digitized and plotted using Tecplot.

4.5.1 Proper Orthogonal Decomposition

Proper orthogonal decomposition (POD) is used in this work to investigate unsteady behavior in predicted boundary layer transition. POD is a modal decomposition technique that seeks to reconstruct a data set by summing the mean of the data set with higher-order perturbations, or modes [199]. POD seeks to extract modes by optimizing the mean square of the data set of interest. When applied to fluid flows, this can reveal baseline structures evident in turbulent flows [200], dominant flow features over an airfoil [201], and unsteady behavior in cavity flows [202] among others. Given some vector field of interest q, the steady and unsteady components can be separated as

$$q(\xi,t) - \overline{q}(\xi) = \sum_j a_j(\xi,t)\,\phi_j(\xi,t) \tag{4.82}$$

The left hand side is the vector field with the mean values subtracted, isolating the unsteady behavior. The right hand side then is the unsteady behavior that can be quantified as a sum of the product of the expansion coefficients a_j and modes ϕ_j. More generally, the right hand side is a Fourier series on the orthogonal basis ϕ_j. This basis is the optimized basis on which the vector field q can be represented [199]. The expansion coefficients are found with the inner product of the perturbations of the vector field and the modes.

$$a_j = \langle\, q(\xi,t) - \overline{q}(\xi)\,,\, \phi_j(\xi)\,\rangle \tag{4.83}$$

In this work, POD is used to analyze the unsteady behavior of boundary layer transition on the PSP rotor in hover. The unsteady transition phenomenon is both a function of space and time. Fortunately, by discretizing the time domain into "snapshots", the modes, collapse down

to a function of space only. Thus, Eq. 4.82 simplifies to

$$q(\xi, t) - \overline{q}(\xi) = \sum_{j} a_j(t)\, \phi_j(\xi) \tag{4.84}$$

where the modes can be computed via singular value decomposition (SVD),

$$X = U\, \Sigma\, V \tag{4.85}$$

and X is the data set of interest, U contains the eigenvectors of XX^T, Σ represents the eigenvalues of the data set, and V contains the modes. The modes are automatically ordered from the largest corresponding eigenvalue to the lowest corresponding eigenvalue. This can be thought of as a modal energy, in which the first mode contains the largest share of energy in the system compared to each other mode individually. Examining the first mode gives a quasi-average reconstruction of the data set, in that this mode is the best representation of the data set using only one mode. In this work, where the data set is a vector of snapshots of transition locations in space, the unsteady transition behavior over time becomes apparent in a pseudo-statistical manner when examining the first few modes. Specifically, examining the first few modes may not show a sharp average transition line, but will show regions where transition is more likely to occur throughout the full data set. This is in essence a reduced-order model that can be examined in a low-cost, low-storage manner, providing insight on the unsteady transition behavior.

Chapter 5: Results

5.1 Crossflow Model Validation

The implementation of AFT2019b+CF into OVERFLOW has been validated for a suite of two-dimensional and three-dimensional test cases suggested by Langtry et al. [12] and Coder [174]. Predicted transition locations are compared to experiments for the crossflow validation test cases outlined in Chapter 3.

5.1.1 NLF(2)-0415 Infinite Swept Wing

The NLF(2)-0415 infinite swept wing was simulated at a constant angle of attack of -4° with a sweep angle of 45°. A Reynolds number sweep was performed to match that of experiments. Simulations were performed until residual and force and moment coefficient convergence were satisfied, approximately 5000 iterations.

Given in Fig. 5.1 are predicted transition locations using the AFT2019b model and the AFT2019b+CF model in comparison to experimental results. Transition predicted using AFT2019b is seemingly irrespective of the Reynolds number, with transition occurring near the pressure minimum at $x/c = 0.71$. With the addition of crossflow transition modeling, the predicted transition location correlates much better with experiments. As Reynolds number increases, the transition location moves forward as the stationary crossflow instability begin to dominate over Tollmien-Schlichting instabilities and thus dominates transition. In comparison to the experimentally reported transition locations, AFT2019b+CF predicts transition slightly more downstream; however, predicted transition still lies between the reported error bars.

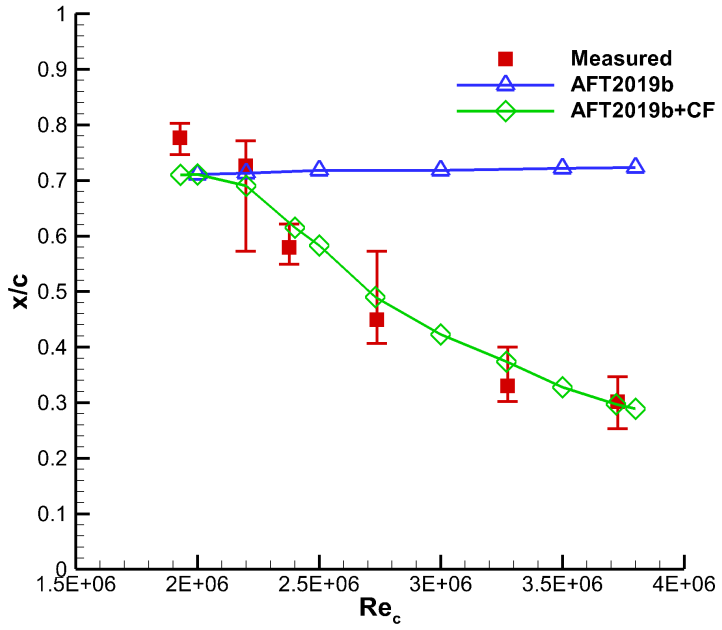
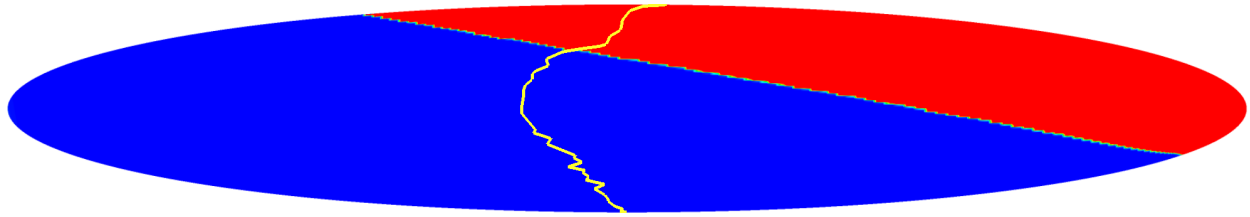


Fig. 5.1 Predicted transition locations on the upper surface of the NLF(2)-0415 wing

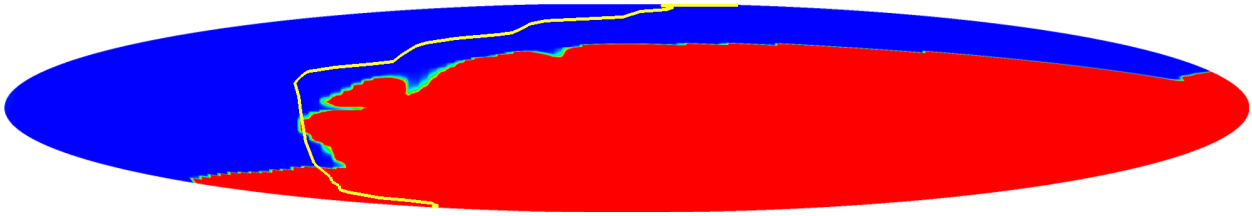
5.1.2 6:1 Inclined Prolate Spheroid

The 6:1 inclined prolate spheroid was simulated at a constant Reynolds number and Mach number for three different angles of attack. Given in Fig. 5.2 are predicted transition locations with overlaid experimentally reported transition locations. When considering pressure gradient as the primary mechanism of transition (i.e. Tollmien-Schlichting type transition), the suction surface (upper half of the spheroid in Fig. 5.2) should exhibit earlier transition than the pressure surface (lower half of the spheroid in Fig. 5.2). The transition line should vary linearly from the lower surface to the upper surface as a function of radial and azimuthal position. This is the case for 5° angle of attack in Fig. 5.2a. AFT2019b+CF predicts transition to vary linearly (in the Cartesian projection of Fig. 5.2) in the transverse direction. Thus, it follows that at 5° angle of attack AFT2019b+CF predicts transition likely as a function of Tollmien-Schlichting instabilities rather than crossflow instabilities. As crossflow strength grows, crossflow waves destabilize in favorable

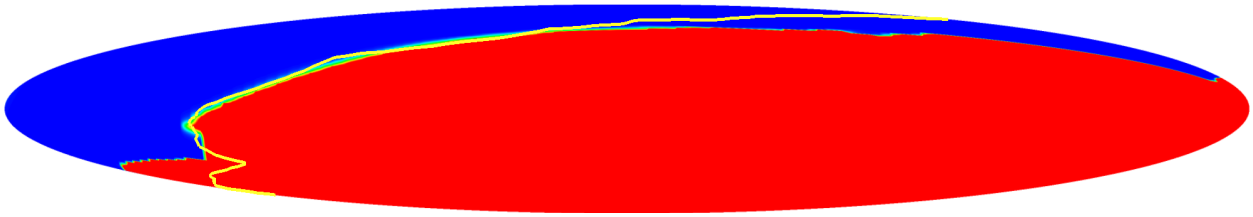
pressure gradients, such as those on the lower surface, and stabilize in adverse gradients, such as those on the suction surface. AFT2019b+CF correctly predicts this relationship at higher angles of attack as streamwise leading edge vortices grow in strength. At 10° angle of attack, AFT2019b+CF predicts a slightly more "jagged" transition line compared to experiments and shows small regions of re-laminarization. At 15° angle of attack, AFT2019b+CF shows excellent agreement with experiments; however, transition is predicted to be slightly early on the pressure surface compared to experiments. Nevertheless, the overall trendline in transition on the surface is well-captured. These results suggest that AFT2019b+CF is capable of capturing transition due to strong crossflow, but may be less receptive to transition effects due to weak crossflow.



(a) $\alpha = 5°$



(b) $\alpha = 10°$



(c) $\alpha = 15°$

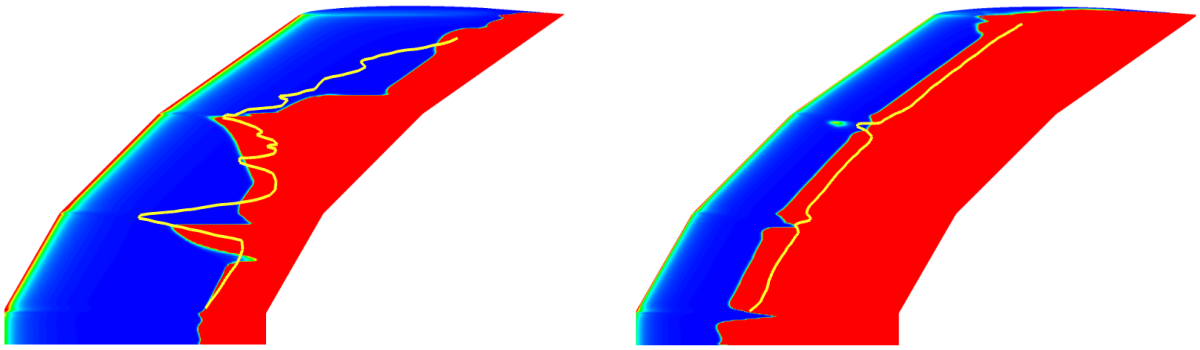
Fig. 5.2 Predicted transition locations using AFT2019b+CF on the 6:1 inclined prolate spheroid at $Re = 6.5$ x 10^6, $M_\infty = 0.13$ visualized via Spalart's turbulence index (blue - laminar, red - turbulent), yellow - measured transition locations

5.1.3 TU Braunschweig Sickle Wing

Four test conditions for the TU Braunschweig sickle wing were simulated as specified by Petzold and Radespiel [181] and Coder [174], outlined in Table 5.1. Given in Fig. 5.3-5.6 are predicted transition locations using AFT2019b+CF with overlaid experimental transition locations. In general, AFT2019b+CF captures well transition locations as a function of chord and span. Experimental transition locations exhibit a "sawtooth" pattern in the transition line for each section that is not captured in simulations. Denison and Pulliam [203] suggest that this lack of waviness in the numerical solution is an artifact of the structured, overset gridding approach. AFT2019b+CF does properly capture the effects of the sweep breaks on transition. At each sweep break, a streamwise vortex is released which amplifies the crossflow strength locally and forces earlier transition. The transition line on the most outboard section is not as well captured on the upper surface for Case A,B, and C and similarly for the lower surface for Case D. In particular, the transition location is predicted to be farther aft than in experiments. Similarly, transition on the lower surface of Case A,B, and C and the upper surface for Case D is predicted to occur more forward than in experiments. However, it remains that AFT2019b+CF performed well in capturing transition effects due to crossflow on this difficult geometry.

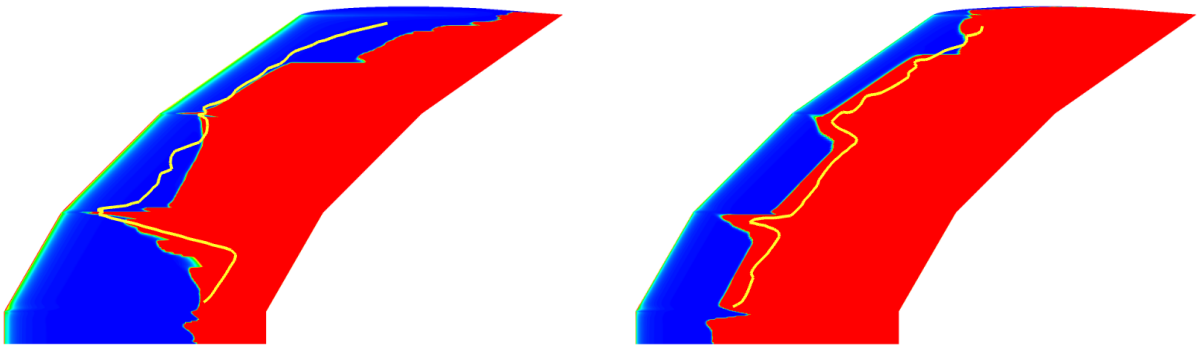
Table 5.1 TU Braunschweig sickle wing test parameters

Case	**A**	**B**	**C**	**D**
Mach number	0.156	0.259	0.259	0.158
Angle of attack, α	-2.6°	-2.6°	-0.3°	6.0°
Reynolds number, Re_c	2.75 x 10^6	4.45 x 10^6	4.43 x 10^6	2.75 x 10^6



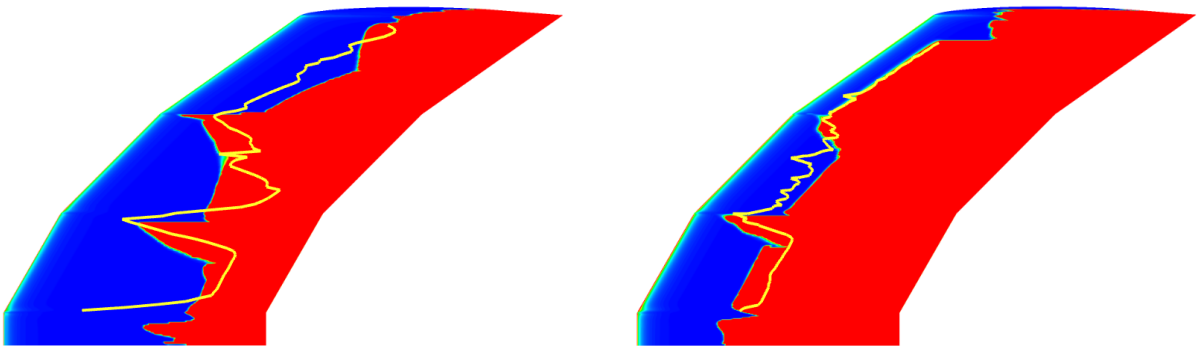
(a) Upper surface **(b)** Lower surface

Fig. 5.3 Predicted transition locations for Case A using AFT2019b+CF on the TU Braunschweig sickle wing visualized via Spalart's turbulence index (blue - laminar, red - turbulent), yellow - measured transition locations



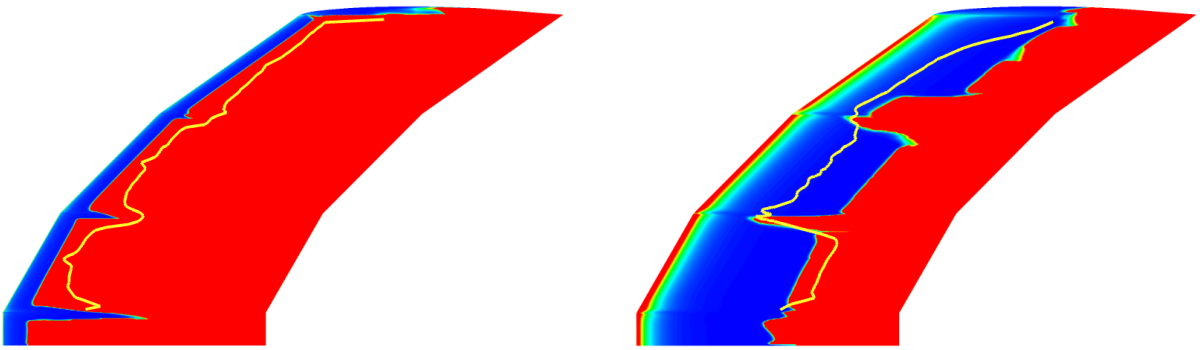
(a) Upper surface **(b)** Lower surface

Fig. 5.4 Predicted transition locations for Case B using AFT2019b+CF on the TU Braunschweig sickle wing visualized via Spalart's turbulence index (blue - laminar, red - turbulent), yellow - measured transition locations



(a) Upper surface **(b)** Lower surface

Fig. 5.5 Predicted transition locations for Case C using AFT2019b+CF on the TU Braunschweig sickle wing visualized via Spalart's turbulence index (blue - laminar, red - turbulent), yellow - measured transition locations



(a) Upper surface **(b)** Lower surface

Fig. 5.6 Predicted transition locations for Case D using AFT2019b+CF on the TU Braunschweig sickle wing visualized via Spalart's turbulence index (blue - laminar, red - turbulent), yellow - measured transition locations

5.2 Isolated S-76 Rotor in Hover

OVERFLOW 2.2n was used to make performance predictions on an isolated, four-bladed S-76 rotor with the swept tapered tip in hovering flight at a tip Mach number of 0.65. Simulations were performed using three turbulence closure methods: the fully turbulent SA-neg-RC-DDES model, the transitional AFT2019b model, and the transitional AFT2019b+CF model which includes crossflow transition. Two collective pitch cases were simulated, 6° and 10°, in order to predict transition and performance for a moderate thrust level and a high thrust level.

The rotors were cold-started at a hover tip Mach number of 0.65 (i.e. instantaneously accelerated). The initial flowfield must be set-up and the initial startup vortex must be advected out of the domain. In order to accelerate the simulation during startup, a dual-time stepping approach was used for the first 10 rotor revolutions. During this dual-time startup, the physical timestep corresponded to 1° of rotor rotation. A minimum CFL number of 1 was specified with a maximum CFL number of 10 in order to balance both convergence and stability. A local dual-time timestep equal to 0.5 was used, paired with 20 dual-time subiterations to ensure temporal convergence. After these 10 startup revolutions, the solution paradigm was switched to a global timestepping approach. The physical timestep was reduced to 0.25° of rotor rotation with 20 Newton subiterations. Solutions were carried out until force, moment, and residual convergence were satisfied. This criterion was satisfied at six full revolutions in physical time.

A representative thrust and torque history using AFT2019b is given in Fig. 5.7. Note that at revolution 10, there is a discontinuous jump for both thrust and torque. This is due to the the switch from dual-time timestepping to global timestepping. The first two revolutions in physical time exhibit transient spikes in thrust and torque. However, after revolution 14, the magnitude of these transients has decreased sufficiently such that the solution is considered converged. Sample residual convergence for the hub grid, main planform grid, root cap grid, and tip cap grid are given in Fig. 5.8. The time-stepping change at revolution 10 is again apparent. The hub grid achieves a steady residual value over time, but the residual is relatively high. The root cap grid and the tip cap grid show good periodic convergence. The main planform grid was notably difficult to converge, which may be a function of the coarse grid spacing around the midspan of the blade.

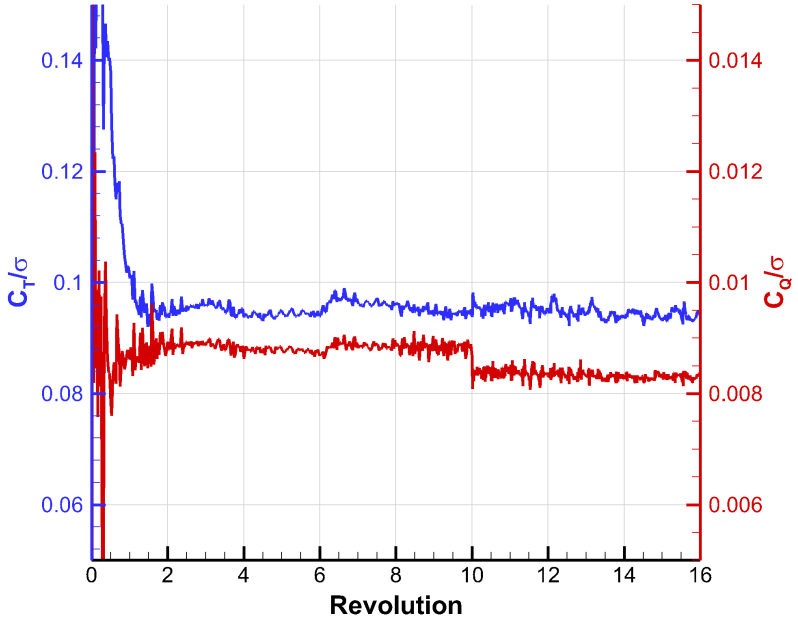


Fig. 5.7 Thrust and torque history for the S-76 rotor using AFT2019b, $\theta_0 = 10°$

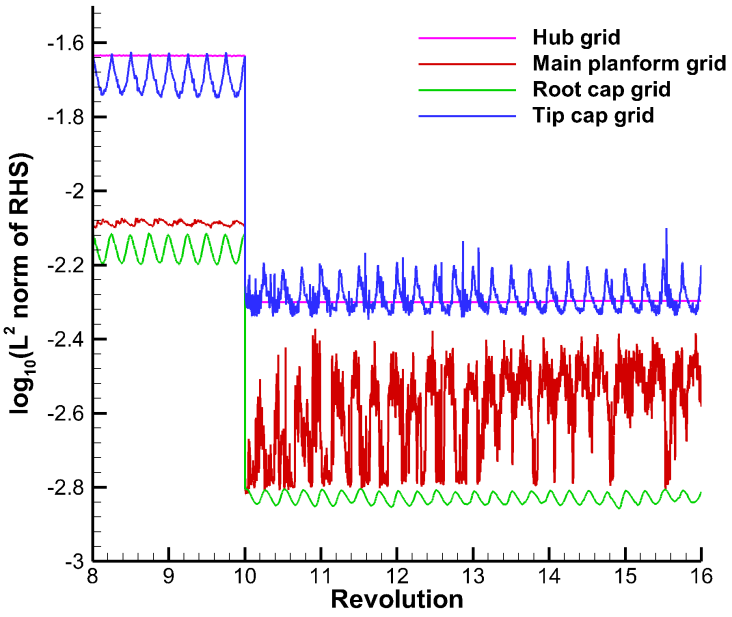


Fig. 5.8 Residual history for the S-76 rotor using AFT2019b, $\theta_0 = 10°$

Given in Table 5.2 are predicted rotor performance data for each collective pitch, for each turbulence model. Integrated forces and moments were computed every ten timesteps, or 2.5°. Thrust and torque coefficients were averaged over the final three revolutions of each simulation. It is of note that the fully turbulent SA-neg-RC model predicts higher thrust over both transition models. The addition of laminar flow on the blade surface via the transition models seems to result in a lower thrust level. Predicted thrust is compared to experimental thrust as a function of collective pitch angle in Fig. 5.9. Each model slightly underpredicts the thrust level from experiments. In experiments, 6° and 10° collective pitch were not tested, rather, 6.1° and 10.3° collective pitch were tested, which may be a minor source of error. Computing thrust as a function of pitch is effectively the determination of the lift curve which is dominated by inviscid phenomena and should be relatively easy to compute. More difficult is the prediction of torque level, which involves both viscous and inviscid phenomena.

Accurate prediction of rotor torque is heavily dependent on the capturing of trailed tip-vortices, which then affects and defines the rotor wake structure. The transition models predict a significantly lower torque level, approximately 10% lower than that predicted using SA-neg-RC. Turbulent boundary layers feature higher skin friction, which leads to an increase in drag. For a rotor, drag acts tangentially about the center of the rotor and induces a torque that must be overcome by the engine. With laminar flow accounted for in the transition models, the drag is less than for the fully turbulent model and the rotor torque is therefore less as well. Comparisons of predicted torque are plotted with experimental data in Fig. 5.10. At moderate collective pitch, the transition models underpredicted the experimental torque value, while the fully turbulent model predicts a higher torque that correlates better with experiments. All models overpredict the rotor torque at high collective pitch, but especially so for the fully turbulent model. The crossflow model predicts slightly higher torque than the model without crossflow, which may indicate that accounting for crossflow effects has resulted in a more turbulent blade surface.

The differences in predicted torque are especially exacerbated when examining the FM as a function of thrust level, as shown in Fig. 5.11. At moderate thrust, SA-neg-RC underpredicts FM by about two counts (i.e. 0.02). Whereas both transition models predict approximately the same FM but grossly overpredict FM compared to experiments. This highlights the potential of laminar flow to vastly increase the rotor FM due to the decrease in drag incumbent with laminar boundary

layers. At higher thrust, the fully turbulent model and the model without crossflow predict about the same FM although the fully turbulent model predicts higher thrust. When accounting for crossflow in AFT2019b+CF, the FM is higher by one count compared to the other models, but underpredicts FM by nearly three counts relative to experiments. The differences in predicted FM in comparison to experiments may be a function of coarse blade surface grids and also a function of the lower-than-desirable residual convergence.

Table 5.2 S-76 rotor predicted performance in hover

Collective, θ_o		SA-neg-RC	AFT2019b	AFT2019b+CF
6°	C_T/σ	0.05032	0.04928	0.04941
	C_Q/σ	0.003691	0.003216	0.003237
	FM	0.5739	0.6384	0.6368
10°	C_T/σ	0.09705	0.09422	0.09578
	C_Q/σ	0.008714	0.008304	0.008385
	FM	0.6511	0.6535	0.6634

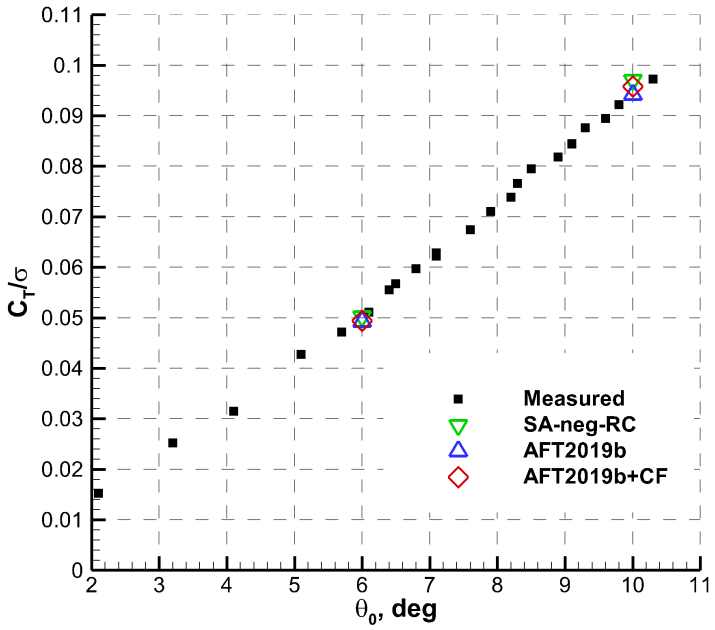


Fig. 5.9 Comparison of thrust as a function of collective pitch for the S-76 rotor

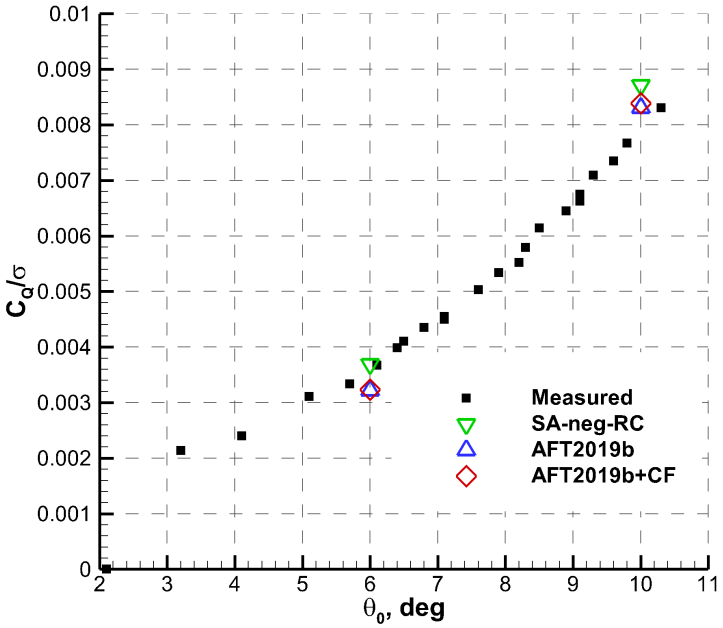


Fig. 5.10 Comparison of torque as a function of collective pitch for the S-76 rotor

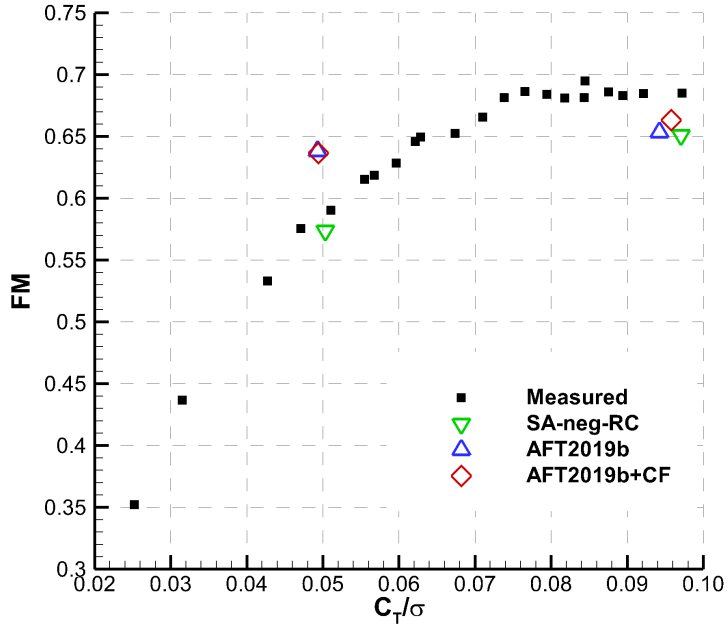


Fig. 5.11 Comparison of figure of merit as a function of thrust level for the S-76 rotor

Predicted transition locations were visualized using Spalart's turbulence index [94], which is a logical where a value of 0 indicates laminar flow and a value of 1 indicates turbulent flow.

$$i_t = \frac{\partial \tilde{\nu}/\partial n}{\kappa\sqrt{\nu|\Omega|}} \tag{5.1}$$

Contours of Spalart's turbulence index for AFT2019b and AFT2019b+CF for both collective pitches are given in Fig. 5.12-5.15. Note that these transition locations are instantaneous locations at revolution 13 (3 revolutions in physical time). It was found that predicted transition location did not appreciably change between revolution 13 and 16. These transition locations were then digitized and plotted as a function of blade radius, as shown in Fig. 5.16. Transition data were not reported in experiments, and thus predicted transition locations are restricted to comparison between transition models. When examining the 6° pitch case in Fig. 5.16a, the primary differences between models in transition location are inboard of $r/R = 0.40$ and outboard of $r/R = 0.90$. In the inboard region, low Reynolds number effects and unsteady interactions with the root vortex system drive erratic transition behavior. Up to about $r/R = 0.90$, transition locations are nearly identical for both models, insinuating that crossflow modeling has minimal effect in this region. In theory, this midspan region experiences, at most, weak crossflow as there are no streamwise vortices or sweep breaks, and spanwise pressure gradient is small. Transition here is expected to be dominated by Tollmien-Schlichting instabilities where the streamwise pressure gradient drives boundary layer instabilities rather than stationary crossflow waves. In the outboard region, AFT2019b+CF predicts slightly earlier transition at the sweep break at $r/R = 0.95$ on the upper surface, suggesting that the released streamwise vortex plays a role in transition. Given that helicity tracks well the strength of streamwise vortices and serves as a production term in the crossflow model, streamwise vortices should amplify the crossflow instability and induce transition. At $r/R > 0.99$ on the lower surface, the transition line is driven forward due to the vortex roll up at the tip. This effect is not evident on the upper surface. When examining the 10° pitch case in Fig. 5.16b, the effects of crossflow modeling are more evident. A BVI event occurs on the lower surface with a vortex core near $r/R = 0.9$ which drives transition forward when modeling crossflow. The production term of the crossflow model picks up the local helicity of the streamwise vortex and computes the stationary crossflow waves as sufficiently strong to induce transition. While

a similar effect is seen on the lower surface for AFT2019b, this patch of turbulent flow is more likely a function of the BVI event imparting momentum to the boundary layer and destabilizing it via enforcing a more adverse pressure gradient. The blade tip is nearly fully turbulent for the crossflow model for the same reason as for the 6° case. The upper surface is predicted nearly fully turbulent for both models. Again, the upper surface is dominated by Tollmien-Schlichting type transition and the effects of crossflow modeling are minimal.



(a) Upper surface



(b) Lower surface

Fig. 5.12 Instantaneous predicted transition locations using AFT2019b on the S-76 rotor, $\theta_0 = 6°$ (blue - laminar, red - turbulent)



(a) Upper surface



(b) Lower surface

Fig. 5.13 Instantaneous predicted transition locations using AFT2019b+CF on the S-76 rotor, $\theta_0 = 6°$ (blue - laminar, red - turbulent)



(a) Upper surface



(b) Lower surface

Fig. 5.14 Instantaneous predicted transition locations using AFT2019b on the S-76 rotor, $\theta_0 = 10°$ (blue - laminar, red - turbulent)

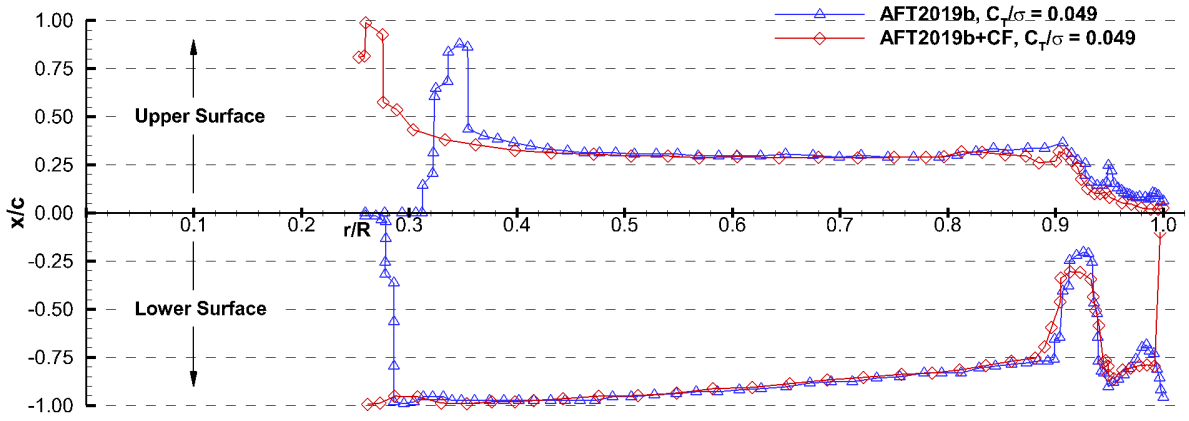


(a) Upper surface

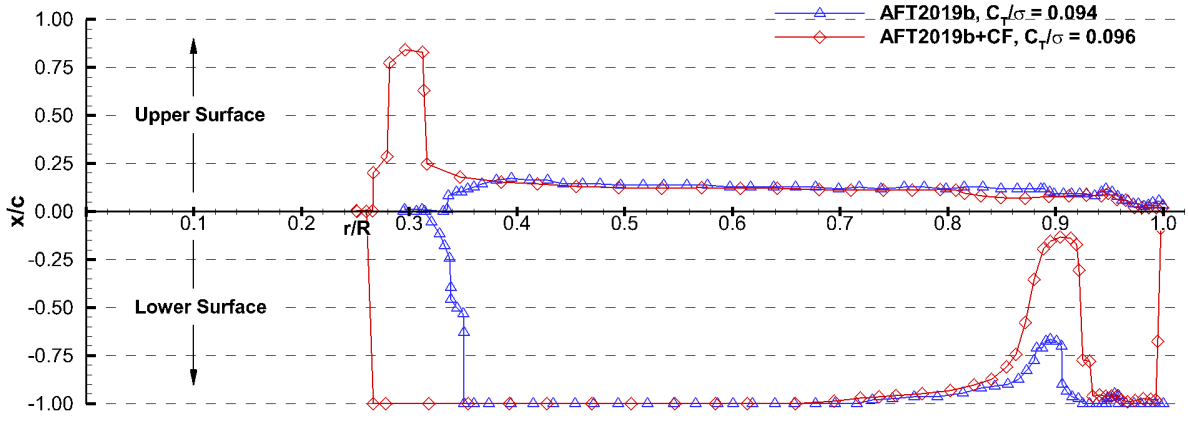


(b) Lower surface

Fig. 5.15 Instantaneous predicted transition locations using AFT2019b+CF on the S-76 rotor, $\theta_0 = 10°$ (blue - laminar, red - turbulent)



(a) $\theta_0 = 6°$



(b) $\theta_0 = 10°$

Fig. 5.16 Digitized instantaneous transition locations on the S-76 rotor

By visualizing contours of vorticity magnitude for each turbulence closure method, the wake structure can be examined qualitatively, as shown in Fig. 5.17 - 5.19 for the 10° collective pitch case. Each contour of vorticity magnitude was taken instantaneously at the final timestep, that is at the end of the sixth revolution in physical time. Contours produced from the fully turbulent simulations show more turbulent content in the wake than do the transitional simulations. The wake structure using the fully turbulent model shows increased vertical spacing between shear layers compared to the transition model, a direct result of the higher predicted thrust (i.e. higher induced velocity). This higher thrust level is also evident in the more-contracted wake of the fully turbulent simulations. It is of note that the shear layers for the fully turbulent results show stronger vorticity compared to the transitional results. Shear layer strength is proportional to the bound circulation, further showing that the fully turbulent simulation has a higher thrust level. AFT2019b+CF shows better tip vortex coherence for young-age wakes, suggesting the tip vortices have stronger circulation, which is evident in the predicted torque level. AFT2019b shows more vortical content near the hub than do the other models; however, this is more so an effect of transient behavior with the root vortex system rather than differences in modeling techniques. For the fully turbulent case, wake breakdown begins at 180° wake age. Both transitional simulations show a vortex pair forming at 90° wake age that serves to destabilize the wake structure and enforce wake breakdown. For all simulations, the shear layer begins to "roll into" the tip vortices at about 270° wake age, with significant wake breakdown by 360° wake age.

The wake can be additionally examined by visualizing isosurfaces of the Q-criterion of the velocity vectors, as shown in Fig. 5.20 - 5.22 colored by vorticity magnitude. The Q-criterion examines the second invariant of the velocity gradient tensor and defines a vortex as a region where the local vorticity magnitude Ω exceeds the local strain rate S [204]. In each simulation, vortex "braids" appear to curl around the 90° wake age vortex. These braids are a second-order instability and contribute to the breakdown of the wake structure. Such braids commonly occur in eddy-resolving CFD methods and have been reported by numerous other investigators [150–153, 194, 205]. The fully turbulent results show earlier wake breakdown, consistent with what was seen in contours of vorticity magnitude. The tip vortices show an undulation in their structure, which is especially seen near 180° wake age. This is likely an indication of the vortex beginning to unravel, but may also be a function of overset interpolation in the off-body grids.

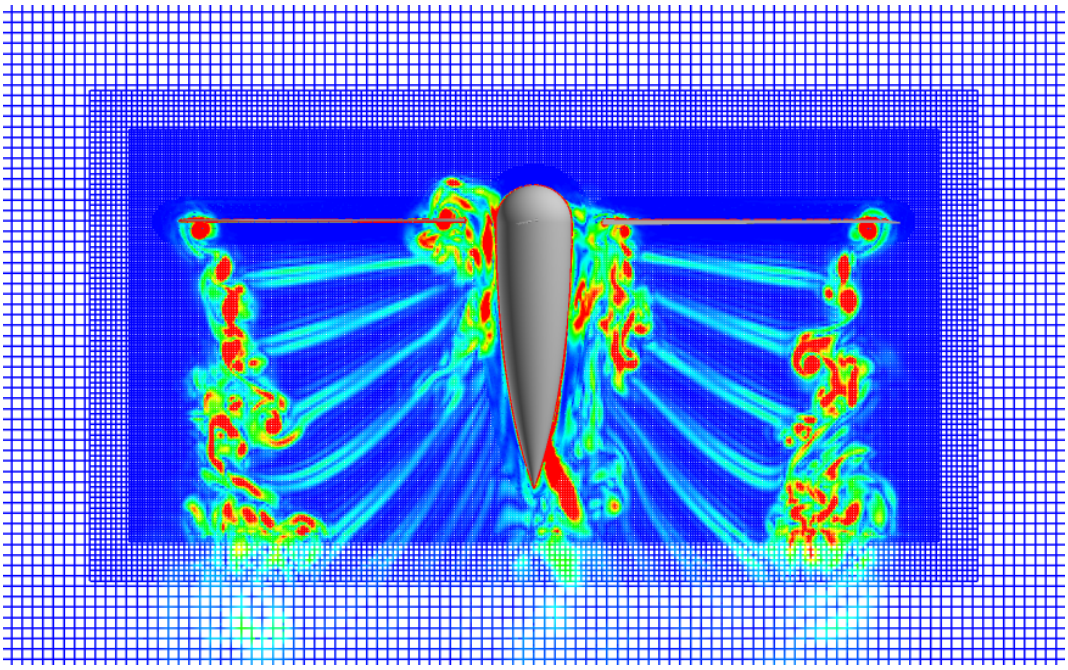


Fig. 5.17 Contours of vorticity magnitude on the y = 0 plane using SA-neg-RC on the S-76 rotor, $\theta_0 = 10°$

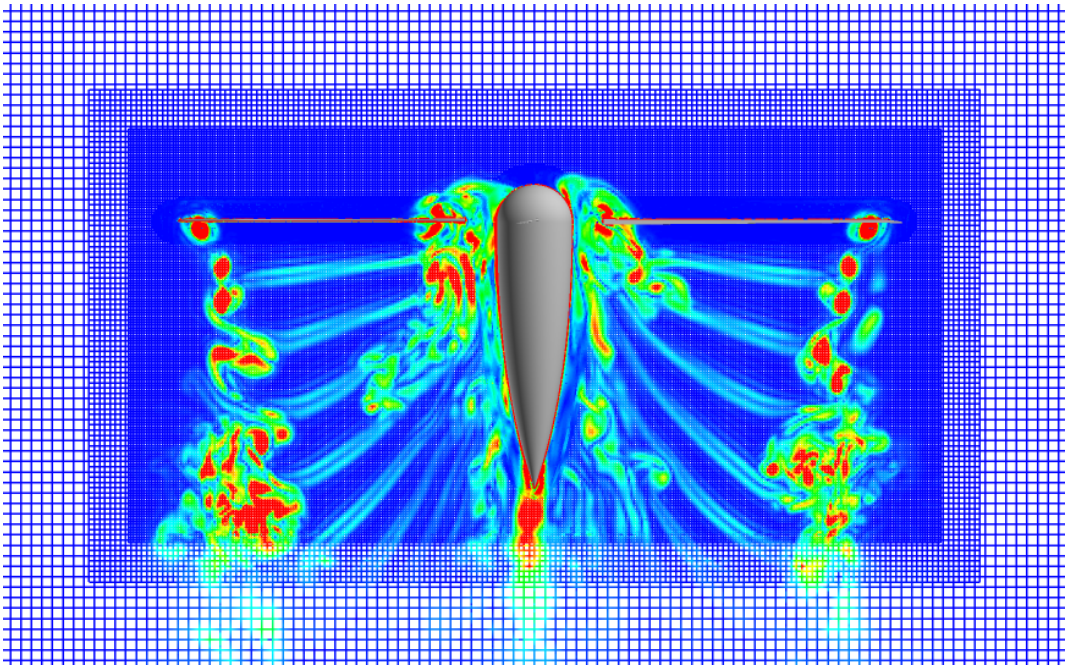


Fig. 5.18 Contours of vorticity magnitude on the y = 0 plane using AFT2019b on the S-76 rotor, $\theta_0 = 10°$

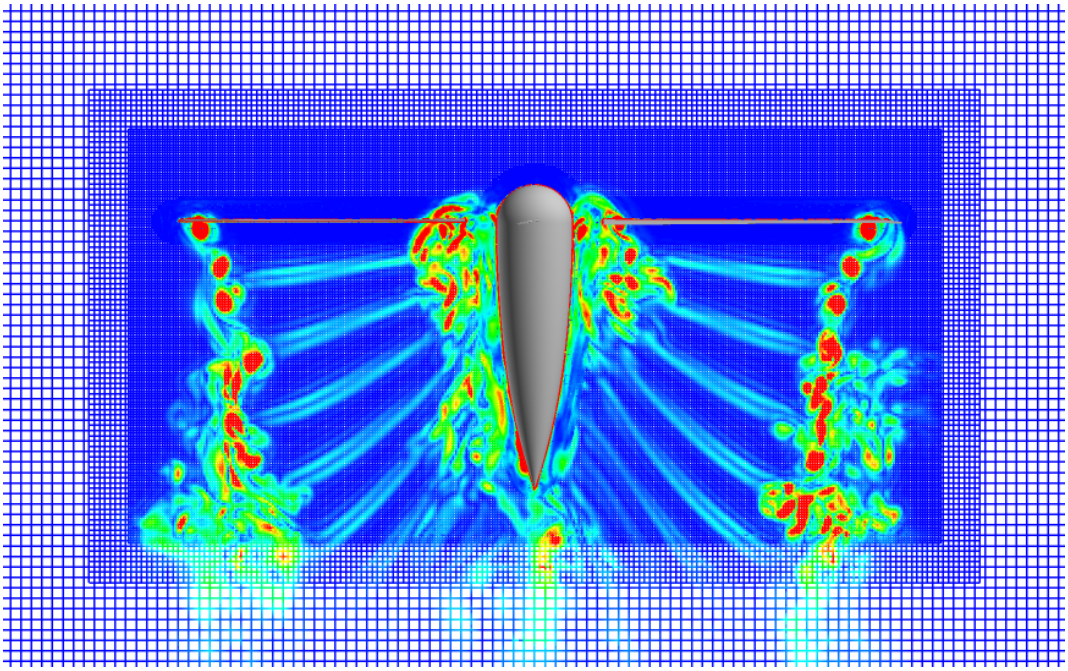


Fig. 5.19 Contours of vorticity magnitude on the y = 0 plane using AFT2019b+CF on the S-76 rotor, $\theta_0 = 10°$

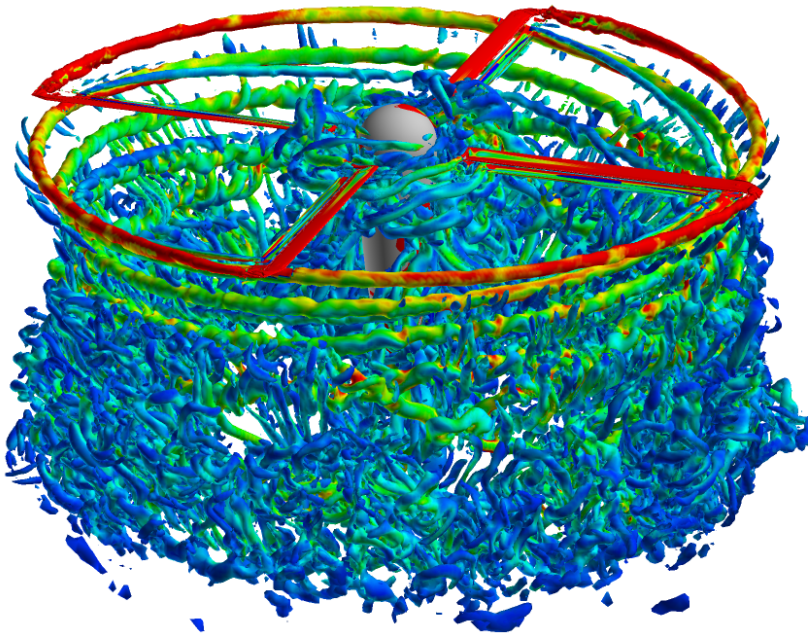


Fig. 5.20 Isosurfaces of the Q-criterion = 0.00009 using SA-neg-RC on the S-76 rotor, $\theta_0 = 10°$

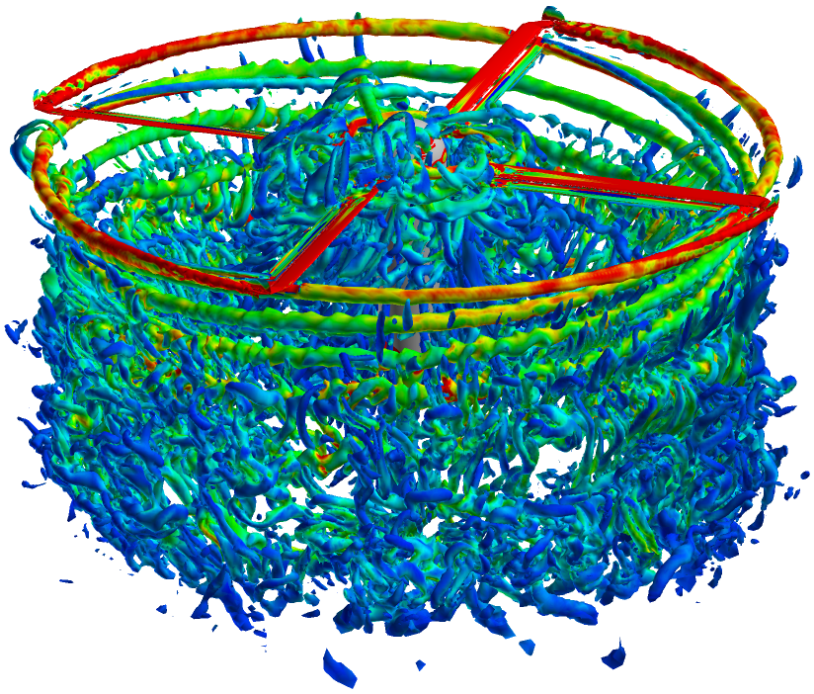


Fig. 5.21 Isosurfaces of the Q-criterion = 0.00009 using AFT2019b on the S-76 rotor, $\theta_0 = 10°$

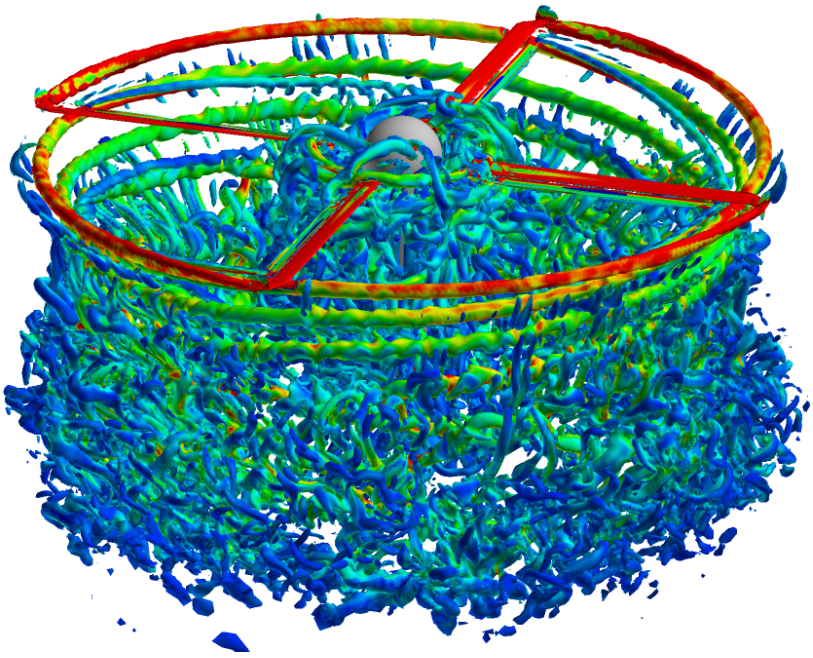


Fig. 5.22 Isosurfaces of the Q-criterion = 0.00009 using AFT2019b+CF on the S-76 rotor, $\theta_0 = 10°$

5.3 Isolated PSP Rotor in Hover

OVERFLOW 2.2n was used to make performance predictions on an isolated, four-bladed PSP rotor in hover at a tip Mach number of 0.58. Simulations were performed using three different turbulence closure methods: the fully-turbulent SA-neg-RC-DDES model, the transitional AFT2019b model, and the transitional AFT2019b+CF model which includes crossflow transition. Two collective pitch cases were simulated, 6° and 10°, in order to predict transition and performance for a moderate thrust level and a high thrust level. Simulations were initialized in the same manner as outlined in Section 5.2 and were carried out for six revolutions in physical time at both collective pitches and for all three turbulence and transition models.

A thrust and torque history using AFT2019b+CF is given in Fig. 5.23. These solutions were restarted from revolution 14 of the AFT2019b solution and were carried out for six additional full revolutions in physical time. When examining the data between revolution 14 and 17, the thrust history shows higher amplitude oscillations than the data after revolution 17. This is likely from initial transients convecting out of the flowfield, as the addition of crossflow transition changes the strength of shear layers and tip vortices. After revolution 17, the transient deviations in thrust from the mean have decreased and thrust and torque values begin to show improved temporal convergence. A residual history for each grid is given in Fig. 5.24 over six revolutions. These residual values, compared to that of the S-76 rotor in Fig. 5.8, show deeper convergence for each grid. Additionally, the main planform grid shows a steady residual value and does not oscillate significantly. This is likely due to improved grid resolution for the PSP blade planform compared to the S-76 blade. The tip cap grid shows 24 individual, evenly-spaced spikes in residual over the full six revolutions, meaning there is some 4/rev frequency in the residual. This occurs at exactly every 1/4 revolution beginning at revolution 14. When this occurs, the blade-local coordinate system is directly in-line with the Cartesian off-body grids. In between each quarter revolution, the tip cap grid communicates with the off-body grids via overset interpolation. This interpolation causes undershoot/overshoot that may explain the improved residual convergence when out of phase with the off-body grids. This effect may be reduced by refining the off-body grid, selecting a higher-order flux reconstruction scheme, or by using a cylindrical off-body grid system.

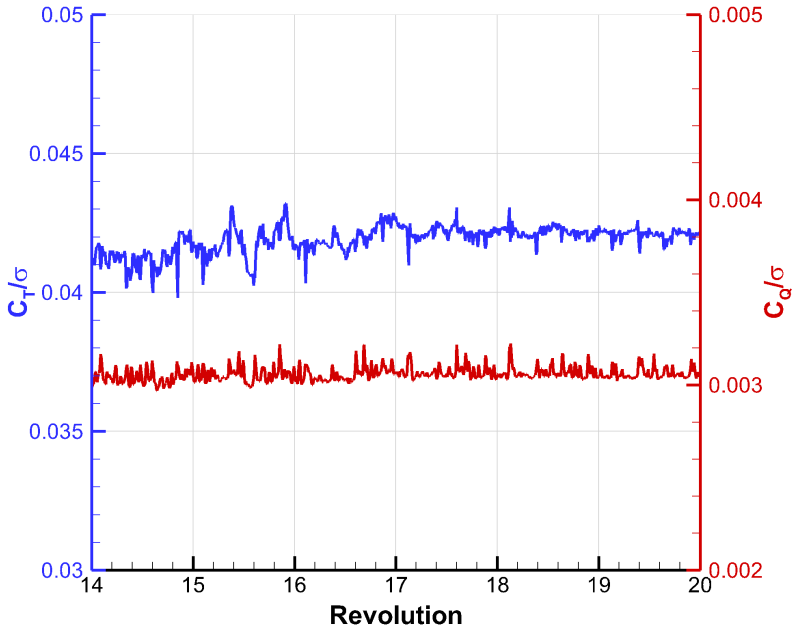


Fig. 5.23 Thrust and torque history for the PSP rotor using AFT2019b+CF, $\theta_0 = 6°$

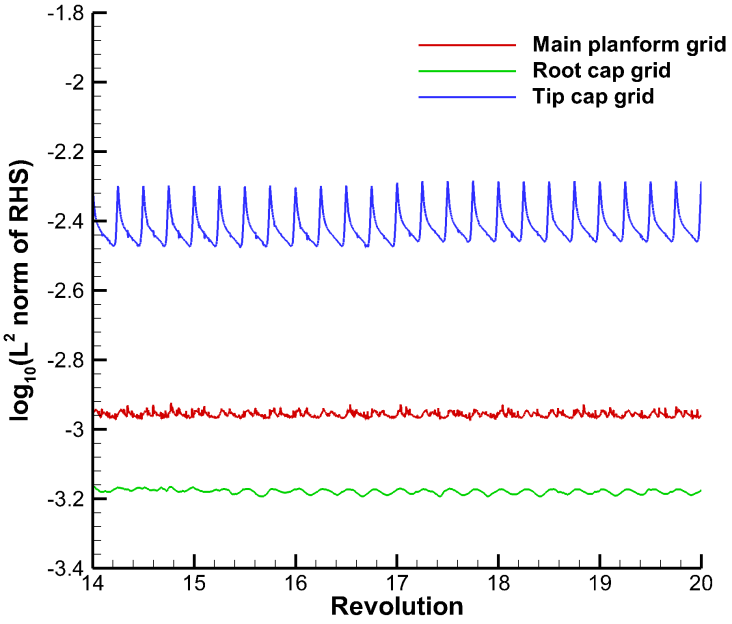


Fig. 5.24 Residual history for the PSP rotor using AFT2019b+CF, $\theta_0 = 6°$

Given in Table 5.3 are predicted rotor performance data for each collective pitch and for each turbulence model. Integrated forces and moments were computed every ten timesteps, or 2.5°. Thrust and torque coefficients were averaged over the final three revolutions of each simulation. Both transition models predicted higher thrust and lower torque at 6° collective pitch compared to the fully turbulent model. This in turn results in a higher predicted FM by several counts for the transition models. At 10° collective pitch, the fully turbulent model predicts higher thrust than AFT2019b, but less thrust than AFT2019b+CF. In general, the transition model with crossflow slightly outperforms the model without crossflow in terms of predicted thrust. But, AFT2019b+CF predicts a higher torque than that of AFT2019b. At 6° collective pitch, the model with crossflow predicts a 0.6 count increase in FM over the model without crossflow. However, at higher collective pitch, both models predict the exact same FM. Separately, AFT2019b and AFT2019b+CF predict different thrust and torque for each collective.

Table 5.3 PSP rotor predicted performance in hover

Collective, θ_o		SA-neg-RC	AFT2019b	AFT2019b+CF
6°	C_T/σ	0.04126	0.04148	0.04214
	C_Q/σ	0.003300	0.003023	0.003068
	FM	0.5800	0.6383	0.6441
10°	C_T/σ	0.08146	0.08115	0.08156
	C_Q/σ	0.007303	0.006915	0.006966
	FM	0.7272	0.7637	0.7637

Predicted FM is plotted with experimental FM as a function of thrust level in Fig. 5.25. The fully turbulent model underpredicts FM by approximately 4 to 5 counts at both thrust conditions, a direct consequence of the high torque and low thrust predicted, comparatively. At moderate thrust, the transition models slightly overpredict FM. The crossflow model predicts a higher thrust for the 6° pitch case and predicts a higher thrust compared to the model without crossflow. However, this still results in a higher FM comparatively. At 10° collective pitch, the differences in thrust for each model are minimal, but the differences in predicted FM are evident due to differences in predicted

torque. Both transition models slightly underpredict FM, by approximately 1 to 2 counts, whereas the fully turbulent model underpredicts FM by 5 counts.

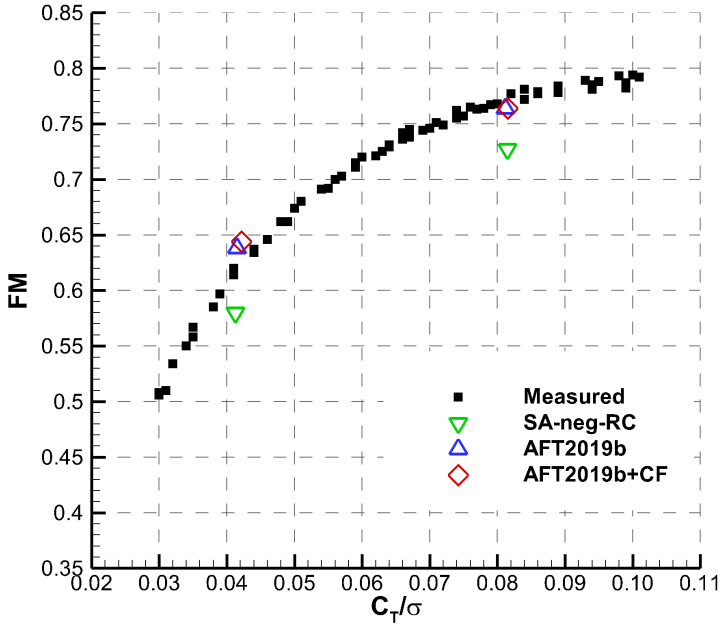


Fig. 5.25 Comparison of figure of merit as a function of thrust level for the PSP rotor

Predicted transition locations were computed using Spalart's turbulence index. Instantaneous transition locations at revolution 13 are shown in Fig. 5.26-5.29. These data were digitized and plotted with experimental data, as shown in Fig. 5.30. Note that experimental transition data were provided as a function of thrust level, rather than as a function of collective pitch. However, the predicted thrust levels match closely to experiment and thus are compared here. For the 6° collective pitch case, transition predicted with AFT2019b shows excellent agreement with that of experiments. On the upper surface, AFT2019b+CF predicts a forward motion in transition around $r/R = 0.90$ which is not seen in experiments. This is the effect of a BVI event on the upper surface, for which the crossflow model detects the helicity of the streamwise vortex and subsequently moves transition forward. The same effect is seen more prominently on the lower surface, where the transition line reflexes forward on either side of $r/R = 0.90$. On the upper

surface, for the regions inboard of $r/R = 0.90$, transition is dominated by Tollmien-Schlichting instabilities. Both transition models accurately predict the transition line up to $r/R = 0.70$, outboard of which both models predict earlier transition compared to experiments. Slightly inboard of $r/R = 0.70$, there is an airfoil blend from the RC(4)-12 to the RC(4)-10. The RC(4)-10 is the airfoil in the region $0.70 < r/R < 0.81$, which is the region that both transition models do not well predict transition locations on the upper surface. The discrepancy in transition may be in the pressure gradient on the airfoil. It may also be that the local angle of incidence is incorrect. The presented simulations have assumed a rigid blade with no deformation. In experiments, there is likely some aerodynamic wind-up or structural loading effects that change the local angle of incidence, and thus the pressure gradient, which is not accounted for in simulations. On the lower surface of the 6° case, AFT2019b matches the experimental transition locations very well and captures that the transition line moves forward at the sweep break. The crossflow model does not capture this phenomenon, or captures this phenomenon too far inboard. At 10° collective pitch, both transition models show excellent agreement with experiments on the upper surface. Given the high collective pitch, there is an adverse pressure gradient across the blade span and enforces Tollmien-Schlichting type transition near the leading edge, for which both transition models can accurately detect. The crossflow model does predict slightly earlier transition near the blade tip than does the model without crossflow and that which is seen in experiments. On the lower surface, both transition models predict transition well up to about $r/R = 0.80$ where transition is dominated by the favorable pressure gradient. In the region about $r/R = 0.90$, a BVI event occurs on the lower surface and greatly affects predicted transition. For AFT2019b+CF, the high strength of the BVI produces strong crossflow instabilities through helicity. This is evident in the wide band of forward transition. The strength of the BVI is felt in AFT2019b as well, suggesting that the BVI event has destabilized the streamwise pressure gradient in its region of influence. The effect of BVI is not seen in the experimentally reported transition locations. Generally, the model without crossflow, AFT2019b, showed better transition predictions compared to the model with crossflow, AFT2019b+CF, suggesting accounting for crossflow may give errant predictions in transition for the PSP rotor in hover.



(a) Upper surface



(b) Lower surface

Fig. 5.26 Instantaneous predicted transition locations using AFT2019b on the PSP rotor, $\theta_0 = 6°$ (blue - laminar, red - turbulent)



(a) Upper surface



(b) Lower surface

Fig. 5.27 Instantaneous predicted transition locations using AFT2019b+CF on the PSP rotor, $\theta_0 = 6°$ (blue - laminar, red - turbulent)



(a) Upper surface



(b) Lower surface

Fig. 5.28 Instantaneous predicted transition locations using AFT2019b on the PSP rotor, $\theta_0 = 10°$ (blue - laminar, red - turbulent)

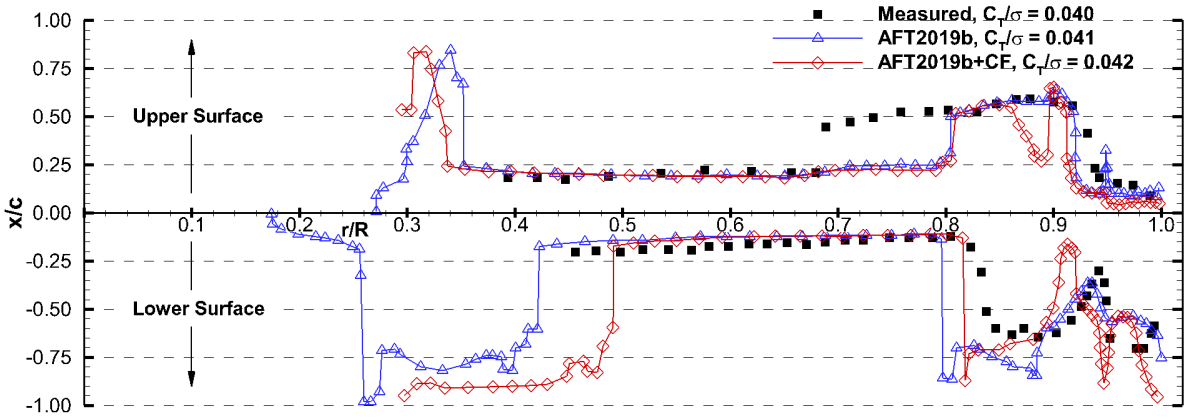


(a) Upper surface

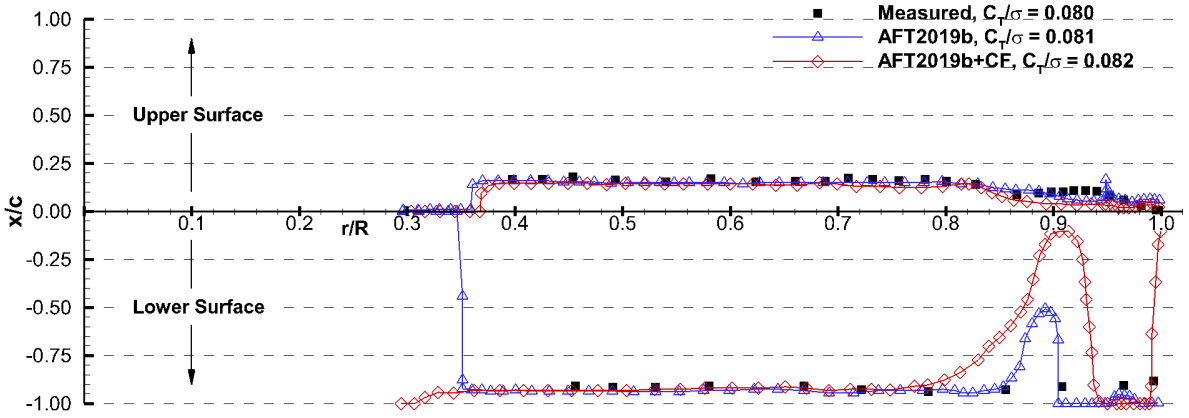


(b) Lower surface

Fig. 5.29 Instantaneous predicted locations using AFT2019b+CF on the PSP rotor, $\theta_0 = 10°$ (blue - laminar, red - turbulent)



(a) $\theta_0 = 6°$



(b) $\theta_0 = 10°$

Fig. 5.30 Digitized instantaneous transition locations on the PSP rotor

With time accurate simulation, there is an unsteadiness in the system as a whole, which is not accurately reflected when examining only instantaneous data. The thrust and torque history do not converge to a single value; rather, they oscillate about some mean value. This unsteadiness in thrust suggests that the bound circulation about the blade oscillates in time as well, which may affect the transition line.

In order to investigate any unsteady behavior in predicted transition, a proper orthogonal decomposition (POD) method based around singular value decomposition (SVD) is employed. An in-house script was written in the MATLAB [206] scripting environment. As the input, this script reads in a series of images. The script reads in each image as a matrix of greyscale values. Then, each image is reshaped to a column vector, upon which each additional image vector is concatenated to create the data matrix X. The data matrix X of Eq. 4.85 is then of size $[pixels, N]$ where $pixels$ is the total number of pixels per image and N is the total number of images. The user may then specify the number of modes to use to reconstruct the image beginning from mode 1 to mode N. The POD reconstruction gives an output of a single image, where the user may specify a specific image (i.e. rotor azimuth) to be reconstructed. In this work, image-based POD is used to quantify the unsteady behavior of predicted transition location on the PSP rotor for both AFT2019b and AFT2019b+CF. Each set of images corresponds to a specific collective pitch, using a specific transition model, for a specific blade surface (e.g. $\theta_0 = 6°$, AFT2019b, lower surface). The data set X is a series of images of transition locations, via Spalart's turbulence index, over the final two rotor revolutions of the specified solution set. Images of the transition locations on a single blade for each surface were created using FieldView in evenly-spaced increments of 5° change in rotor azimuth, or 72 images per revolution. The resulting reconstructed image was taken to be always the first image in the data set, that is the 0° azimuth image at the beginning of revolution five. Given that the primary interest is unsteady behavior of transition, only the first two modes were used to reconstruct the image. These two modes contained 35% to 45% of the total modal energy for each data set examined. This two mode reconstruction is in essence a weighted average of the data set and should show regions on the blade surface in which unsteady transition behavior is expected.

The unsteady transition behaviour was also examined using three methods additional to POD. An in-house FORTRAN code was written and modified to take the ensemble average of the solution files over the final two rotor revolutions, in increments of 5° rotor azimuth. From this,

the turbulence index of the ensemble average can be computed and plotted. This code additionally computes the turbulence index on the blade surface for each solution file and averages those values. It is noteworthy that the turbulence index of the average is not the same as the average of the turbulence index, as this operation is non-commutative. Each of these methods to investigate the unsteady transition behavior are summarized below in Table 5.4

Table 5.4 Summary of unsteady boundary layer investigation methods

Proper Orthogonal Decomposition	Two mode reconstruction of the turbulence index used to represent a weighted average of the data set
Skin friction of the average	Post-processed skin friction of the average solution file of the data set
Turbulence index of the average	Post-processed turbulence index of the average solution file of the data set
Average turbulence index	Average of the turbulence index computed for each individual solution file

Visual comparisons of each of these methods are given in Fig. 5.31-5.38. The POD images are colored in greyscale, where black indicates laminar flow and grey indicates turbulent flow. Note that the image reconstruction process in MATLAB is not lossless and the resolution of the reconstructed images is less than that of the original image. The blurriness in the color scale in some regions is not an artifact of compression loss, but corresponds to regions in which unsteady transition behavior is statistically expected to occur. Darker coloring in a specific region indicates the flow regime is more likely to be laminar in that region. Lighter coloring indicates the flow is more likely to be turbulent in that region. The same holds true for the skin friction contours, in which darker coloring indicates lower skin friction, lighter coloring indicates higher skin friction, and blurred regions indicate regions where unsteady transition behavior is expected. The turbulence index of the average solution and the contours of average turbulence index retain a red-blue color scale for consistency with previous showings of the turbulence index.

Transition detection methods on the upper surface for the PSP rotor at 6° collective pitch using AFT2019b are outlined in Fig. 5.31. Each method shows a large patch of laminar flow from

about $0.85 < r/R < 0.92$ which is where the RC(6)-08 airfoil begins and ends, respectively. The POD method in Fig. 5.31a shows some blurriness near the root region, insinuating the root vortex system has some influence on unsteady transition behavior in the root region. Additionally, the RC(6)-08 region shows some blurriness at the spanwise bounds of the laminar region. Thus, it is expected that there is some minor variation in the spanwise width of this laminar region. When examining skin friction contours of the average solution file in Fig. 5.31b, this variation is also evident. Additionally, the skin friction contours reveal some unsteady skin friction behavior at the blade tip. This is likely an effect of the released tip vortex which will increase local skin friction. The turbulence index of the average solution file in Fig. 5.31c does not reveal the same statistical variation in transition. However, it does reveal regions where the flow is steadily fully laminar or fully turbulent. It is somewhat capable of detecting regions of unsteady transition as evident in the green and yellow colored regions on the blade. But, determining transition locations from the average is not a commutative operation, as the equation for the turbulence index is non-linear. Conversely, computing the skin friction of the average file is commutative as the skin friction is based solely on linear operations. Computing the turbulence index for each solution file, then averaging those values is a commutative operation and offers another method of transition detection, as shown in Fig. 5.31d. These contours show similar trends as the contours of skin friction; however, they do not as well show the smearing of the spanwise bounds of transition in the RC(6)-08 region. This method also better captures the transition "bucket" in this region, whereas the turbulence index of the average does not capture the bucket as well. While the POD method shows unsteady behavior in the near-root region, the contours of the average turbulence index do not show the unsteady behavior near the root. The contours of the average turbulence index show the tip is teal-colored. By determining which value between 0 and 1 corresponds to this teal color, the likelihood of transition here can be determined as a percentage. For example, this teal color corresponds to a turbulence index of 0.3. Therefore, the flow regime at that point in space is expected to be fully turbulent 30% of the time. This method not only shows the unsteady behavior in transition via the colors in-between red and blue, but gives quantitative statistics as to where transition is expected to occur in space and is, in essence, a true turbulent intermittency. Thus, when examining the statistical transition behavior over some time for a rotor in hover, the average turbulence index is the best method of transition detection.



(a) POD two mode reconstruction of the turbulence index (black - laminar, grey - turbulent)



(b) Skin friction contours of the two-revolution average (black - lower skin friction, grey - higher skin friction)



(c) Turbulence index contours of the the two-revolution average (blue - laminar, red - turbulent)

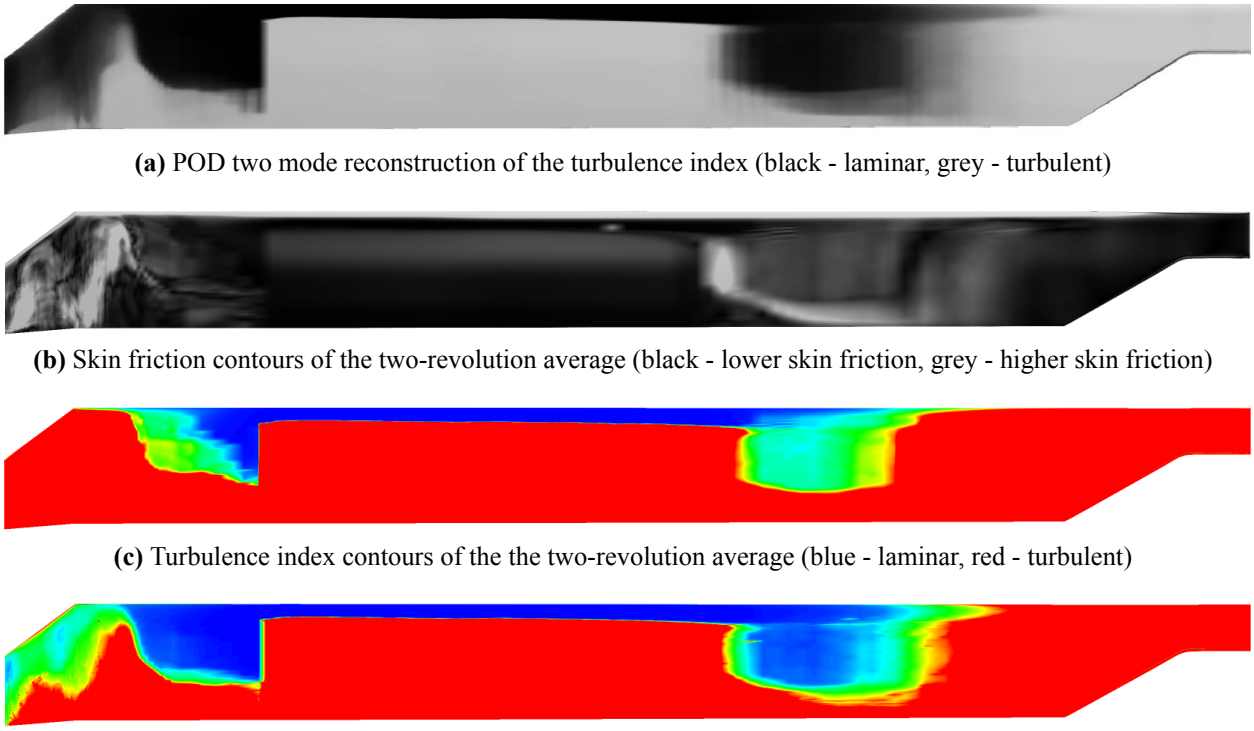


(d) Contours of the average turbulence index over two revolutions

Fig. 5.31 Comparison of unsteady transition detection techniques using AFT2019b on the PSP rotor, $\theta_0 = 6°$, upper surface

The same analysis is performed for the lower surface at 6° collective pitch using AFT2019b, outlined in Fig. 5.32. The POD analysis shows some unsteady behavior near $r/R < 0.45$. This region is outside of the influence of the root vortex system, but may be experiencing some unsteadiness due to low Reynolds number effects on the streamwise pressure gradient. On the blade tip, there is some smearing in the coloration. The tip is neither fully black nor fully grey, but somewhere in-between. This means that the transition on the blade tip is unsteady. There are several distinct, darker lines on the blade tip, indicating that these lines are chordwise locations where transition is more likely to occur on the tip. While the POD method shows these distinct lines, the skin friction method does not show these same lines, but does reveal significant unsteadiness in skin friction on the tip. The skin friction method does show the influence of BVI causing early transition just inboard of the sweep. This effect is also captured when looking at the turbulence index of the average in Fig. 5.32c. This method, however, shows the tip is fully turbulent, which

is certainly not the case. The average turbulence index in Fig. 5.32d highlights a transition bucket in the near-root region and in the RC(6)-08 region. In between those regions, the transition line is expected to be nearly steady, evident in the sharp jump from blue to red. The near-root region shows that transition is expected the occur at approximately the 75% chord, evidenced by the downstream change from blue to green. In the region of $0.92 < r/R < 0.95$, the influence of BVI on transition is shown. The curvature in the transition line due to this BVI event is seemingly unsteady, as evidenced by the green coloring nearest to the sweep break. On the blade tip, the coloring is primarily green, which corresponds to a turbulence index value of 0.5. Thus, this region is expected to be fully turbulent approximately 50% of the time. In the tip region, there is a clear demarcation between green and red, which lines up with a demarcation seen in the POD method. But, the POD method does not offer as clear of statistics on transition.



(a) POD two mode reconstruction of the turbulence index (black - laminar, grey - turbulent)

(b) Skin friction contours of the two-revolution average (black - lower skin friction, grey - higher skin friction)

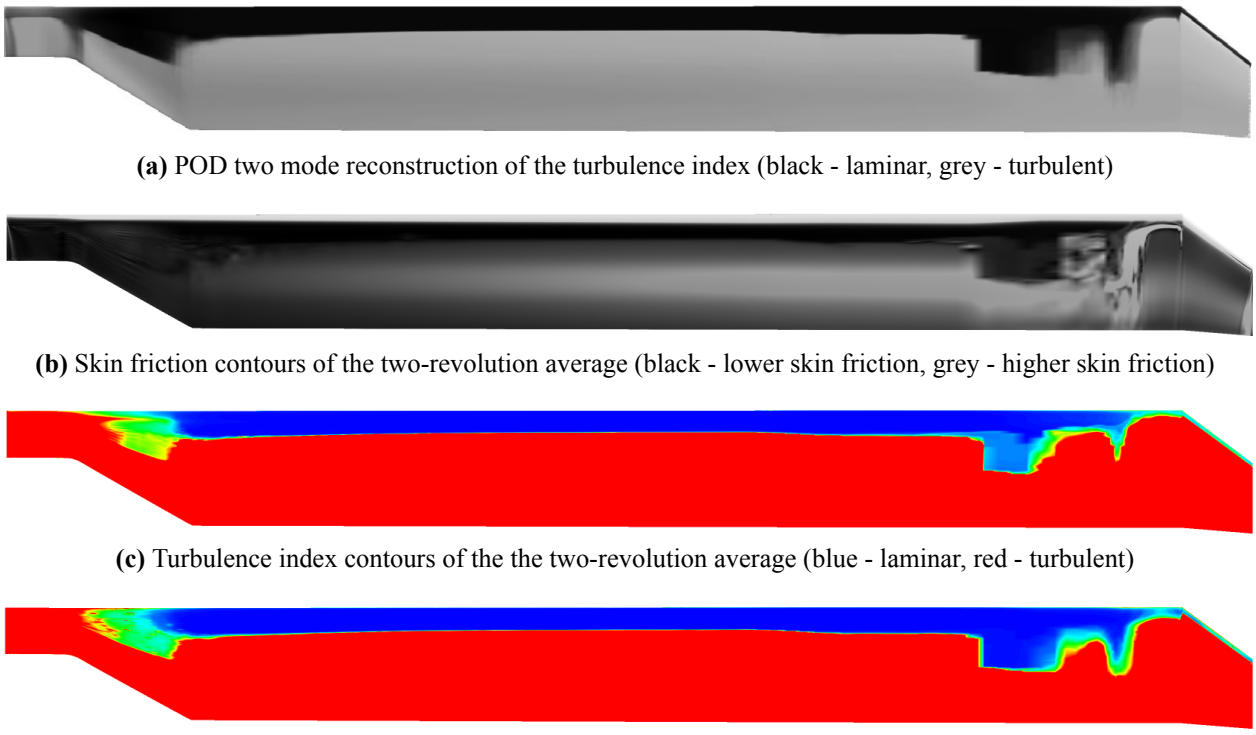
(c) Turbulence index contours of the the two-revolution average (blue - laminar, red - turbulent)

(d) Contours of the average turbulence index over two revolutions

Fig. 5.32 Comparison of unsteady transition detection techniques using AFT2019b on the PSP rotor, $\theta_0 = 6°$, lower surface

With the addition of crossflow on the upper surface in Fig. 5.33, there is shown additional unsteadiness in transition. Both the POD method and skin friction method show a patch of expectedly turbulent flow in the RC(6)-08 region. A BVI event occurs at this location. The blade slices this streamwise vortex such that the upper portion of the vortex impinges on the upper surface. The crossflow model picks up on the helicity of this vortex and moves the transition line forward. However, the predicted transition line is smeared, suggesting that the BVI event is unsteady in its spatial location and/or in its strength. These skin friction contours also show the downstream influence of the BVI on skin friction. The turbulence index of the average solution shows a greater region of turbulent flow in the RC(6)-08 region that is not seen in other methods. When examining contours of the average turbulence index in Fig. 5.33d, predicted transition is steady up until $r/R > 0.9$. Unlike when using AFT2019b, the transition bucket does not fully span the RC(6)-08 region and the influence of the BVI is shown as it is in the other methods. The effect of BVI shows a 10-20% chord band where the coloring is green, indicating that surface flow in this band is expected to be turbulent 50% of the time. The blade tip is almost entirely turbulent, with transition expected to occur at the leading edge.

The lower surface in Fig. 5.34 shows a greater extent of laminar flow in the root region compared to results using AFT2019b. The POD method gives results nearly identical to that determined using AFT2019b, insinuating that crossflow transition has little effect on unsteady transition behavior at this collective pitch. This holds true except the influence of BVI and crossflow results in a slightly wider region of turbulent flow just inboard of the tip. Contours of skin friction of the average solution show regions of high skin friction on the blade tip, suggesting that the flow regime is more likely to be turbulent here. Additionally, the BVI event on the lower surface causes a more drastic increase on skin friction when accounting for crossflow. This may offer an explanation as to why the torque is slightly higher when accounting for crossflow for the 6° collective pitch case. The turbulence index of the average properly shows the regions expected to be steadily laminar or turbulent, but again fails to show the unsteadiness in transition on the tip. The average turbulence index shows steady transition behavior up to $r/R = 0.92$, where the BVI event affects transition. On the tip, between the leading edge and the 30% chord, the flow regime is expected to be laminar a majority of the time. Downstream of this region, the flow regime is expected to be turbulent 50% or more of the time. When comparing these contours to the skin



(a) POD two mode reconstruction of the turbulence index (black - laminar, grey - turbulent)

(b) Skin friction contours of the two-revolution average (black - lower skin friction, grey - higher skin friction)

(c) Turbulence index contours of the the two-revolution average (blue - laminar, red - turbulent)

(d) Contours of the average turbulence index over two revolutions

Fig. 5.33 Comparison of unsteady transition detection techniques using AFT2019b+CF on the PSP rotor, $\theta_0 = 6°$, upper surface

friction contours in Fig. 5.34b, there are striking similarities in the tip region. In the skin friction contours, there is a region of grey on the blade tip and another region of grey just inboard of the sweep break. These same regions are seen in Fig. 5.34d, but the regions are green-colored. Thus indicating that both methods are capable of showing where the flow regime is more likely to be turbulent.

The same transition detection methods on the upper surface for the PSP rotor at 10° collective pitch using AFT2019b are outlined in Fig. 5.35. The POD reconstruction of the turbulence index over time is given in Fig. 5.35a. There is little to no smearing or blurriness in the coloring using this method. At the sweep break, there is some slight blurriness, likely due to the release of a weak streamwise vortex. However, other regions along the blade show clear demarcations between black and grey, suggesting that the transition behavior is relatively steady on the upper surface.



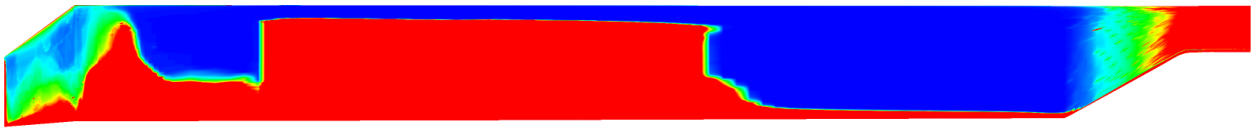
(a) POD two mode reconstruction of the turbulence index (black - laminar, grey - turbulent)



(b) Skin friction contours of the two-revolution average (black - lower skin friction, grey - higher skin friction)



(c) Turbulence index contours of the the two-revolution average (blue - laminar, red - turbulent)



(d) Contours of the average turbulence index over two revolutions

Fig. 5.34 Comparison of unsteady transition detection techniques using AFT2019b+CF on the PSP rotor, $\theta_0 = 6°$, lower surface

Contours of skin friction of the average solution file show the same trends as the POD method. The streamwise vortices released at the sweep break and at the blade tip can be seen in streaks of lighter coloring. These streaks highlight the contraction of these vortices, which is the first step in the contraction of the rotor wake. The turbulence index of the average shows distinct regions of laminar flow and turbulent flow and agrees well with the POD and skin friction methods. Contours of the average turbulence index give similar results to each of the other methods.

On the lower surface, inboard of $r/R = 0.9$, transition locations are seemingly steady, given in Fig. 5.36. The POD method shows some unsteadiness in the root region and also shows significant unsteadiness in transition on the tip. The BVI brings the transition line forward, but in a steady manner. The coloring of the tip shows a high degree of smearing and shows some demarcations in color in the chordwise direction. Overall, the POD method seems to reveal significantly unsteady



(a) POD two mode reconstruction of the turbulence index (black - laminar, grey - turbulent)



(b) Skin friction contours of the two-revolution average (black - lower skin friction, grey - higher skin friction)



(c) Turbulence index contours of the the two-revolution average (blue - laminar, red - turbulent)



(d) Contours of the average turbulence index over two revolutions

Fig. 5.35 Comparison of unsteady transition detection techniques using AFT2019b on the PSP rotor, $\theta_0 = 10°$, upper surface

transition behavior on the tip, with no clear assertion on where transition is more likely to occur. This result is especially highlighted when examining skin friction. The influence of the BVI event on transition is clear, as is the influence of the streamwise vortex at the sweep break. On the tip, there are some color-blocked demarcations that are more clear than that seen using POD. Nevertheless, the skin friction appears to show unsteady transition. This effect is lost in the turbulence index of the average solution file, which shows the tip as fully turbulent, as is common in previous results. In Fig. 5.36d, the flow regime is steadily laminar up to $r/R < 0.85$. The most inboard portion of the transition line due to BVI is seemingly steady. When moving outboard, the effect of BVI on transition becomes more muddled. In the region $0.90 < r/R < 0.95$, the flowfield is predictably laminar up to about the 40% chord. The blade tip is almost entirely green, insinuating the tip is fully turbulent about half the time. This result is common with the POD method and the

skin friction method, as those two methods show significant smearing in the colormap in the tip region.



(a) POD two mode reconstruction of the turbulence index (black - laminar, grey - turbulent)



(b) Skin friction contours of the two-revolution average (black - lower skin friction, grey - higher skin friction)



(c) Turbulence index contours of the the two-revolution average (blue - laminar, red - turbulent)

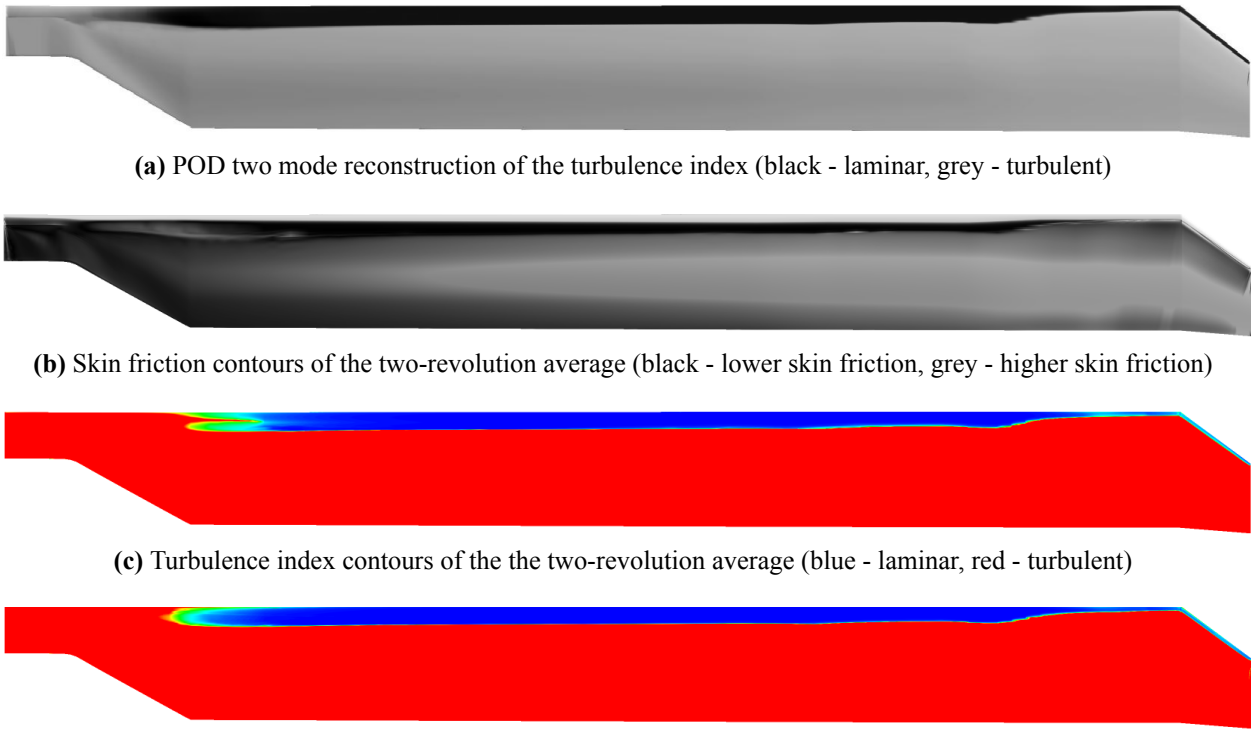


(d) Contours of the average turbulence index over two revolutions

Fig. 5.36 Comparison of unsteady transition detection techniques using AFT2019b on the PSP rotor, $\theta_0 = 10°$, lower surface

The upper surface at 10° collective pitch using the crossflow model seems to show steady transition behavior for each transition detection method employed, as shown in Fig. 5.37. The streamwise vortex released at the sweep break seems to have no influence on predicted transition when using AFT2019b+CF. Overall, the differences in transition prediction methods here are minimal and these predictions using AFT2019b+CF seem to vary little in comparison to using AFT2019b. At such high collective pitch, the crossflow instabilities are weak and transition is dominated by Tollmien-Schlichting instabilities. The lack of any smearing on the blade tip suggests that if there is a BVI event on the blade, it has no effect on the upper surface.

The influence of BVI is evident when examining the lower surface in Fig. 5.38. The POD reconstruction in Fig. 5.38a shows a distinct border between laminar flow and turbulent flow at



(a) POD two mode reconstruction of the turbulence index (black - laminar, grey - turbulent)

(b) Skin friction contours of the two-revolution average (black - lower skin friction, grey - higher skin friction)

(c) Turbulence index contours of the the two-revolution average (blue - laminar, red - turbulent)

(d) Contours of the average turbulence index over two revolutions

Fig. 5.37 Comparison of unsteady transition detection techniques using AFT2019b+CF on the PSP rotor, $\theta_0 = 10°$, upper surface

the location of BVI. Compared to AFT2019b, the BVI pulls the transition line forward, meaning the crossflow model correctly picks up on the helicity of the streamwise vortex. Inboard of the sweep break, the transition line is seemingly steady. Whereas outboard of the sweep break, the transition line is more unsteady. There are a few slightly darker demarcations on the tip indicating statistically likely transition locations. Given the blade tip is primarily dark, the tip is more likely to have a large extent of laminar flow rather than turbulent flow. The released tip vortex enforces fully turbulent flow directly at the tip. Contours of skin friction of the average solution file show a steady, predictable behavior in skin friction inboard of the sweep break. On the tip, the skin friction appears unsteady, but shows a few darker demarcations, similar to that seen in POD. The turbulence index of the average again does not capture the unsteadiness in transition at the tip, but does well in capturing the inboard influence of BVI on transition. Unlike when using AFT2019b, the affect

of BVI on transition is seemingly steady when examining Fig. 5.38d. The demarcations about the BVI event region are clear and well-defined. Outboard of this region, the majority of the blade tip is expected to be laminar. At $r/R > 0.99$, the flow regime is fully turbulent as this is the region in which the released tip vortex rolls up and the strong helicity induces transition.



(a) POD two mode reconstruction of the turbulence index (black - laminar, grey - turbulent)



(b) Skin friction contours of the two-revolution average (black - lower skin friction, grey - higher skin friction)



(c) Turbulence index contours of the the two-revolution average (blue - laminar, red - turbulent)



(d) Contours of the average turbulence index over two revolutions

Fig. 5.38 Comparison of unsteady transition detection techniques using AFT2019b+CF on the PSP rotor, θ_0 = 10°, lower surface

Contours of vorticity magnitude are given in Fig. 5.39 - 5.41. The fully turbulent results show a large amount of vortical content below the root region, with some content above the root region. Unlike the S-76 rotor, there is no hub to block this content from the root region. The tip vortices begin breaking down at 180° wake age, where the tip vortices from 180° wake age and 270° wake age coalesce into a vortex pair. This same phenomenon is evident in the AFT2019b and AFT2019b+CF results. The AFT2019b case shows even a larger extent of vortical content in the root region, but shows little content above the rotor. The tip vortex structure is more stable than the fully turbulent case. Individual tip vortices are still coherent near 270° wake age, but are immersed

in a vortical flow feature, which suggests wake breakdown. Results using AFT2019b+CF show the least wake breakdown comparatively. Vortex pairs form at 180° wake age but do not appear to destabilize the wake structure as a whole.

By examining isosurfaces of the Q-criterion in Fig. 5.42 - 5.44, it can be seen that wake breakdown begins at approximately 180° wake age. The SA-neg-RC case shows secondary vortex braids forming just before 90° wake age. Formation of such braid structures is not seen until later wake ages for AFT2019b and AFT2019b+CF. The root vortex structure is chaotic and shows vortical content above the rotor disk in the root region. This phenomenon is often called "vortex bloom" and occurs during rotor startup. Here, however, this vortex bloom is seen well after rotor startup. Both transitional simulations show negligible vortical content above the rotor disk and all of the root vortex content is contained below the disk.

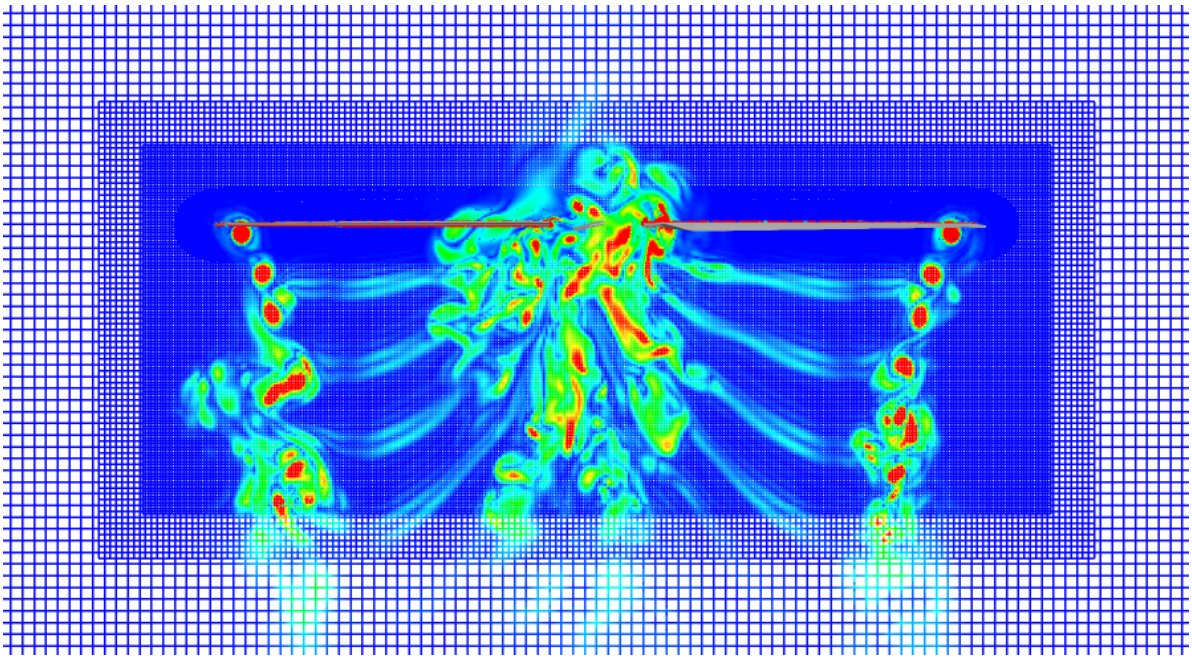


Fig. 5.39 Contours of vorticity magnitude on the y = 0 plane using SA-neg-RC on the PSP rotor, $\theta_0 = 10°$

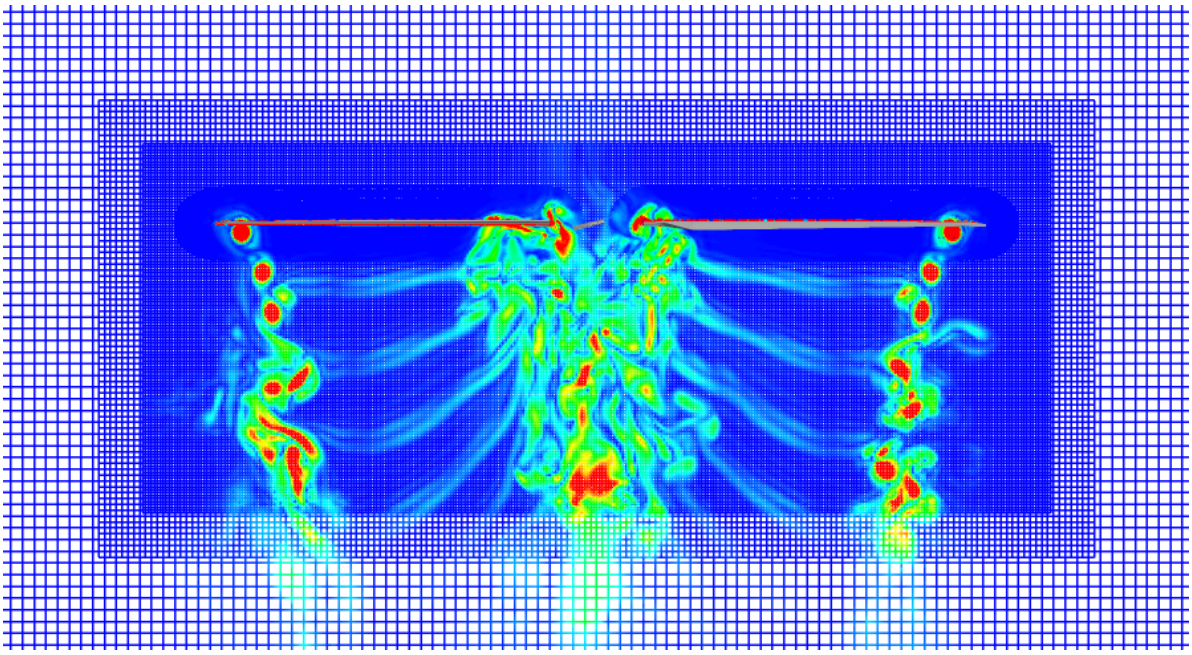


Fig. 5.40 Contours of vorticity magnitude on the y = 0 plane using AFT2019b on the PSP rotor, $\theta_0 = 10^\circ$

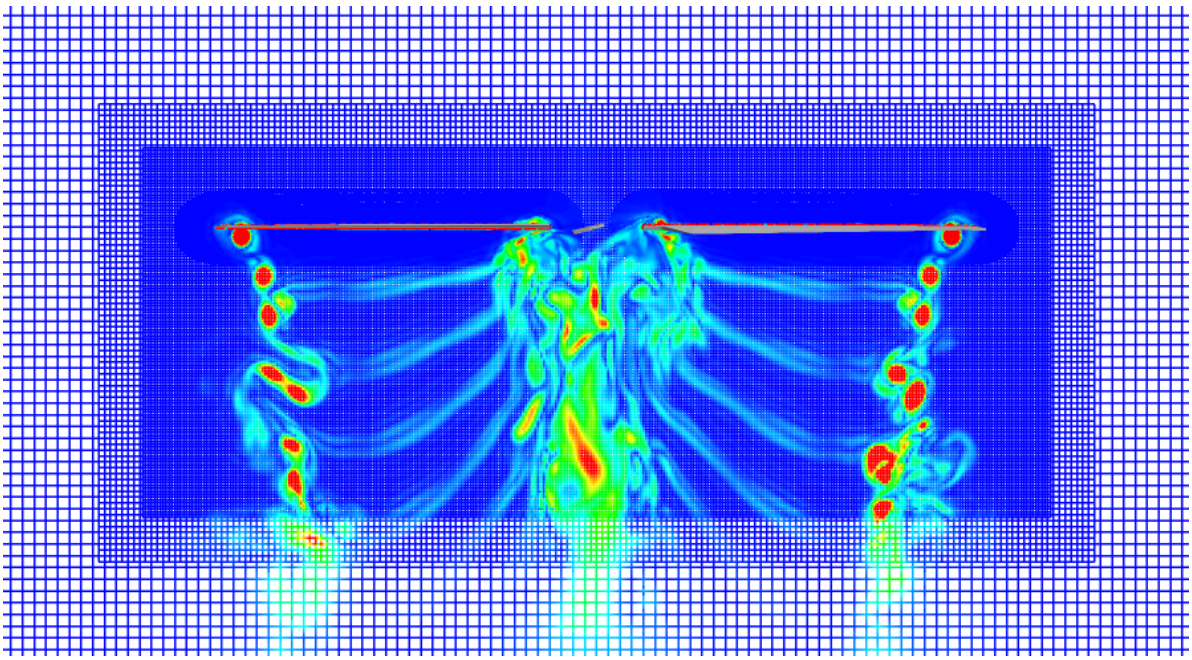


Fig. 5.41 Contours of vorticity magnitude on the y = 0 plane using AFT2019b+CF on the PSP rotor, $\theta_0 = 10^\circ$

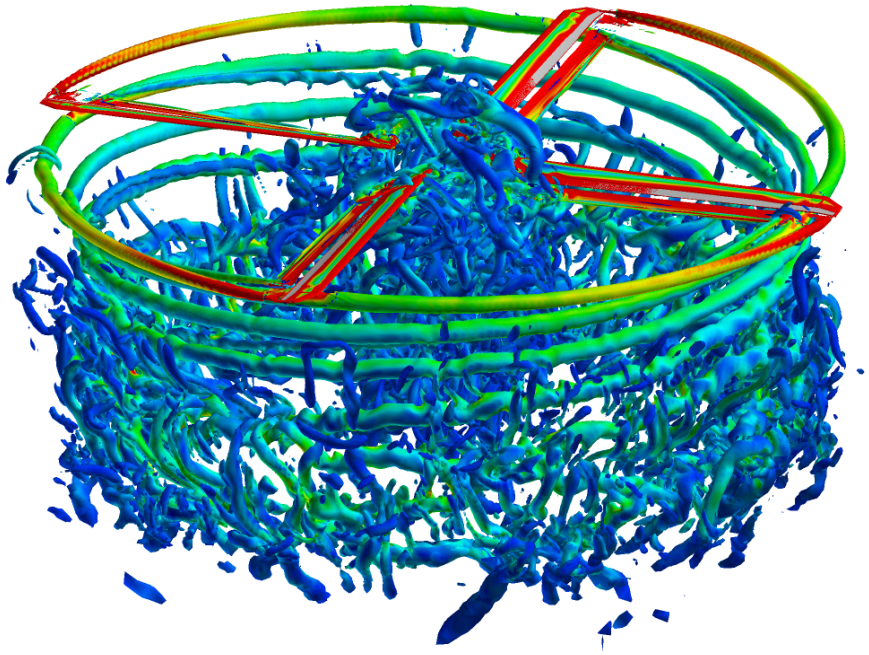


Fig. 5.42 Isosurfaces of the Q-criterion = 0.00009 using SA-neg-RC on the PSP rotor, $\theta_0 = 10°$

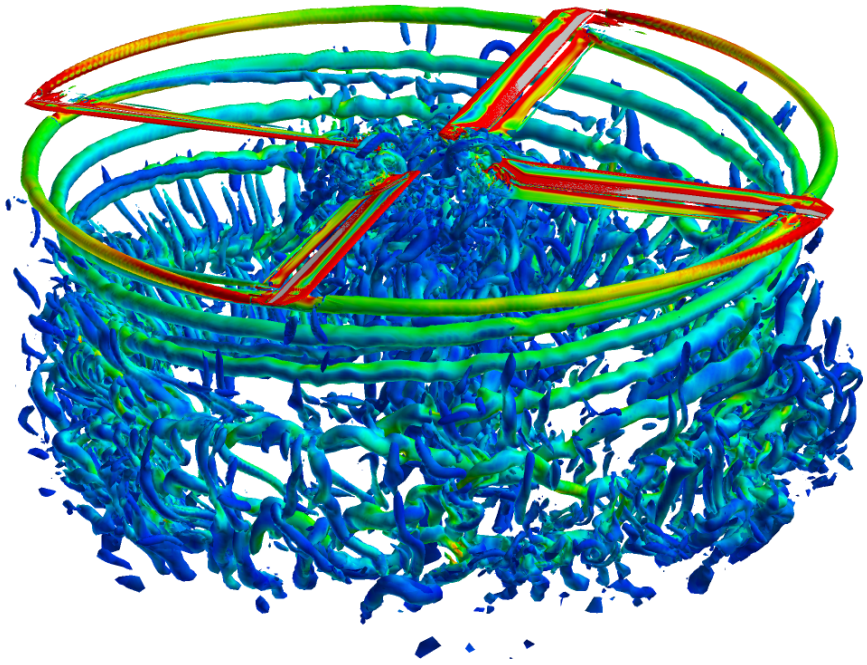


Fig. 5.43 Isosurfaces of the Q-criterion = 0.00009 using AFT2019b on the PSP rotor, $\theta_0 = 10°$

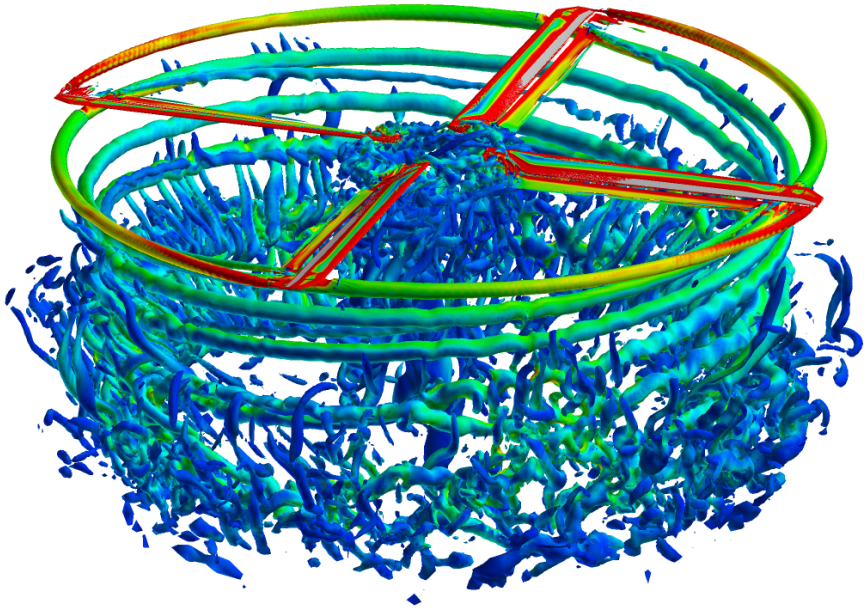


Fig. 5.44 Isosurfaces of the Q-criterion = 0.00009 using AFT2019b+CF on the PSP rotor, $\theta_0 = 10°$

5.4 PSP-ROBIN in Forward Flight

OVERFLOW 2.2n was used to make performance predictions on three-bladed PSP rotor with the ROBIN fuselage in forward flight conditions. Simulations were performed using three turbulence closure methods: the fully-turbulent SA-neg-RC-DDES model, the transitional AFT2019 model, and the transition AFT2019b+CF model which includes crossflow transition. Note that AFT2019 differs from AFT2019b in its computational of the local shape factor H_L. AFT2019 uses the gradient of wall-normal momentum, rather than wall-normal velocity, to compute the local shape factor. In order to provide the best comparisons to experiments, the thrust level $C_T/\sigma = 0.08$ was simulated. The rotor was trimmed to zero 1/rev flapping using coupled CFD-CSD [207] and the resulting trim variables are listed in Table 5.5.

The vehicle was cold-started at a hover tip Mach number of 0.57 in a flowfield with a freestream Mach number of 0.171 such that the rotor advance ratio was 0.30. The simulation was initialized using RANS modeling for the first three rotor revolutions with a timestep corresponding to 1° of rotor rotation. A minimum and maximum CFL number of 1 and 10, respectively, were specified in order to satisfy convergence and stability. Then, the solution was restarted for an additional three revolutions using a DDES approach with global timestepping. The timestep corresponded to 0.25° of rotor rotation. Twenty Newton subiterations were used in order to improve temporal convergence. It was found that three revolutions in physical time was enough to satisfy thrust, torque, and residual convergence. Note that the AFT2019 solution began at revolution 0, and the SA-neg-RC solution and AFT2019b+CF solution were restarted from the AFT2019 case at revolution 3 (end of dual-time start-up).

Table 5.5 PSP-ROBIN forward flight rotor trim variables [207]

Collective pitch, θ_0	7.84°
Lateral cyclic pitch, θ_{s1}	-5.77°
Longitudinal cyclic pitch, θ_{c1}	2.77°
Coning, β_0	3.53°

A thrust history using each turbulence closure model is presented in Fig. 5.45. Only the three revolutions in physical time are shown. Generally, AFT2019b+CF shows higher peaks and higher troughs compared to SA-neg-RC and AFT2019, suggesting that the crossflow model results in a higher average thrust. It is also of note that the mean thrust value is much higher than the value of $C_T/\sigma = 0.08$ reported in experiments. This may suggest that the collective and cyclic pitch variables are not a valid solution for a trimmed flight condition.

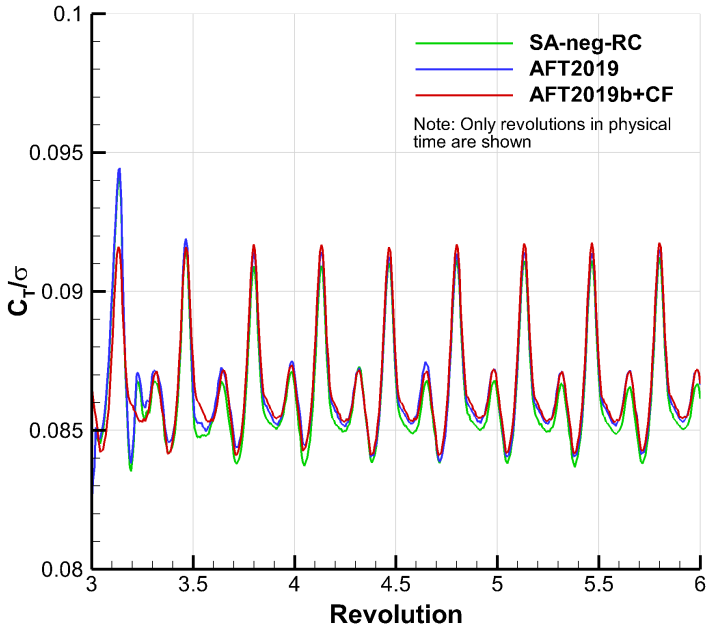


Fig. 5.45 Thrust history for the PSP-ROBIN in forward flight

Similarly, a torque history is given in Fig. 5.46. The fully turbulent model shows the highest peaks and troughs compared to the other models. This is expected as rotor torque is a function of drag on the blade, for which the fully turbulent model has the highest drag. The lowest torque is evident in the curve for AFT2019. In comparison to AFT2019b+CF, AFT2019 has a lower torque curve, meaning that results using the AFT2019b+CF model may have a larger extent of turbulent flow comparatively.

Thrust and torque were averaged over the final two revolutions in physical time, outlined in Table 5.6. All three turbulence closure methods predict a higher thrust than the experiment.

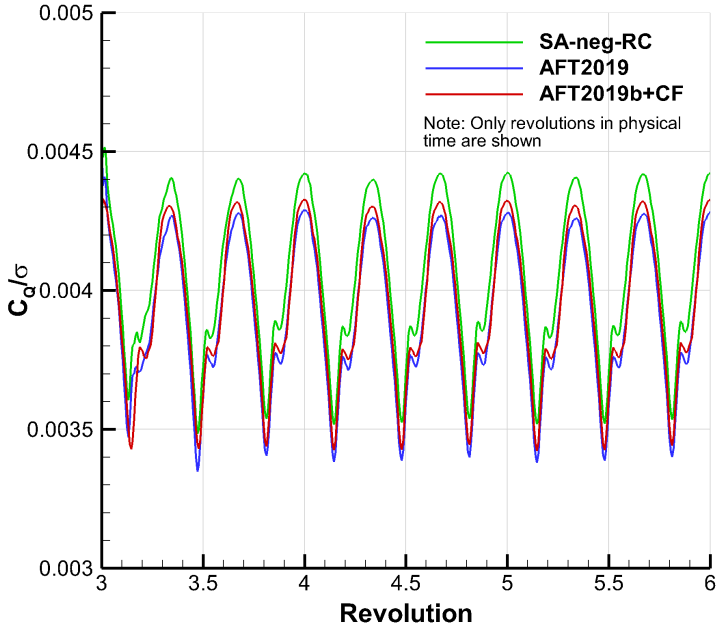


Fig. 5.46 Torque history for the PSP-ROBIN in forward flight

This further suggests the trim state may be incorrect. The highest thrust was obtained using AFT2019b+CF, which predicted both higher thrust and higher torque compared to AFT2019. The fully turbulent model predicted the highest torque and the lowest thrust compared to the two transition models. Note that rotor torque was not reported in the experimental data and comparisons are restricted to predictions only.

Table 5.6 PSP rotor predicted performance in forward flight

	Experiments	SA-neg-RC	AFT2019	AFT2019b+CF
C_T/σ	0.08	0.08612	0.08653	0.08665
C_Q/σ	-	0.004047	0.003911	0.003945

Sample residual convergence for the ROBIN fuselage is given for the AFT2019b+CF case in Fig. 5.47. The ROBIN fuselage grids showed good residual convergence with time. The main body grid shows a notable 3/rev frequency. This occurs when the advancing blade passes over the nose of the fuselage and its downwash affects temporal convergence. The nose cap grid does not see this effect, as the nose cap grid is primarily front-facing and is out of the influence of rotor downwash. The tail cap grid shows the poorest residual convergence as it is immersed in a region of separated, highly-vortical flow sloughing off the tail of the fuselage.

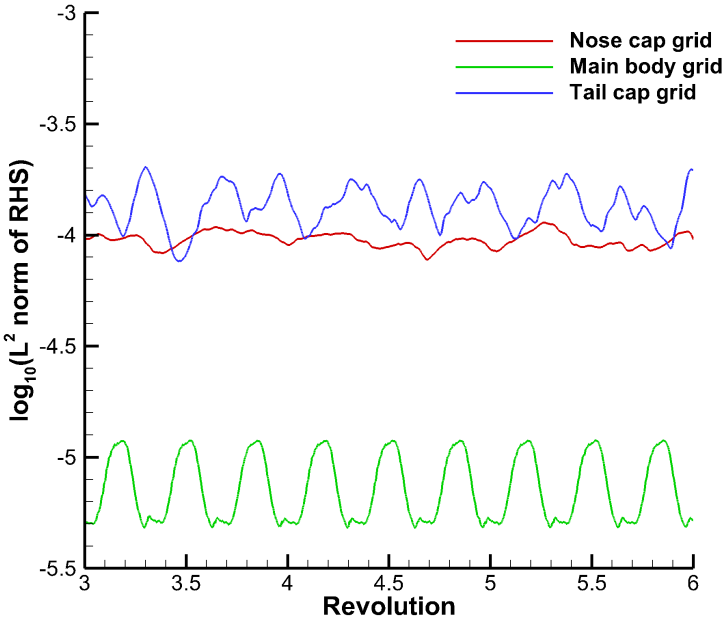


Fig. 5.47 Residual history for the PSP-ROBIN in forward flight using AFT2019b+CF, ROBIN only

For a single blade, residual convergence for the three physical time revolutions using the AFT2019b+CF model is shown in Fig. 5.48. The tip cap grid shows the worst residual convergence comparatively. Just before each integer multiple of a revolution, both the main planform grid and tip cap grid show a spike in residual. This corresponds to a rotor azimuth of approximately 350°. At this azimuth, the blade interacts with a large region of separated flow convecting downstream. This separated flow is highly vortical and turbulent, lending to poorer residual convergence when

the blade passes through this region. Residual convergence exhibits good revolution-to-revolution periodicity, which was determined to be an adequate measure of convergence criterion.

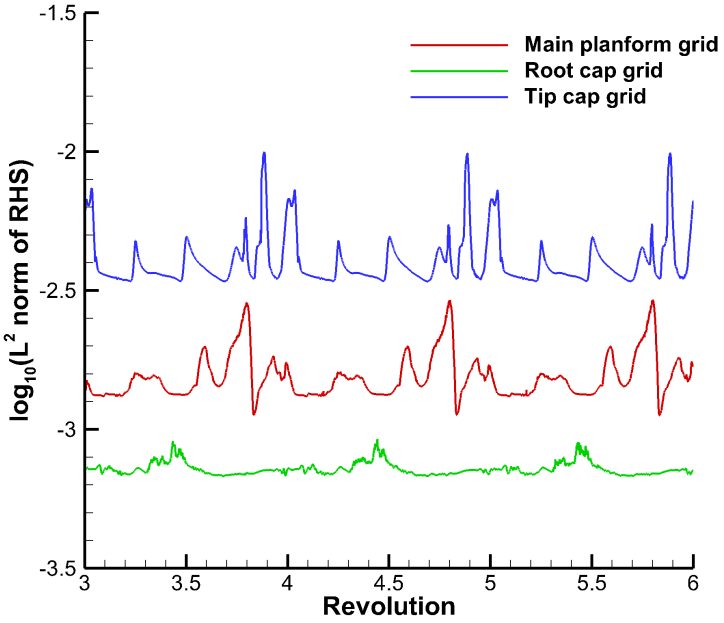
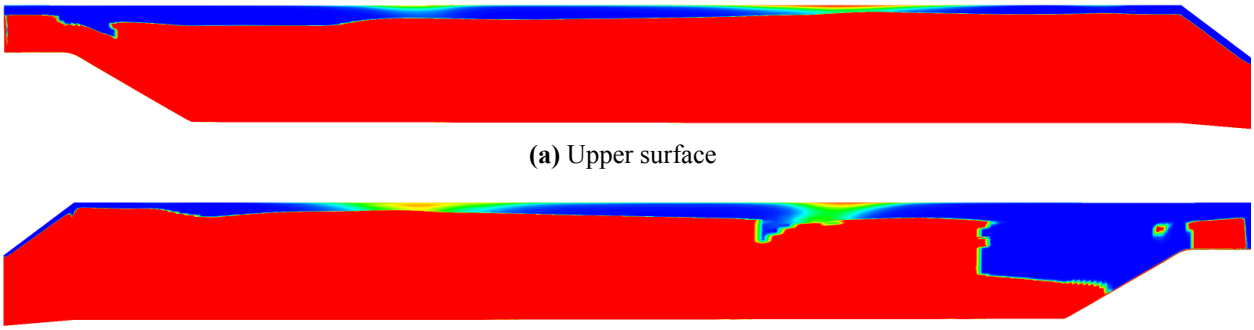


Fig. 5.48 Residual history for the PSP-ROBIN in forward flight using AFT2019b+CF, PSP only

Instantaneous transition locations are visualized using Spalart's turbulence index. Three rotor azimuths were selected: 90°, 150°, and 315°. These selected azimuths represent instances of no crossflow, strong crossflow, and strong crossflow with interaction with a separated flow region, respectively. Each of the selected azimuths has experimentally reported transition lines against which predictions may be compared.

Predicted transition locations at 90° rotor azimuth are shown in Fig. 5.49 and Fig. 5.50. The upper surface is almost entirely turbulent. At this azimuth, the blade is near its minimum pitch in the pitch cycle. For the AFT2019 case in Fig. 5.49, the chordwise transition location is constant across the blade span, including the tip. The lower surface is almost fully turbulent, with transition occurring near $x/c < 0.1$. On the most inboard section of the blade the flow is primarily laminar. Here, the flow is laminar as the local twist angle is high and the pressure gradient on the surface is

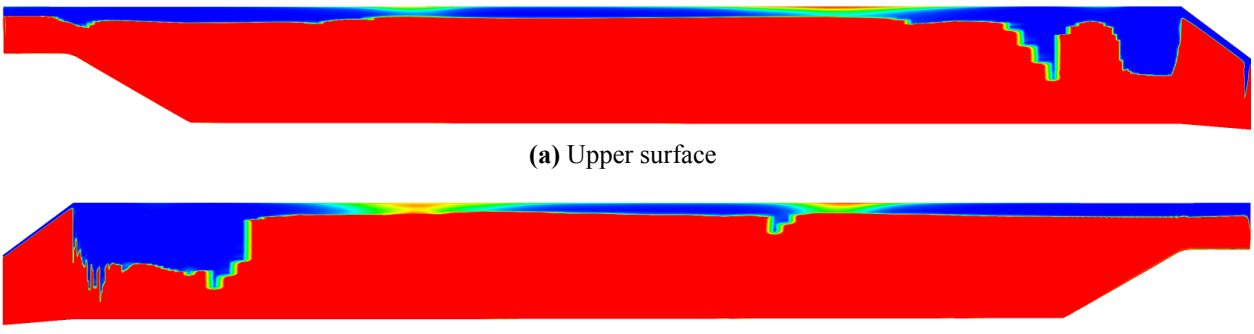
favorable.. When accounting for crossflow, the upper and lower surface show a bucket of laminar flow in the RC(6)-08 region. In this region, the blade passes through the shear layer of the preceding blade. The crossflow model picks up on the helicity of the shear layer and explains the turbulent region in the middle of the RC(6)-08 section on the upper surface. Unfortunately, this does not explain why this region has more laminar flow than the AFT2019 case. The additional laminar flow may be a function of the higher predicted thrust for AFT2019b+CF. The higher predicted thrust of AFT2019b+CF implies that the curvature of the shear layer of the preceding blade is different than the curvature of the shear layer using AFT2019. This may cause some portions of the shear layer to hit or miss the blade surface, effectively functioning as a bypass transition mechanism.



(a) Upper surface

(b) Lower surface

Fig. 5.49 Instantaneous predicted transition locations using AFT2019 on the PSP rotor in forward flight, $\psi = 90°$ (blue - laminar, red - turbulent)

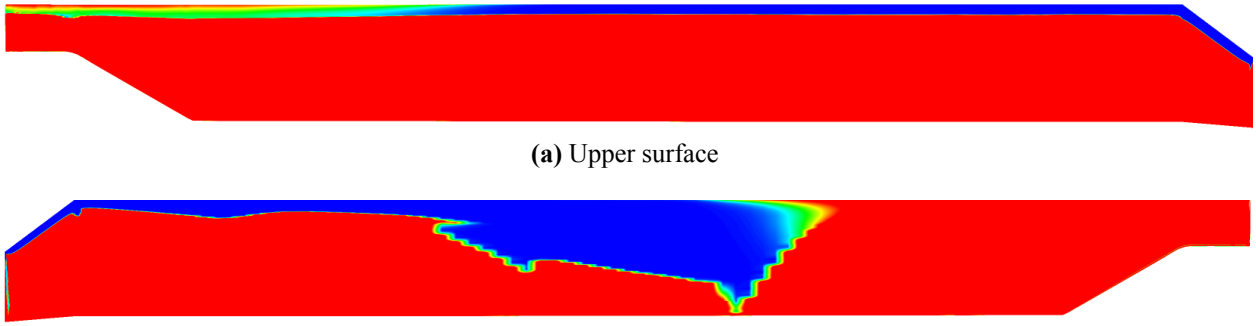


(a) Upper surface

(b) Lower surface

Fig. 5.50 Instantaneous predicted transition locations using AFT2019b+CF on the PSP rotor in forward flight, $\psi = 90°$ (blue - laminar, red - turbulent)

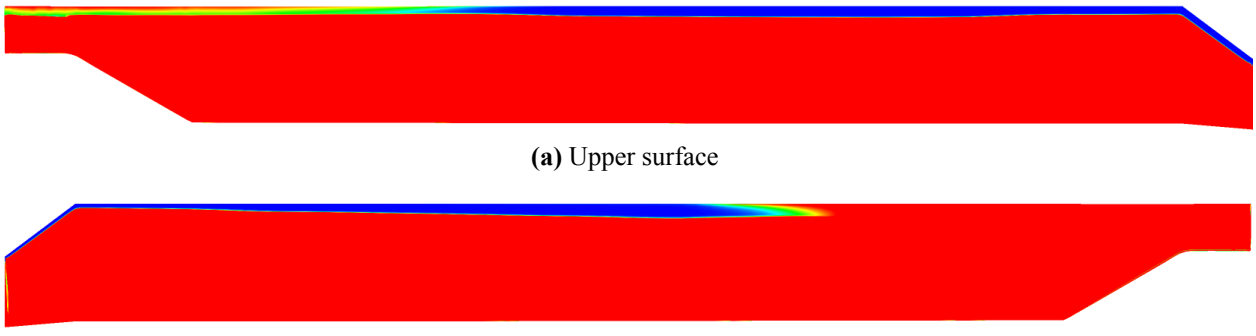
At 150° rotor azimuth, the upper surface is almost entirely turbulent for the AFT2019 and AFT2019b+CF cases, as shown in Fig. 5.51 and Fig. 5.52. The AFT2019b+CF case shows slightly earlier chordwise transition compared to the AFT2019 case, likely a function of the strong crossflow at this azimuth. On the lower surface, AFT2019 shows a region of laminar flow near the midspan of the blade. AFT2019 accounts only for Tollmien-Schlichting instabilities, and these instabilities are weak in this region as the pressure gradient is favorable. However, when examining AFT2019b+CF, this same region is fully turbulent. The blade is immersed in strong crossflow; thus, the crossflow instabilities are strong and supersede the Tollmien-Schlichting instabilities in the midspan region. The crossflow model accounts for this and drives the flow to be fully turbulent.



(a) Upper surface

(b) Lower surface

Fig. 5.51 Instantaneous predicted transition locations using AFT2019 on the PSP rotor in forward flight, $\psi = 150°$ (blue - laminar, red - turbulent)

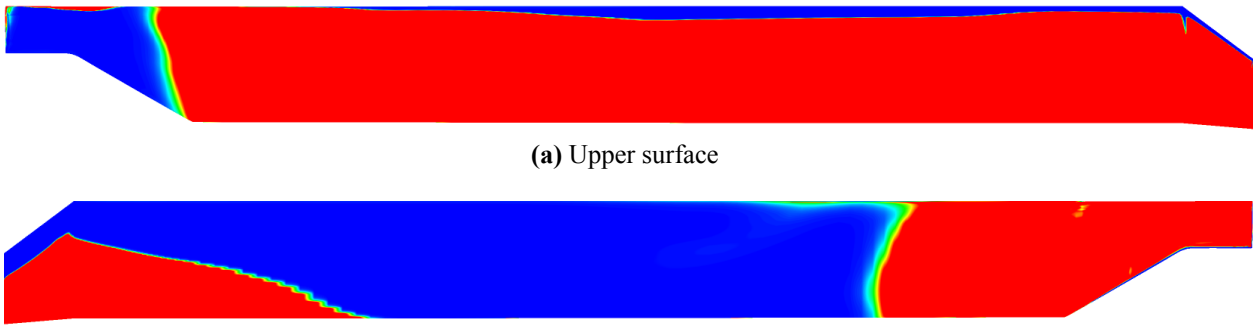


(a) Upper surface

(b) Lower surface

Fig. 5.52 Instantaneous predicted transition locations using AFT2019b+CF on the PSP rotor in forward flight, $\psi = 150°$ (blue - laminar, red - turbulent)

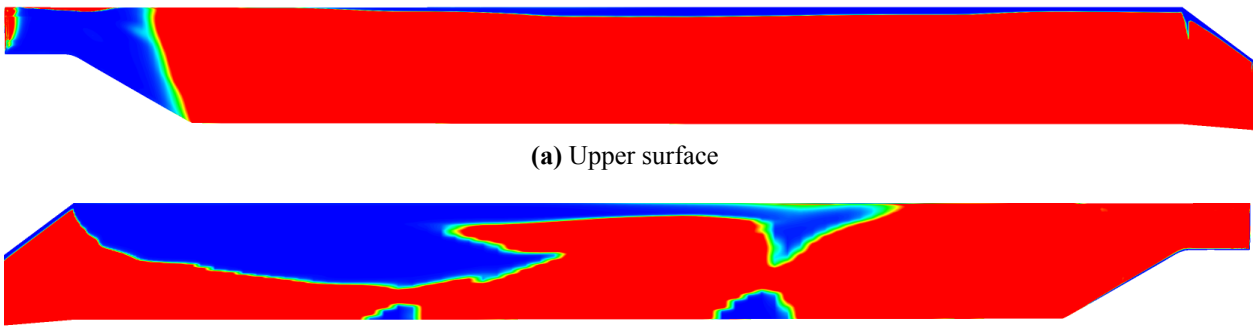
When examining transition at 315° rotor azimuth in Fig. 5.53 and Fig. 5.54, the upper surface is nearly fully turbulent for both cases. At this azimuth, the local pitch angle is near its maximum, and the upper surface experiences an adverse pressure gradient, which causes early transition. For AFT2019b+CF, the upper surface transitions slightly earlier compared to AFT2019, suggesting that crossflow instabilities grow more quickly than Tollmien-Schlichting instabilities. The lower surface experiences a favorable pressure gradient, realized in the late transition for AFT2019. On the lower surface for AFT2019b+CF, the midspan shows earlier transition. At this high pitch, the favorable pressure gradient amplifies crossflow instabilities, causing early transition. Other portions of the blade show large extents of laminar flow and relaminarization, caused by interaction with a region of separated flow convecting downstream.



(a) Upper surface

(b) Lower surface

Fig. 5.53 Instantaneous predicted transition locations using AFT2019 on the PSP rotor in forward flight, $\psi = 315°$ (blue - laminar, red - turbulent)



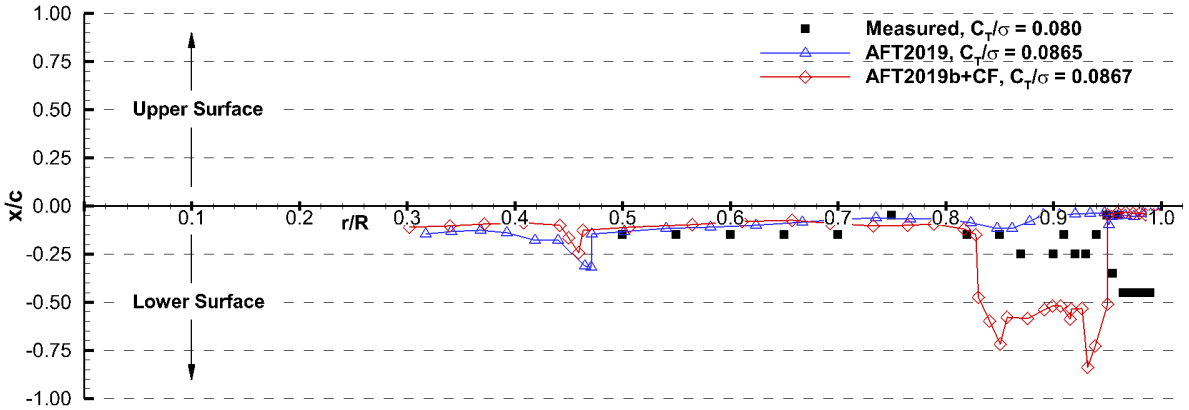
(a) Upper surface

(b) Lower surface

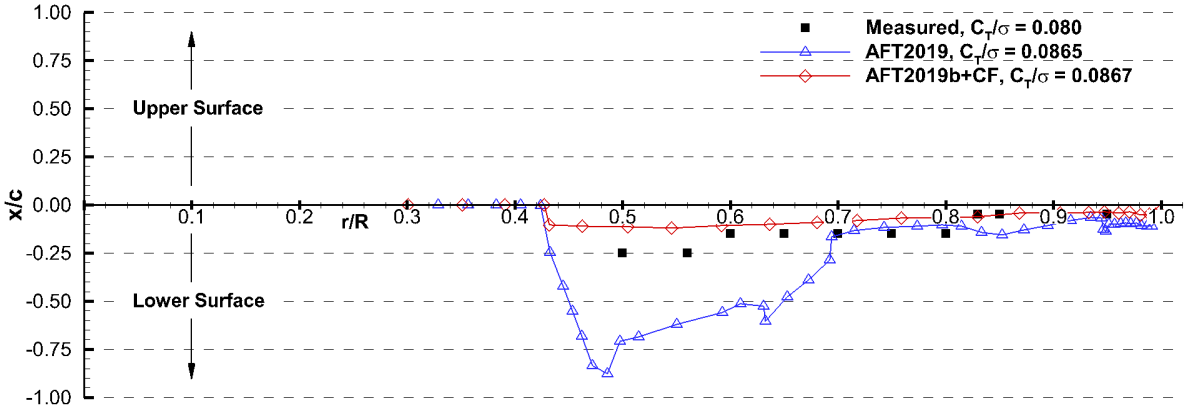
Fig. 5.54 Instantaneous predicted transition locations using AFT2019b+CF on the PSP rotor in forward flight, $\psi = 315°$ (blue - laminar, red - turbulent)

Experiments by Overmeyer et al. [173] reported transition locations on the lower surface for 60° - 150° rotor azimuth and 240° - 330° rotor azimuth. Transition locations were reported for only the outer 50% of the blade and no transition locations were reported for the upper surface. Thus, comparisons between predicted transition locations and experimental transition locations are restricted to the lower surface of the blade. These comparisons are shown in Fig. 5.55 for the same rotor azimuths as previously examined. Note that experimental transition locations were reported in increments of 10% chord. All experimental data are plotted in the middle of this increment. For example, if transition is reported in experiments to occur between 50-60% chord, then the data point plotted is at the 55% chord.

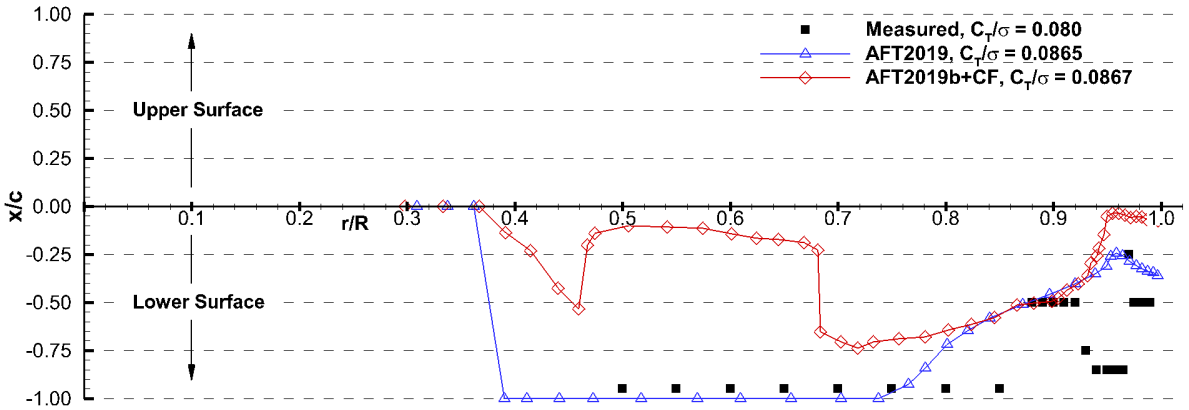
At 90° azimuth in Fig. 5.55a, both transition models predict transition accurately up to approximately $r/R = 0.8$. Outboard of this region, AFT2019 and AFT2019b+CF "straddle" experimentally reported transition. Experiments do show a laminar bucket in the region of $0.85 < r/R < 0.95$, but this bucket is not a deep as is shown in AFT2019b+CF. AFT2019 predicts the transition line to lie nearly on the leading edge across the full blade span. Additionally, the blade tip shows transition near the 50% chord in experiments, whereas both transition models predict transition at the leading edge of the blade tip. For 150° azimuth in Fig. 5.55b, AFT2019b+CF predicts well the experimental transition line. AFT2019 shows a large region of laminar flow which is not seen in experiments. This suggests that transition at this azimuth is largely dominated by crossflow instabilities as would be expected given the high degree of crossflow at this condition. The experimental transition line for the 315° azimuth case in Fig. 5.55c is qualitatively similar to predicted transition lines in Fig. 5.30b. Specifically, the flow regime is nearly, or is, fully laminar, then reflexes forward chordwise near the location where a BVI event is expected. AFT2019 predicts transition well up until $r/R = 0.80$, but does not predict transition well outboard of this region. Transition predictions using AFT2019b+CF do not agree well with experiments over the full blade span. This suggests that predicted crossflow instabilities are too strong and do not play as significant a role in this region. These discrepancies may possibly be attributed to differences in the trim state in the simulation versus the experiment.



(a) $\psi = 90°$



(b) $\psi = 150°$



(c) $\psi = 315°$

Fig. 5.55 Digitized instantaneous transition locations on the PSP rotor in forward flight

To investigate the contributions of rotor thrust by a blade at a given azimuthal position, sectional thrust loading distributions were extracted and plotted in Fig. 5.56 - 5.58 for each turbulence closure model. Five rotor azimuths were selected for investigation: two azimuths with no crossflow, two azimuths with high crossflow, and one azimuth interacting with a region of separated flow. The fully turbulent model in Fig. 5.56 shows a near-constant sectional thrust for a blade at 90° rotor azimuth. The 180° azimuth blade shows the largest contribution to thrust compared to any other azimuth investigated. Moving away from this condition to the 270° azimuth, the sectional thrust level drops expectedly, showing a gradual increase in thrust (i.e. lift) up to $r/R = 0.90$. Advancing to higher rotor azimuths, the thrust level should increase as the relative velocity at the blade leading edge increases. However, the region of separated flow convecting downstream interrupts the thrust loading at 315° azimuth. At 300° azimuth, a separated flow feature begins to form near the root leading edge which grows and is convected downstream and weakly downward. This separated flow impacts the blade at 315° azimuth on the lower surface in the region of $0.45 < r/R < 0.55$, which is evident in the drop in thrust. Bound circulation about the blade is effectively "reset" and circulation strength does not recover to the level expected if there were no interaction with separated flow. At the end of the revolution, at 0° azimuth, the thrust level increases significantly. The set of curves from azimuths 270°, 315°, and 0° are a family of curves that are shifted upward and to the left as relative velocity at the blade leading edge increases. When comparing the fully turbulent results to AFT2019 and AFT2019b+CF, the differences in results are minimal. The curves are nearly identical, with only minor differences between slopes and peak value for a given azimuth. Thus, transition modeling seems to have little effect on predicting sectional thrust loading.

A discrete Fourier transform was performed on the thrust history over the final revolution in physical time, with results plotted in Fig. 5.59. Each turbulence closure model shows strong 3/rev and 6/rev content. These two frequencies are the primary components of integrated thrust. Both transition models show greater 6/rev content than the fully turbulent model. This may be due to incremental increases in lift, due to laminar flow, when a blade passes over the side of the fuselage body, which occurs six times over the full revolution. The higher harmonics contain non-negligible thrust content.

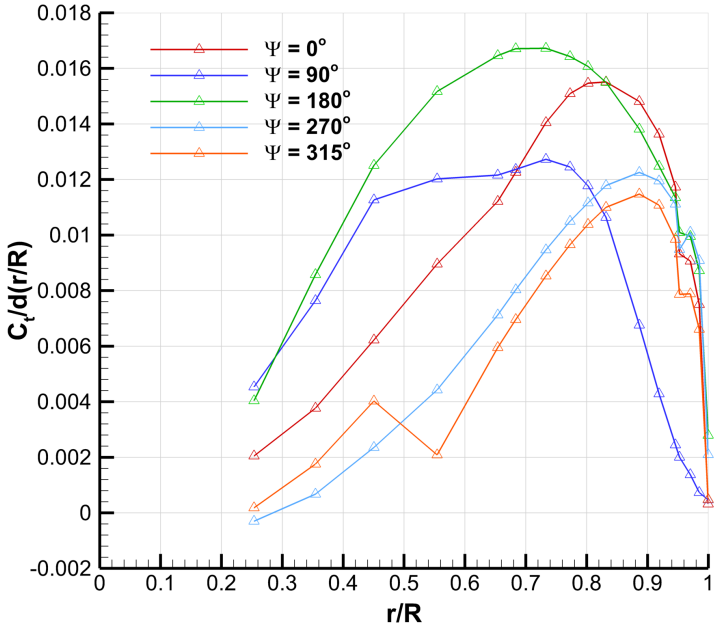


Fig. 5.56 Sectional thrust for the PSP-ROBIN in forward flight using SA-neg-RC

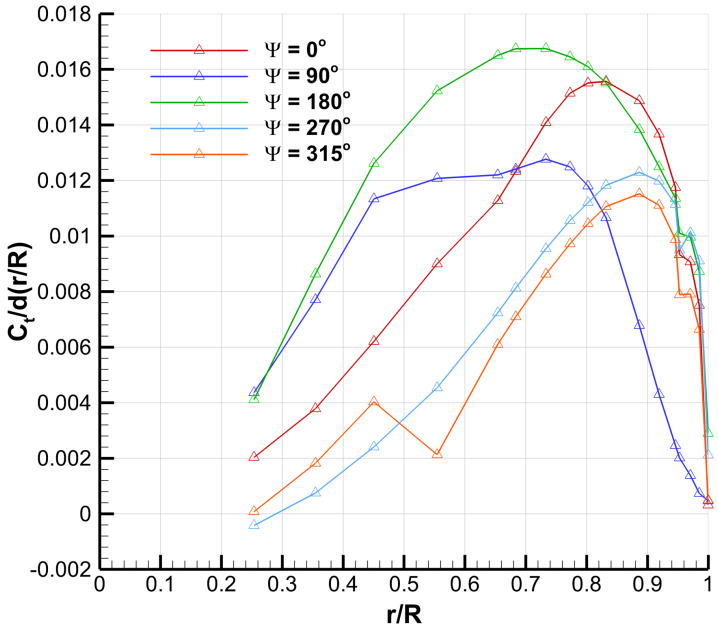


Fig. 5.57 Sectional thrust for the PSP-ROBIN in forward flight using AFT2019

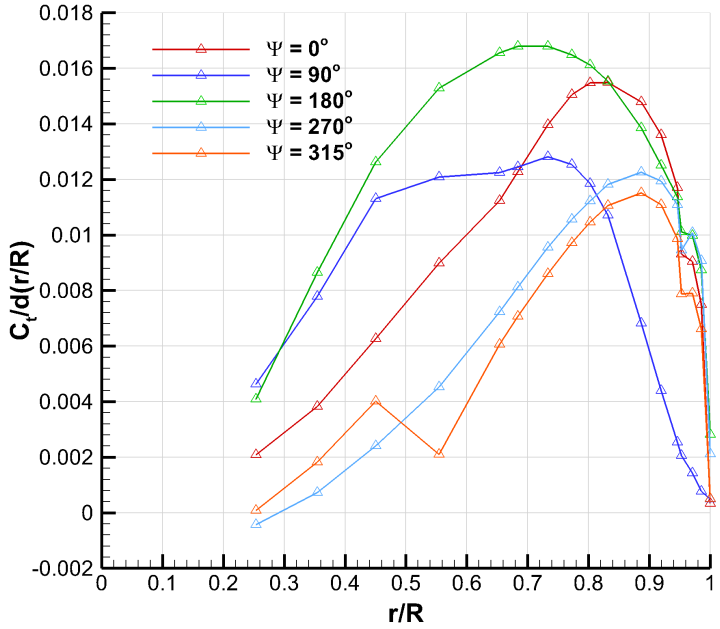


Fig. 5.58 Sectional thrust for the PSP-ROBIN in forward flight using AFT2019b+CF

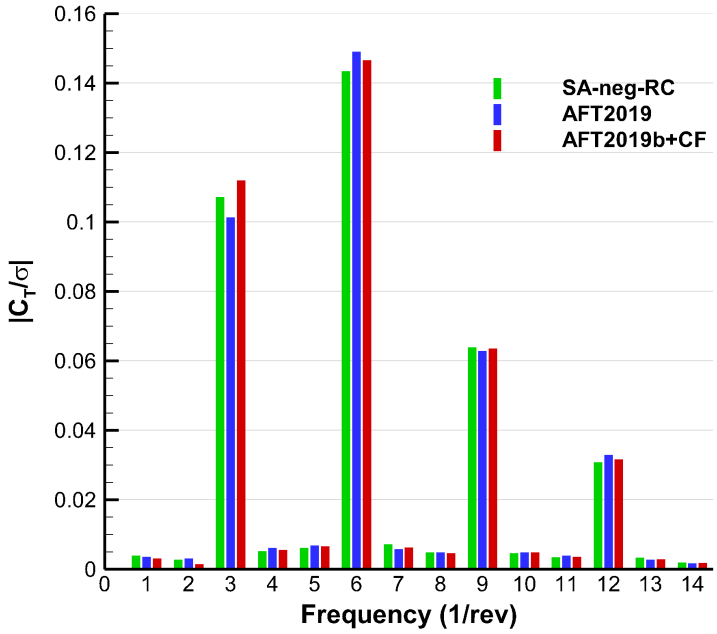


Fig. 5.59 Thrust harmonics for the PSP-ROBIN in forward flight

Sectional torque loading distributions are given in Fig. 5.60 - 5.62. Examining the fully turbulent case, it is evident that sectional torque increases radially until the sweep break at $r/R = 0.95$. The blade at 90° azimuth shows near-constant torque with radius, until there is a sharp increase in torque at the sweep break, where a tip vortex is released. At 180° azimuth, there is a downward spike in torque in the region $0.3 < r/R < 0.45$ in which a BVI event occurs. The shear layer of the preceding blade causes unsteady interaction with the boundary layer causing instantaneously negative torque. On the retreating side of the disk at 270° azimuth, the sectional torque is negligible up to $r/R = 0.55$. On this region of the blade, the sectional thrust is small and thus the drag is also expected to be small. As thrust increases radially outward, so does torque. The 315° azimuth case again shows the influence of the separated flow region in the spike in torque at $r/R = 0.45$. As is the case with thrust, the 0° azimuth curve is familial with the 270° and 315° azimuth curves, being shifted upward and to the left.

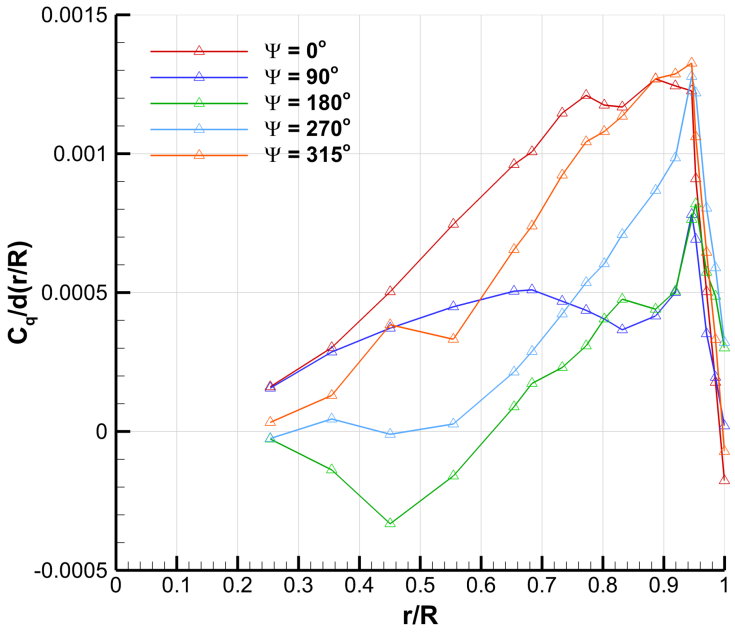


Fig. 5.60 Sectional torque for the PSP-ROBIN in forward flight using SA-neg-RC

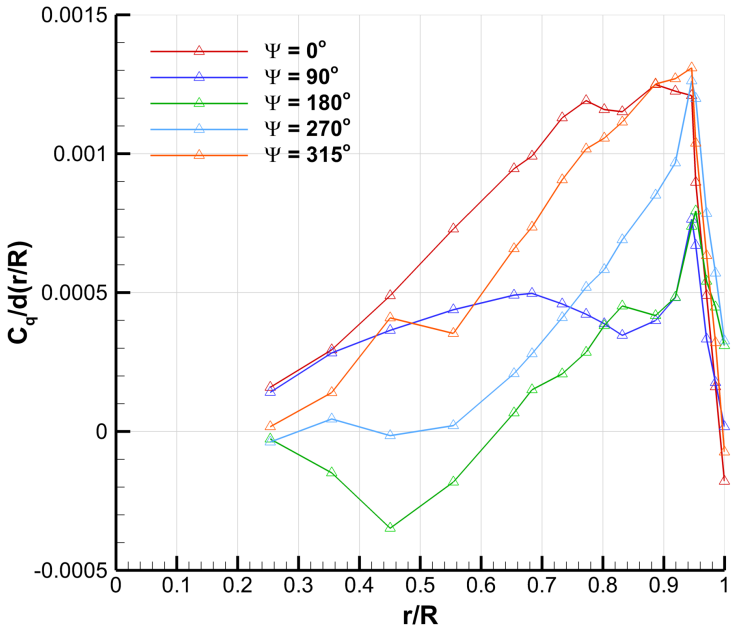


Fig. 5.61 Sectional torque for the PSP-ROBIN in forward flight using AFT2019

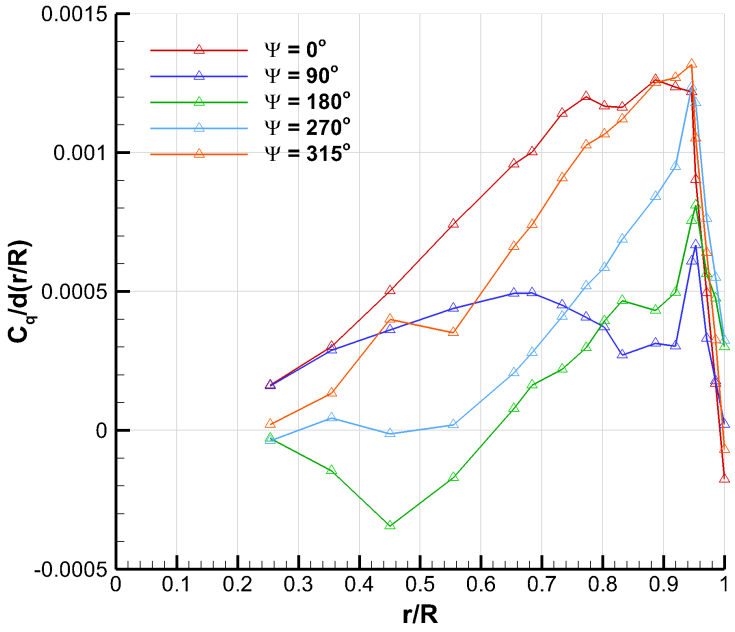


Fig. 5.62 Sectional torque for the PSP-ROBIN in forward flight using AFT2019b+CF

Torque harmonics are plotted in Fig. 5.63 for all three turbulence closure methods. Integrated torque values over one full revolution in physical time were used to determine the frequency content. As expected, the 3/rev frequency is most dominant. SA-neg-RC has the largest 3/rev contribution, a direct result of higher predicted drag due to the fully turbulent assumption. AFT2019b+CF has the largest contribution for 9/rev content, whereas AFT2019 has the largest contribution for 6/rev and 12/rev content. This may be a function of differences in wake vortex strength due to laminar flow.

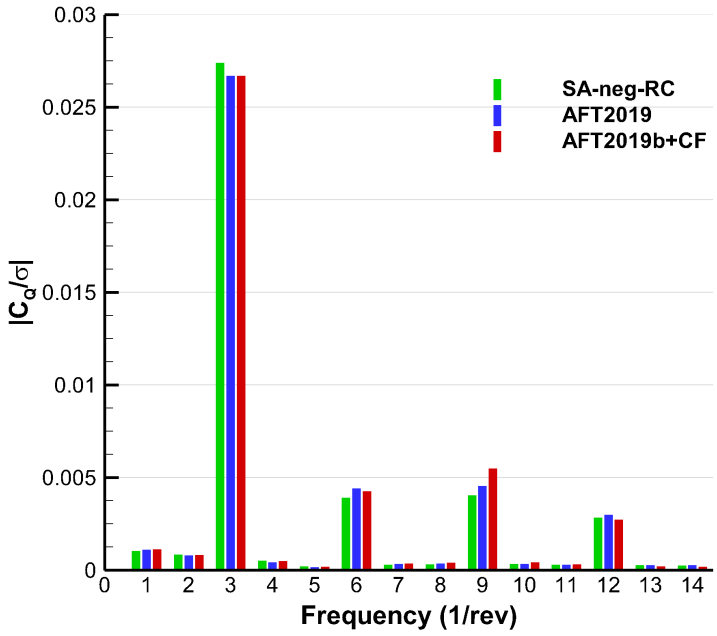


Fig. 5.63 Torque harmonics for the PSP-ROBIN in forward flight

The wake structure is visualized via isosurfaces of the Q-criterion, colored by vorticity magnitude. The wake at revolution 5.5 is shown in Fig. 5.64. The shear layer for each blade and the tip vortices are immediately evident. Additionally evident is a region of highly vortical flow that convects down the length of the fuselage. This vortical flow first forms off the root of the blade at 180° where a broadband instability forms a vortex "braid" structure that resembles a ladder. A similar instability forms off the root of the blade at 60° azimuth. An additional instability

forms on the root of the blade at 300° azimuth, where flow separates from the blade root. These three instabilities, one for each blade, coalesce about the tail of the fuselage and enforce breakdown in the wake of the vehicle. Aft of the tail, the wake is fully broken down. However, flow on the tail itself appears to be attached. The separating flow from the 300° azimuth blade growing on the blade surface eventually sloughs off the blade and is convected downstream. This flow feature is the same feature that causes the erratic behavior in transition, sectional thrust, and sectional torque for the blade at 315° azimuth. When examining the wake structure at revolution 6 in Fig. 5.65, the same vortex braid instabilities are present, most notably at the root of the 120° and 240° azimuth blades. The 240° azimuth blade experiences a BVI event at the root, which begins the growth of a surface instability that eventually causes the root surface flow to separate. At 240° wake age, a super vortex [1] begins to form off the port side of the fuselage. This same vortex-vortex interaction is evident in Fig. 5.64. Similarly, another super vortex is beginning to form on the starboard side. However, these structure likely will not coalesce into a single structure until a later wake age. Although tip vortices remain in tact, instabilities from other blades interact with the tip vortices and eventually destabilize the wake structure.

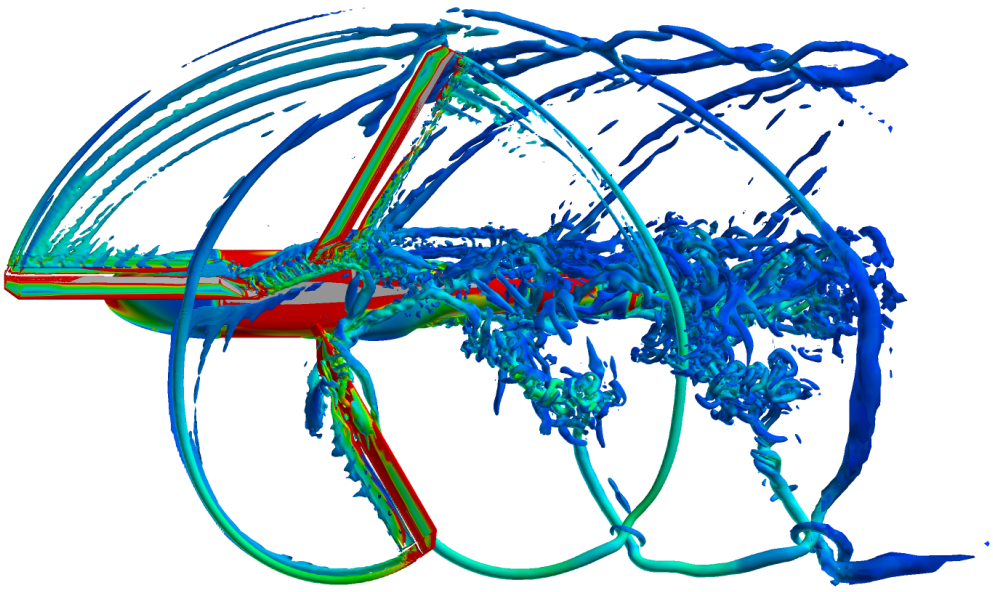


Fig. 5.64 Isosurfaces of the Q-criterion = 0.00005 using AFT2019b+CF on the PSP-ROBIN in forward flight, revolution 5.5

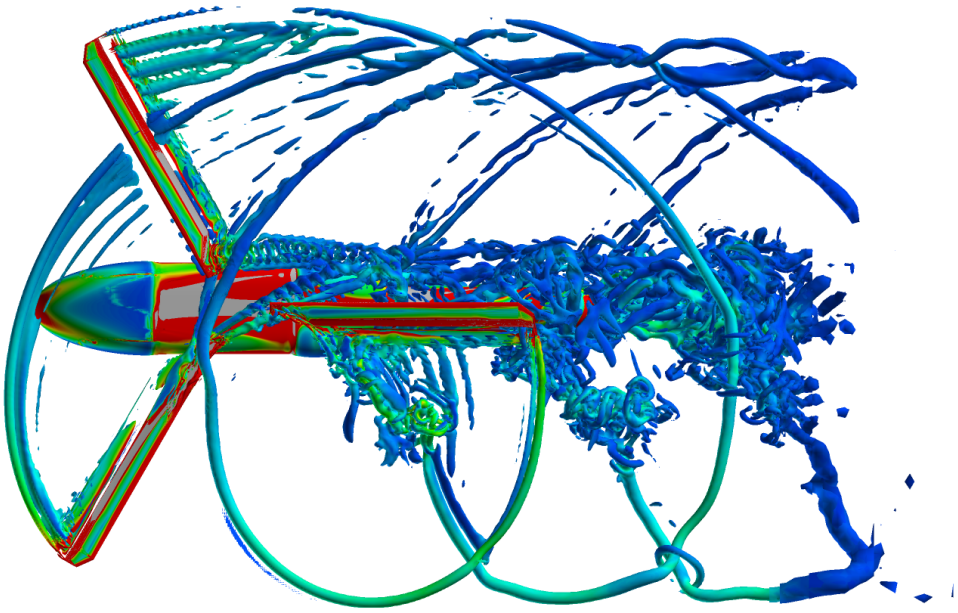


Fig. 5.65 Isosurfaces of the Q-criterion = 0.00005 using AFT2019b+CF on the PSP-ROBIN in forward flight, revolution 6.0

Chapter 6: Conclusions

The Amplification Factor Transport transition modeling framework was modified to include crossflow transition. This transition model was coupled to the Spalart-Allmaras turbulence model in a hybrid RANS/LES framework. The model was implemented in OVERFLOW 2.2n, a structured, overset, Reynolds-averaged Navier-Stokes CFD code designed and maintained by NASA. The crossflow model was validated for several two-dimensional and three-dimensional test cases, showing excellent agreement with experimentally reported transition locations, especially for high crossflow strength. The crossflow transition model was then applied to perform transitional simulations of the S-76 rotor in hover, PSP rotor in hover, and PSP-ROBIN in forward flight. Each of these rotorcraft cases has a suite of rotor performance data and boundary layer transition data and are commonly simulated in the rotorcraft CFD community.

The S-76 rotor was simulated for two collective pitches, 6° and 10° to represent a low-moderate thrust level and a high thrust level. Simulations were performed using the fully turbulent SA-neg-RC model, the transitional AFT2019b model, and the transitional model with crossflow AFT2019b+CF. Simulations predicted thrust well as a function of collective pitch. However, the transition models underpredicted rotor torque at 6° pitch, leading to overprediction of figure of merit. Conversely, at 10° pitch, each model overpredicted rotor torque, leading to underprediction of figure of merit. Unfortunately, no experimental transition data exist and transition predictions were limited to comparison between the two transition models. Both transitional simulations showed a significant extent of laminar flow on the lower surface of the blade. At both collective pitches, a blade-vortex interaction (BVI) event occurs on the lower surface, which affects transition. At the location of such a BVI event, the crossflow model predicts a large region of turbulent flow on the blade surface, whereas the model without crossflow does not, indicating the crossflow model predicts crossflow-induced transition. Additionally, the crossflow model shows the blade tip is fully turbulent where the tip vortex begins to roll up. The wake structure revealed significant wake

breakdown for all simulations, especially so for the fully turbulent case. Tip vortices remained coherent up to approximately 270° wake age. Although the crossflow model did not greatly affect predicted performance or wake structure, it did affect predicted transition locations on the blade surface by increasing the extent of turbulent flow on the blade relative to the model without crossflow.

Similarly, the PSP rotor was simulated in hover at 6° and 10° collective pitch with the same turbulence closure methods. The crossflow model predicted higher figure of merit and thrust for the 6° pitch condition compared to the fully turbulent model and the model without crossflow. Additionally, the crossflow model predicted higher rotor torque, suggesting increased drag on the blade. For that thrust level, the figure of merit was overpredicted by 2-3 counts for the transition models. For the high thrust case at 10° pitch, the transition models underpredicted figure of merit by 1-2 counts. Both the model with crossflow and the model without crossflow predicted the same figure of merit; however, the model with crossflow predicted both higher thrust and higher torque. Instantaneous transition locations showed good agreement with experiments, except for in regions where a BVI event was predicted to occur. In these regions, the crossflow model overpredicted the affect of BVI on transition locations. Although a rotor in hover is, in theory, a periodically steady flowfield, this is not necessarily the case for time-accurate simulations. In order to quantify the unsteady behavior in boundary layer transition, four transition detection methods were employed: proper orthogonal decomposition (POD), skin friction contours of the average solution file, transition locations of the average solution file, and the average transition locations. For each method, data were extracted over two full rotor revolutions in increments of 5° rotor azimuth. These locations were then used to determine the average transition location at any point in time and space. The POD method revealed regions in which transition was expected to be unsteady, but provided only qualitative results. The skin friction method revealed distinct demarcations between regions of expectedly low and high skin friction flows. The transition locations of the average solution file were capable of showing steady transition locations, but failed to show unsteady effects accurately. The average transition locations method revealed regions where the flow regime was more, or less, likely to be turbulent. This method effectively functions as a true intermittency, where each point on the blade has a value assigned to it that reveals the statistical probability that that point is fully turbulent.

The PSP-ROBIN system was simulated in forward flight at an advance ratio of 0.3 in order to match the experimental thrust case $C_T/\sigma = 0.08$. Predictions were made using a fully turbulent model, a transition model without crossflow, and a transition model with crossflow. Each model predicted a thrust level of approximately $C_T/\sigma = 0.86$, much higher than that of experiments. This likely is not a result of the turbulence closure model chosen, but may be a function of an incorrect rotor trim state. Instantaneous transition locations were compared to experimentally determined transition locations for three selected rotor azimuths. The blade at 90° azimuth showed good correlation with experiments for both transition models. However, the transition model with crossflow predicted a pocket of laminar flow in the RC(6)-08 section of the blade that was not seen in experiments. This increase in laminar flow may be a result of the rigid blade assumption. In experiments, the local angle of incidence may be different due to some aerodynamic windup which would in turn effect the transition location in the RC(6)-08 region. The transition model without crossflow did not predict this pocket and better compares to experiments, suggesting the pocket of laminar flow is an artifact of crossflow modeling. At 150° rotor azimuth, the crossflow model agrees well with experiments whereas the model without crossflow does not. This is due to the high crossflow strength at this azimuth, for which the model without crossflow cannot account. Neither model showed good correlation with experiments at 315° azimuth. Predictions showed a large region of separated flow interacting with the blade surface at this azimuth, which may not have occurred in experiments. Sectional thrust loading and sectional torque loading curves were extracted for five rotor azimuths for each turbulence closure model. Interestingly, the blade at 180° azimuth produces the highest total thrust, further suggesting the trim state is incorrect. Differences between sectional loading between the three turbulence closure methods were minimal, except for minor differences in slope and peak values.

In the future, for hover simulations, it is desirable to examine and report the unsteady transition behavior rather than only instantaneously determined transition locations. These instantaneously determined transition locations introduce additional uncertainty if this is the only method of transition detection, as time-accurate simulations are not necessarily steady, even if the simulation is symmetric about some axis. Thus, reporting only instantaneous transition is effectively aliasing the data set and is not necessarily representative of the full data set. To examine the unsteady transition behavior, when averaging Spalart's turbulence index over a specified amount of time, the data set

collapses down to three dimensions: one for the chordwise location, one for the spanwise location, and one for the turbulence index at a given chordwise and spanwise point. Using this method, the average turbulence index functions as a true intermittency, where the value at some point in space is the percentage of time for which the surface flow at that point in space is expected to be fully turbulent. Although this makes comparisons to experimental transition locations more difficult as intermittency is not a direct metric of transition, this method does more accurately represent the results from the simulation at hand.

Simulations for the PSP-ROBIN in forward flight suggest that transition modeling has only a minimal effect on predicted performance. However, this result may be an artifact of an incorrect rotor trim state. Rather than using a specific set of trim variables to make performance predictions using each turbulent closure method, the rotor should be trimmed for each turbulence closure method including aeroelastic effects. This necessitates the use of a comprehensive analysis tool such as CAMRAD or RCAS in order to compute these trim variables. In forward flight, this will guarantee the rotor is trimmed to the correct thrust condition and thus the same thrust condition for each turbulence closure method. This way, the effects of transition modeling compared to fully turbulent modeling may be better assessed. Additionally, comparisons of transition locations across multiple transition models will be more meaningful.

Generally, the model without crossflow performed better, in terms of predicting boundary layer transition, for the rotorcraft test cases. For the transition model validation cases, the crossflow model predicted transition much better. It is noteworthy that each validation case was a static test case with no moving reference frame and thus Galilean-invariance in the crossflow shape factor is of no import to the simulation. On the other hand, the rotorcraft test cases were dynamic, time-accurate, and featured a moving reference frame. For the rotorcraft test cases, the comparatively worse predictions transition locations using the crossflow model may be a consequence of the lack of Galilean-invariance in the crossflow shape which introduces uncertainty in flows with moving reference frames. In the future, a Galilean-invariant crossflow modeling framework not dependent on a local helicity-based shape factor should be employed.

References

[1] Leishman, J. G., *Principles of Helicopter Aerodynamics*, 2nd ed., chapter and pages.

[2] Britannica, "Sikorsky R-4," retrieved February 2020. URL `https://www.britannica.com/technology/R-4`.

[3] Rotaru, C., "Nonlinear Characteristics of Helicopter Rotor Blade Airfoils: An Analytical Evaluation," *Mathematical Problems in Engineering*, Vol. 2013, Article ID 503858, 2013.

[4] Caradonna, F. X., "The Application of CFD to Rotary Wing Problems," *NASA TM 102803*, 1992.

[5] Martin, P. B., Maughmer, M. D., and Somers, D. M., "Airfoil Design and Testing for High-Lift Rotorcraft Applications," *AHS Specialists' Conference on Aeromechanics 2008*, American Helicopter Society, San Francisco, CA, January 2008.

[6] Overmeyer, A. D., and Martin, P. B., "Measured Boundary Layer Transition and Rotor Hover Performance at Model Scale," *55th AIAA Aerospace Sciences Meeting*, AIAA Paper 2017-1872, Grapevine, TX, January 2017.

[7] Grabe, C., Shengyang, N., and Krumbein, A., "Transport Modeling for the Prediction of Crossflow Transition," *AIAA Journal*, Vol. 56, No. 8, 2018, pp. 3167-3178.

[8] Smith, A. M. O., and Gamberoni, N., "Transition Pressure Gradient and Stability Theory," *Douglas Aircraft Company, Report ES 26388*, 1956.

[9] Coder, J. G., "Development of a CFD-compatible Transition Model Based on Linear Stability Theory," *Ph.D. Dissertation*, Department of Aerospace Engineering, The Pennsylvania State University, State College, PA, 2014.

[10] Langtry, R. B., and Menter, F. R., "Correlation-Based Transition Modeling for Unstructured Parallelized Computational Fluid Dynamics Codes," *AIAA Journal*, Vol. 47, No. 12 (2009), pp. 2894-2906.

[11] Coder, J. G., "Further Development of the Amplification Factor Transport Transition Model for Aerodynamic Flows," *AIAA SciTech 2019 Forum*, 2019-0039, San Diego, CA, January 2019.

[12] Langtry, R. B., Sengupta, K., Yeh, D. T., and Dorgan, A. J., "Extending the γ-$\mathrm{Re}_{\theta t}$ Local Correlation based Transition Model for Crossflow Effects," *45th AIAA Fluid Dynamics Conference*, AIAA Paper 2015-2474, Dallas, TX, June 2015.

[13] Shengyang, N., Krimmelbein, N., Krumbein, A., and Grabe, C., "Extension of a Reynolds-Stress-Based Transition Transport Model for Crossflow Transition," *Journal of Aircraft*, Vol. 55, No. 4, 2018, pp. 1641-1654.

[14] Pillai, S. V., and Lardeau, S., "Accounting Crossflow Effects in One-Equation Local Correlation-Based Transition Model," *8th AIAA Theoretical Fluid Mechanics Conference*, AIAA 2017-3159, Denver, CO, June 2017.

[15] Xu., J., Han, X., Qiao, L., Bai, J., and Zhang, Y., "Fully Local Amplification Factor Transport Equation for Stationary Crossflow Instabilities," *AIAA Journal*, Vol. 57, No. 7, 2019, pp. 2682-2693.

[16] Glauert, H., *Aerodynamic Theory*, chapter and pages.

[17] Richards, R. B., *Principles of Helicopter Performance*, chapter and pages.

[18] Gessow, A., and Myers, G. C., *Aerodynamics of the Helicopter*, chapter and pages.

[19] Paul, W. F., and Zincone, R., "Advanced Technology Applied to the UH-60A and S-76 Helicopters," *3rd European Rotorcraft and Powered Lift Forum*, Aix-en-Provence, France, 2006.

[20] Prandlt, L., and Betz, A., *Vier Abhandlungen zur Hydrodynamik und Aerodynamik*, chapter and pages.

[21] Gessow, A., "Effect of Rotor-Blade Twist and Plan-Form Taper on Helicopter Hovering Performance," *NACA Technical Notice 1542*, 1948.

[22] Gustafson, F. B., and Gessow, A., "Effect of Rotor Tip Speed on Helicopter Performance and Maximum Forward Speed," *NACA ARR No. L6A16*, 1946.

[23] Goldstein, S., "On the Vortex Theory of Screw Propellers," *Proceedings of the Royal Society*, Vol. 123, No. 792, 1929, pp. 440-465.

[24] Glauert, H., "The Effect of Compressibility on the Lift of an Aerofoil," *Proceedings of the Royal Society*, Vol. 118, No. 779, 1928, pp. 113-119.

[25] Brotherhood, P., and Stewart, W., "An Experimental Investigation of the Flow through a Helicopter Rotor in Forward Flight," *ARC Reports and Memoranda No. 2734*, 1949.

[26] Glauert, H., "A General Theory of the Autogyro," *ARC Reports and Memoranda No. 1111*, November 1926, pp. 558-593.

[27] Drees, J. M., "A Theory of Airflow Through Rotors and Its Application to Some Helciopter Problems," *The Journal of the Helicopter Association of Great Britain*, Vol. 3, No. 2, 1949.

[28] Coleman, R., Feingold, A. M., and Stempin, C. W., "Evaluation of the Induced-Velocity Field of an Idealized Helicopter Rotor," *NACA ARR L5E10*, June 1945.

[29] Castles, J., W, and De Leeuw, J. H., "The Normal Component of the Induced Velocity in the Vicinity of a Lifting Rotor and Some Examples of Its Application," *NACA TN 2912*, 1953.

[30] Pitt, D. M., and Peters, D. A., "Theoretical Predictions of Dynamic-Inflow Derivatives," *6th European Rotorcraft Forum*, Bristol, England, 1980.

[31] Mangler, K. W., "Calculation of the Induced Velocity Field of a Rotor," *Royal Aircraft Establishment Report Aero 2247*, 1953.

[32] Squire, H. B., "Some Aerodynamic Problems of the Helicopter," *Journal of the Helicopter Association of Great Britain*, Vol. 1, No. 3, 1948, pp. 35-48.

[33] Mangler, K. W., and Squire, H. B., "The Induced Velocity Field of a Rotor," *ARC Reports and Memoranda No. 2642*, 1953.

[34] Ormiston, R. A., "An Actuator Disk Theory for Rotor Wake Induced Velocities," *AGARD Conference Proceedings 111*, 1972.

[35] Peters, D. A., Boyd, D. D., and He, C. J., "Finite-State Induced-Flow Model for Rotors in Hover and Forward Flight," *43rd Annual Forum of the American Helicopter Society*, St. Louius, MO, May 1987.

[36] Peters, H. C. J., D. A., "Finite-State Induced Flow Models Part II: Three-Dimensional Rotor Disk," *Journal of Aircraft*, Vol. 32, No. 2, 1995, pp. 323-333.

[37] Young, C., "The Prediction of Helicopter Rotor Hover Performance using a Prescribed Wake Analysis," *ARC CP No. 1341*, 1974.

[38] Anderson, J. D., *Fundamentals of Aerodynamics*, 5th ed., chapter and pages.

[39] Hariharan, N. S., Egolf, T. A., and Sankar, L. N., "Simulation of Rotor in Hover: Current State, Challenges and Standardized Evaluation," *2014 AIAA SciTech Forum*, AIAA 2014-0041, National Harbor, MD, January 2014.

[40] Landgrebe, A. J., and Cheney, M. C., "Rotor Wakes - Key to Performance Prediction," *AGARD Conference Proceedings 111*, 1973.

[41] Kocurek, J. D., and Tangler, J. L., "A Prescribed Wake Lifting Surface Hover Performance Analysis," *32nd Annual Forum of the American Helicopter Society*, May 1976.

[42] Lewis, R. I., *Vortex Element Methods for Fluid Dynamic Analysis of Engineering Systems,*, chapter and pages.

[43] Egolf, T. A., and Landgrebe, A. J., "Helicopter Rotor Wake Geometry and Its Influence in Forward Flight, Vol. I – Generalized Wake Geometry and Wake Effect on Rotor Airloads and Performance," *NASA CR-3726*, 1983.

[44] Beddoes, T. S., "A Wake Model for High Resolution Airloads," *2nd International Conference on Basic Rotorcraft Research*, 1985.

[45] Landgrebe, A. J., "An Analytical Method for Predicting Rotor Wake Geometry," *Journal of the American Helicopter Society*, Vol. 14, No. 4, 1969, pp. 20-32.

[46] Landgrebe, A. J., "The Wake Geometry of a Hovering Rotor and Its Influence on Rotor Performance," *Journal of the American Helicopter Society*, Vol. 17, No. 4, 1972, pp. 2-15.

[47] Clark, D. R., and Leiper, A. C., "The Free Wake Analysis, A Method for the Prediction of Helicopter Rotor Hovering Performance," *Journal of the American Helicopter Society*, Vol. 15, No. 1, 1970, pp. 3-11.

[48] Sadler, S. G., "Main Rotor Free Wake Geometry Effects on Blade Air Loads and Response for Helicopters in Steady Maneuvers," *NASA CR 2110, NASA CR 2111*, 1971.

[49] Scully, M. P., "Computation of Helicopter Rotor Wake Geometry and Its Influence on Rotor Harmonic Airloads," *NASA CR 2110, NASA CR 2111*, Massachusetts Institute of Technology, 1971.

[50] Bliss, D., and Miller, W. O., "Efficient free wake calculations using analytical/numerical matching and far-field linearization," *45thAnnual American Helicopter Society Forum*, Boston, MA, May 1989.

[51] Sarpkaya, T., "Computational Methods with Vortices," *Journal of Fluids Engineering*, Vol. 111, 1989, pp. 5-52.

[52] Brooks, T. F., Boyd, D. D., Burley, C. L., and Jolly, R. J., "Aeroacoustic Codes for Rotor Harmonic and BVI Noise-CAMRAD:Mod1/HIRES," *2nd AIAA and CEAS Aeroacoustics Conference*, AIAA 1993-1735, State College, PA, May 1996.

[53] Johnson, W., "Rotorcraft Aerodynamic Models for a Comprehensive Analysis," *American Helicopter Society 54th Annual Forum*, Washington, D. C., May 1998.

[54] Saberi, H., Khoshlahjeh, M., Ormiston, R. A., and Rutkowski, M. J., "Overview of RCAS and Application to Advanced Rotorcraft Problems," *American Helicopter Society 4th Decennial Specialists' Conference on Aeromechanics*, San Francisco, CA, January 2004.

[55] Strawn, R. C., and Caradonna, F. X., "Numerical Modeling of Rotor Flows with a Conservative Form of the Full-Potential Equations," *AIAA 24th Aerospace Sciences Meeting*, AIAA 1986-0079, Reno, NV, Jan 1986.

[56] Caradonna, F. X., and Phillippe, J. J., "The Flow Over a Helicopter Blade tip in the Transonic Regime," *Vertica*, Vol. 2, 1978, pp. 43-60.

[57] Phillippe, J. J., and Chattot, J. J., "Experimental and Theoretical Studies on Helicopter Blade Tips at ONERA," *6th European Rotorcraft Forum*, ONERA TP No. 1980-96, Sept. 1980.

[58] Steger, J. L., and Caradonna, F. X., "A Conservative Implicit Finite-Difference Algorithm for the Unsteady Transonic Full-Potential Equation," *AIAA 13th Fluid and PlasmaDynamics Conference*, AIAA 1980-1368, Snowmass, CO, July 1980.

[59] Bridgeman, J. O., Strawn, R. C., and Caradonna, F. X., "An Entropy and Viscosity Corrected Potential Method for Rotor Performance prediction," *44th Annual AHS Forum*, Washington D.C., June 1988.

[60] Caradonna, F. X., and Isom, M. P., "Subsonic and Transonic Potential Flow over Helicopter Rotor Blades," *AIAA Journal*, No. 12, December 1972, pp. 1606-1612.

[61] Jameson, A., Schmidt, W., and Turkel, E., "Numerical Solution of the Euler Equations by Finite Volume Methods Using Runge-Kutta Time-Stepping Schemes," *AIAA14th Fluid and Plasma Dynamics Conference*, AIAA 1981-1529, Palo Alto, CA, June 1981.

[62] Agarkwal, R. K., and Deese, J. E., "An Euler Solver for Calculating the Flow Field of a Helicopter Rotor in Hover and Forward Flight," *19th AIAA Fluid Dynamics, Plasma Dynamics, and Lasers Conference*, AIAA 1987-1472, Honolulu, HI, June 1987.

[63] Kroll, N., *12th European Rotorcraft Forum*, Paper No. 28, Garmisch-Partenkirchen, Germany, September 1986.

[64] Kramer, E., Hertel, J., and Wagner, S., "Computation of Subsonic and Transonic Helicopter Rotor Flow Using Euler Equations," *13th European Rotorcraft Forum*, Paper No. 14, Arles, France, September 1987.

[65] Chen, C. L., and McCroskey, W. J., "Numerical Simulation of Helicopter Multi-Bladed Rotor Flow," *AIAA 26th Aerospace Sciences Meeting*, AIAA 1988-0046, Reno, NV, January 1988.

[66] Reynolds, O., "On the Dynamical Theory of Incompressible Viscous Fluids and the Determination of the Criterion." *Philosophical Transactions of the Royal Society of London. (A.)*, Vol. 186, 1895.

[67] Sankar, N. L., and Tang, W., "Numerical Solution of Unsteady Viscous Flow Past Rotor Sections," *AIAA 23rd Aerospace Sciences Meeting*, AIAA 1985-0129, Reno, NV, January 1985.

[68] Beam, R. M., and Warming, R. F., "An implicit finite-difference algorithm for hyperbolic systems in conservation-law form," *Journal of Computational Physics*, Vol. 22, No. 1, 1976, pp. 87-110.

[69] Rai, M. M., "Navier-Stokes Simulations of Blade-Vortex Interaction Using High-Order Accurate Upwind Schemes," *AIAA 25th Aerospace Sciences Meeting*, AIAA 1987-0543, Reno, NV, January 1987.

[70] Schlinker, R. H., and Amiet, R. K., "Rotor-Vortex Interaction Noise," *NASA CR 3744*, 1983.

[71] Agarwal, R. K., and Deese, J. E., "Navier-Stokes Calculations of the Flowfield of a Helicopter Rotor in Hover," *AIAA 26th Aerospace Sciences Meeting*, AIAA 1988-0106, Reno, NV, January 1988.

[72] Wake, B. E., and Sankar, L. N., "Solutions of the Navier-Stokes Equations for the Flow About a Rotor Blade," *Journal of the American Helicopter Society*, Vol. 34, No. 2, 1989, pp. 13-23.

[73] Srinivasan, G. R., and McCroskey, W. J., "Navier-Stokes Calculations of Hovering Rotor Flowfields," *Journal of Aircraft*, Vol. 25, No. 10, 1988. pp. 865-874.

[74] Srinivasan, G. R., Baeder, J. D., Obayashi, S., and McCroskey, W. J., "Flowfield of a Lifting Rotor in Hover: A Navier-Stokes Simulation," *AIAA Journal*, Vol. 30, No. 10, 1992. pp. 2371-2378.

[75] Roe, P. L., "Approximate Riemann solvers, parameter, vectors, and difference schemes," *Journal of Computational Physics*, Vol. 43, No. 2, 1981, pp. 357-372.

[76] Srinivasan, G. R., Raghavan, V., Duque, E. P. N., and McCroskey, W. J., "Flowfield analysis of modern helicopter rotors in hover by Navier-Stokes method," *AHS International Technical Specialists Meeting on Rotorcraft Acoustics and Rotor Fluid dynamics*, October 1991, Philadelphia, PA.

[77] Srinivasan, G. R., and Baeder, J. D., "TURNS: A Free-Wake Euler/Navier-Stokes Numerical Method for Helicopter Rotors," *AIAA Journal*, Vol. 31, No. 5, 1993, pp. 959-962.

[78] Duque, E. P. N., "A Numerical Analysis of the British Experimental Rotor Program Blade," *Journal of the American Helicopter Society*, Vol. 37, No. 1, 1992, pp. 46-54.

[79] Steger, J. L., Dougherty, F. C., and Benek, J. A., "A chimera grid scheme. [multiple overset body-conforming mesh system for finite difference adaptation to complex aircraft configurations]," *Proceedings of the Applied Mechanics, Bioengineering, and Fluids Engineering Conference*, June 1983, Houston, TX.

[80] Dougherty, F. C., Benek, J. A., and Steger, J. L., "On Applications of Chimera Grid Schemes To Store Separation," *NASA TM-88193*, 1985.

[81] Coder, J. G., and Ortiz-Melendez, H. D., "Transitional Delayed Detached-Eddy Simulation of Multielement High-Lift Airfoils," *Journal of Aircraft*, Vol. 56, No. 4, 2019, pp. 1303-1312.

[82] McCroskey, W. J., "Some Rototcraft Applications of Computational Fluid Dynamics," *NASA TM-100066*, 1988.

[83] Meakin, R. L., "Moving Body Overset Grid Methods for Complete Aircraft Tiltrotor Simulations," *AIAA 11th Computational Fluid Dynamics Conference*, AIAA 1993-3350, Orlando, FL, July 1993.

[84] Pope, S. B., *Turbulent Flows*, 1st ed., chapter and pages.

[85] Smith, A. M. O., and Cebeci, T., "Nuermical Solution of the Turbulent-Boundary-Layer Equations," *DAC Report No. 33735*, 1967.

[86] Baldwin, B. S., and Lomax, H., "Thin-layer Approximation and Algebraic Turbulence Model for Separated Turbulent Flows," *AIAA 16th Aerospace Sciences Meeting*, AIAA 1978-257, Hunstville, AL, January 1978.

[87] Durbin, P. A., and Shih, T. I.-P., "An Overview of Turbulence Modeling," *Transactions on State of the Art in Science and Engineering*, Vol. 15, 2005.

[88] Prandtl, L., "Über ein neues Formelsystem für die ausgebildete Turbulenz," *Mathematik–Physik Klasse, Nachrichten Akademisches Wissenschaft*, 1945.

[89] Wilcox, D. C., *Turbulence Modeling for CFD*, 2nd ed., chapter and pages.

[90] Bradshaw, P., Ferriss, D. H., and Atwell, N. P., "Calculation of boundary-layer development using the turbulent energy equation," *Journal of FLuid Mechanics*, Vol. 28, No. 3, 1967, pp. 593-616.

[91] Townsend, A. A., *The Structure of Turbulent Shear Flow*, 2nd ed., chapter and pages.

[92] Nee, V. W., and Kovasznay, L. S. G., "Simple phenomological theory of turbulent shear flows," *Physics of Fluids*, Vol. 12, 1969, pp. 473-484.

[93] Baldwin, B. S., and Barth, T. J., "A One-Equation Turbulence Transport Model for High Reynolds Number Wall-Bounded Flows," *NASA TM 102847*, 1990.

[94] Spalart, P. R., and Allmaras, S. R., "A One-Equation Turbulence Model for Aerodynamic Flows," *Recherche Aerospatiale*, No. 1, 1994, pp. 5-21.

[95] Allmaras, S. R., Johnson, F. T., and Spalart, P. R., "Modifications and Clarifications for the Implementation of the Spalart-Allmaras Turbulence Model," *7th International Conference on Computational Fluid Dynamics*, ICCFD7-1902, Big Island, HI, July 2012.

[96] Shur, M. L., Strelets, K., M., Travin, A., and Spalart, P. R., "Turbulence Modeling in Rotating and Curved Channels: Assessing the Spalart-Shur Correction," *AIAA Journal*, Vol. 38, No. 5, 2000, pp. 784–792.

[97] Spalart, P. R., "Strategies for Turbulence Modelling and Simulation," *International Journal of Heat and Fluid Flow*, Vol. 21, 2000, pp. 252-263.

[98] Mani, M., Babcock, D. A., Winkler, C. M., and Spalart, P. R., "Predictions of a Supersonic Turbulent Flow in a Square Duct," *51st AIAA Aerospace Sciences Meeting*, AIAA 2013-0860, Grapevine, TX, January 2013.

[99] Argyropoulos, C. D., and Markatos, N. C., "Recent advances on the numerical modelling of turbulent flows," *Applied Mathematical Modeling*, Vol. 39, 2015, pp. 693-732.

[100] Launder, B. E., and Sharma, B. I., "Application of the energy-dissipation model of turbulence to the calculation of flow near a spinning disc," *Letters in Heat and Mass Transfer*, Vol. 1, No. 2, 1974, pp. 131-137.

[101] Shih, T.-H., Liou, W. W., Shabbir, A., Yang, Z., and Zhu, J., "A new k-ϵ eddy viscosity model for high reynolds number turbulent flows," *Computers & Fluids*, Vol. 24, No. 3, 1995, pp. 227-238.

[102] Yakhot, V., Orzsag, S. A., Thangam, S., Gatski, T. B., and Speziale, C. G., "Development of turbulence models for shear flows by a double expansion technique," *Physics of Fluids A: Fluid Dynamics*, Vol. 4, No. 7, 1992, pp. 1510-1520.

[103] Menter, F. R., "Review of the shear-stress transport turbulence model experience from an industrial perspective," *International Journal of Computational Fluid Dynamics*, Vol. 23, No. 4, 2009, pp. 305-316.

[104] Kolmogorov, A. N., "Equations of turbulent motion of an incompressible fluid," *Proceedings of the USSR Academy of Sciences*, Vol. 30, No. 4, 1941, pp. 299-303.

[105] Launder, B. E., and Spalding, D. B., *Mathematical Modeling of Turbulence*, chapter and pages.

[106] Wilcox, D. C., "Reassessment of the Scale-Determining Equation for Advanced Turbulence Models," *AIAA Journal*, Vol. 26, No. 11, 1988, pp. 1299-1310.

[107] Wilcox, D. C., "Formulation of the k-omega Turbulence Model Revisited," *AIAA Journal*, Vol. 46, No. 11, 2008, pp. 2823-2838.

[108] Menter, F. R., "Two-equation eddy-viscosity turbulence models for engineering applications," *AIAA Journal*, Vol. 32, No. 8, 1994, pp. 1598-1605.

[109] Smirnov, P. E., and Menter, F. R., "Sensitization of the SST Turbulence Model to Rotation and Curvature by Applying the Spalart–Shur Correction Term," *Journal of Turbomachinery*, Vol. 131, No. 4, 2009.

[110] Durbin, P. A., "Near-wall turbulence closure modeling without "damping functions"," *Theoretical and Computational Fluid Dynamics*, Vol. 3, No. 1, 1991, pp. 1-13.

[111] Hanjalic, K., Popovac, M., and Hadziabdic, M., "A robust near-wall elliptic-relaxation eddy-viscosity turbulence model for CFD," *International Journal of Heat and Fluid Flow*, Vol. 25, No. 6, 2004, pp. 1047-1051.

[112] Hanjalic, K., and Launder, B. E., "A Reynolds stress model of turbulence and its application to thin shear flows," *Journal of Fluid Mechanics*, Vol. 52, No. 4, 1972, pp. 609-638.

[113] Launder, B. E., Reece, G. J., and Rodi, W., "Progress in the development of a Reynolds-stress turbulence closure," *Journal of Fluid Mechanics*, Vol. 68, No. 3, 1975, pp. 537-566.

[114] Craft, T. J., Launder, B. E., and Suga, K., "Development and application of a cubic eddy-viscosity model of turbulence," *International Journal of Heat and Fluid Flow*, Vol. 12, No. 2, 1996, pp. 108-115.

[115] Gerolymos, G. A., Lo, C., Vallet, I., and Younis, B. A., "Term-by-Term Analysis of Near-Wall Second-Moment Closures," *AIAA Journal*, Vol. 50, No. 12, 2012, pp. 2848-2864.

[116] Wilcox, D. C., *Turbulence Modeling for CFD*, 3rd ed., chapter and pages.

[117] Pope, S. B., "A more general effective-viscosity hypothesis," *Journal of Fluid Mechanics*, Vol. 72, No. 2, pp. 331-340.

[118] Gatski, T. B., and Speziale, C. G., "On Explicit Algebraic Stress Models for Complex Turbulent Flows," *Journal of Fluid Mechanics*, Vol. 254, 1993, pp. 59-78.

[119] Jongen, T., and Gatski, T. B., "General explicit algebraic stress relations and best approximation for three-dimensional flows," *International Journal of Engineering Science*, Vol. 36, No. 7, pp. 739-763.

[120] Prandtl, L., "über Flüssigkeitsbewegung bei sehr kleiner Reibung," *Verhandlinger 3. Int. Math. Kongr*, 1904, pp. 484-491.

[121] Di Pasquale, D., Rona, A., and Garrett, S. J., "A selective review of CFD transition models," *39th AIAA Fluid Dynamics Conference*, AIAA 2009-3812, San Antonio, TX, June 2009.

[122] Tollmien, W., "Grenzschichttheorie," *Handbuch der Experimentalphysik*, Vol. 4, No. 1, Leipzig, Germany, pp. 239-287.

[123] Schlichting, H., "Zur Enstehung der Turbulenz bei der Plattenströmung," *Nachrichten der Gesellschaft der Wissenschaften zu Gottingen, Mathematisch-Physikalische Klasse*, 1929, pp. 21-44.

[124] Orr, W. M., "The Stability or Instability of the Steady Motions of a Perfect Liquid and of a Viscous Liquid, Part I: A Perfect Liquid," *Proceedings of the Royal Irish Academy, Section A: Mathematical and Physical Sciences*, Vol. 27, 1907, pp. 9-68.

[125] Orr, W. M., "The Stability or Instability of the Steady Motions of a Perfect Liquid and of a Viscous Liquid, Part II: A Viscous Liquid," *Proceedings of the Royal Irish Academy, Section A: Mathematical and Physical Sciences*, Vol. 27, 1907, pp. 69-138.

[126] Sommerfeld, A., "Ein Beitrag zur hydrodynamische Erklärung der turbulenten Flussigkeitsbewegungen," *Proceedings of the 4th International Congress of Mathematicians*, Vol. III, Rome, Italy, 1909, pp. 116-124.

[127] Görtler, H., "On the Three-Dimensional Instability of Laminar Boundary Layers on Concave Walls," *NACA TM-1375*, 1954.

[128] Gray, W. E., "The effect of wing sweep on laminar flow," *R.A.E. Technical Memorandum 255*, 1952.

[129] van Ingen, J. L., "A suggested Semi-Empirical Method for the Calculation of the Boundary Layer Transition Region," *Department of Aerospace Engineering, Delft University of Technology, Report VTH-74*, 1956.

[130] Michel, R., "Etude de la Transition et Calcul de la Trainee des Profiles d'aile en Incompressible," *ONERA Publ. 58*, 1951.

[131] Granville, P. S., "The Calculation of the Viscous Drag of Bodies of Revolution," *David W. Taylor Model Basin Report 849, Navy Department,*, 1953.

[132] Abu-Ghannam, B. J., and Shaw, R., "Natural Transition of Boundary Layers: The Effects of Turbulence, Pressure Gradient, and Flow History," *Journal of Mechanical Engineering Science*, Vol. 22, No. 5, 1980, pp. 213-228.

[133] Eppler, R., and Somers, D. M., "A Computer Program for the Design and Analysis of Low-Speed Airfoils," *NASA TM-80210*, 1980.

[134] Steelant, J., and Dick, E., "Modelling of Bypass Transition with Conditioned Navier-Stokes Equations Coupled to an Intermittency Transport Equation," *International Journal for Numerical Methods in Fluids*, Vol. 23, 1996, pp. 193-220.

[135] Steelant, J., and Dick, E., "Modeling of laminar-turbulent transition for high freestream turbulence," *Journal of Fluids Engineering*, Vol. 123, 2001, pp. 22-30.

[136] Menter, F. R., Langtry, R., and Volker, S., "Transition Modelling for General Purpose CFD Codes," *Flow, Turbulence and Combustion*, Vol. 77, 2006, pp. 277-303.

[137] Walters, D. K., and Leylek, J. H., "A New Model for Boundary Layer Transition Using a Single-Point RANS Approach," *Journal of Turbomachinery*, Vol. 126, No. 1, 2004, pp. 193-202.

[138] Coder, J. G., "Enhancement of the Amplification Factor Transport Transition Modeling Framework," *55th AIAA Aerospace Sciences Meeting*, AIAA Paper 2017-1709, Grapevine, TX, January 2017.

[139] Coder, J. G., and Maughmer, M. D., "Computational Fluid Dynamics Compatible Transition Modeling Using an Amplification Factor Transport Equation," *AIAA Journal*, Vol. 52, No. 11 (2014), pp. 2506-2512.

[140] Vieira, B. A. O., Kinzel, M. P., and Maughmer, M. D., "CFD Hover Predictions Including Boundary-Layer Transition," *55th AIAA Aerospace Sciences Meeting*, AIAA Paper 2017-1665, Grapevine, TX, January 2017.

[141] Saric, W. S., Reed, H. L., and White, E. B., "Stability and Transition of Three-Dimensional Boundary Layers," *Annual Review of Fluid Mechanics*, Vol. 35, 2003, pp. 413-330.

[142] Medida, S., and Baeder, J. D., "A New Crossflow Transition Onset Criterion for RANS Turbulence Models," *21st AIAA Computational Fluid Dynamics Conference*, AIAA 2013-3081, San Diego, CA, June 2013.

[143] Saric, W. S., and Yeats, L. G., "Generation of crossflow vortices in a 3-D flat-plate flow," *International Union of Theoretical and Applied Mechanics Laminar-Turbulent Transition Symposium*, pp. 429-437, Novosibirsk, USSR, 1984.

[144] Balch, D. T., and Lombardi, J., "Experimental Study of Main Rotor Tip Geometry and Tail Rotor Interactions in Hover. Vol. I – Text and Figures," *NASA/CR-177336*, 1985.

[145] Jain, R. K., and Potsdam, M. A., "Hover Predictions on the Sikorsky S-76 Rotor using Helios," *52nd AIAA Aerospace Sciences Meeting*, AIAA Paper 2014-0207, National Harbor, MS, January 2014.

[146] Wissink, A., Jain, R., Lakshminarayan, V., and Sitaraman, J., "Automated Meshing Enhancements in HPCMP CREATE^{TM}-AV Helios v10," *AIAA SciTech 2020 Forum*, AIAA 2020-1572, Orlando, FL, January 2020.

[147] Baeder, J. D., Medida, S., and Kalra, T. S., "OVERTURNS Simulations of S-76 Rotor in Hover," *52nd AIAA Aerospace Sciences Meeting*, AIAA Paper 2014-0045, National Harbor, MS, January 2014.

[148] Sheng, C., Wang, J., and Zhao, Q., "S-76 Rotor Hover Predictions Using Advanced Turbulence Models," *53rd AIAA Aerospace Sciences Meeting*, AIAA Paper 2015-1715, Kissimmee, FL, January 2015.

[149] Min, B. Y., Reimann, C. A., Wake, B. E., Jee, S., and Baeder, J. D., "Hovering Rotor Simulation using OVERFLOW with Improved Turbulence Model," *2018 AIAA Aerospace Sciences Meeting*, AIAA Paper 2018-1779, Kissimmee, FL, January 2018.

[150] Jain, R., "Hover Predictions on the S-76 Rotor with Tip Shape Variation Using Helios," *Journal of Aircraft*, Vol. 55, No. 1, 2018, pp. 66-77.

[151] Jain, R., "CFD Performance and Turbulence Transition Predictions on an Installed Model-scale Rotor in Hover," *55th AIAA Aerospace Sciences Meeting*, AIAA Paper 2017-1871, Grapevine, TX, January 2017.

[152] Parwani, A. A., and Coder, J. G., "Effect of Laminar-Turbulent Transition Modeling on PSP Rotor Hover Predictions," *2018 AIAA Aerospace Sciences Meeting*, AIAA Paper 2018-0308, Kissimmee, FL, January 2018.

[153] Parwani, A. A., and Coder, J. G., "CFD Predictions of Rotor-Fuselage Interactions Using Laminar-Turbulent Transition Modeling," *AHS International 74th Annual Forum*, American Helicopter Society, Phoenix, AZ, May 2018.

[154] Sheng, C., Zhao, Q., and Baugher, S., "Numerical Investigation of Rotor Aerodynamics Using High-Order Unstructured Grid Schemes," *AIAA SciTech 2020 Forum*, AIAA 2020-0528, Orlando, FL, January 2020.

[155] Lee, B., Jung, Y. S., Jude, D., and Baeder, J. D., "Turbulent Transition Prediction of PSP Hovering Rotor Using $\gamma - Re_{\theta t} - SA$ with Crossflow Transition Model," *AIAA SciTech 2019 Forum*, AIAA Paper 2019-0286, San Diego, CA, January 2019.

[156] Muller, C., and Herbst, F., "Modelling of Crossflow-induced Transition based on Local Variables," *6th European Conference on Computational Fluid Dynamics*, Barcelona, Spain, July 2014.

[157] Hwang, J. Y., and Kwon, O. J., "Numerical Study of PSP Rotor Blades Using a γ-Re$_{\theta t}$-CF+ Turbulent Transition Model," *AIAA SciTech 2019 Forum*, AIAA Paper 2019-0595, San Diego, CA, January 2019.

[158] Park, S. H., and Kwon, O. J., "Numerical Study of Isolated and Full Configuration PSP Rotor Using a Mixed Mesh Flow Solver," *AIAA SciTech 2020 Forum*, AIAA Paper 2020-0529, Orlando, FL, January 2020.

[159] Tung, C., Caradonna, F. X., and Johnson, W. R., "The Prediction of Transonic Flows On an Advancing Rotor," *Journal of the American Helicopter Society*, Vol. 31, No. 3, 1986, pp. 4-9.

[160] Strawn, R., and Tung, C., "The Prediction of Transonic Loading on Advancing Helicopter Rotors," *NASA TM 88238*, 1986.

[161] Strawn, C., R., Desopper, A., Miller, J., and Jones, A., "Correlation of Puma Airloads - Evaluation of CFD Prediction Methods," *15th European Rotorcraft Forum*, Paper No. 14, September 1989, Amsterdan, Netherlands.

[162] Kim, K. C., Desopper, A., and Chopra, I., "Blade Response Calculations Using Three-Dimensional Aerodynamic Modeling," *Journal of American Helicopter Society*, Vol. 36, No. 1, 1991, pp. 68-77.

[163] Datta, A., Nixon, M., and Chopra, I., "Review of Rotor Loads Prediction with the Emergence of Rotorcraft CFD," *Journal of American Helicopter Society*, Vol. 52, No. 4, 2007, pp. 287-317.

[164] Xu, H., Ye, Z., and Wang, S. A., G., "Simulation of Helicopter Forward Flight Flow Using Unstructured Overset Grids," *47th AIAA Aerospace Sciences Meeting*, AIAA 2009-1285, Orlando, FL, January 2009.

[165] Kim, J. W., Park, S. H., and Yu, Y. H., "Euler and Navier-Stokes Simulations of Helicopter Rotor Blade in Forward Flight Using an Overlapped Grid Solver," *19th AIAA Computational Fluid Dynamics*, AIAA 2009-4268, San Antonio, TX, June 2009.

[166] Potsdam, M., Yeo, H., and Johnson, W., "Rotor Airloads Prediction Using Loose Aerodynamic/Structural Coupling," *Journal of Aircraft*, Vol. 43, No. 3, 2006, pp. 732-742.

[167] Leffell, J. I., Murman, S. M., and Pulliam, T. H., "Time-Spectral Rotorcraft Simulations on Overset Grids," *32nd AIAA Applied Aerodynamics Conference,*, AIAA 2014-3258, Atlanta, GA, June 2014.

[168] Lim, J. W., Nygaard, T. A., Strawn, R., and Potsdam, M., "Blade–Vortex Interaction Airloads Prediction Using Coupled Computational Fluid and Structural Dynamics," *Journal of the American Helicopter Society*, Vol. 52, No. 4, 2007, pp. 318-328.

[169] Jain, R., Yeo, H., and Chopra, I., "Computational Fluid Dynamics–Computational Structural Dynamics Analysis of Active Control of Helicopter Rotor for Performance Improvement," *Journal of the American Helicopter Society*, Vol. 55, No. 4, 2010, pp. 042004-1 - 042004-14.

[170] Anusonti-Inthra, P., "Full Vehicle Simulations for a Coaxial Rotorcraft Using High-Fidelity CFD/CSD Coupling," *2018 AIAA Aerospace Sciences Meeting*, AIAA 2018-0777, Kissimmee, FL, January 2018.

[171] You, Y., Na, D., and Jung, S. N., "Improved rotor aeromechanics predictions using a fluid structure interaction approach," *Aerospace Science and Technology*, Vol. 73, 2018, pp. 118-128.

[172] Bain, J., Potsdam, M., Sankar, L., and Brentner, K. S., "Improved rotor aeromechanics predictions using a fluid structure interaction approach," *American Helicopter Society 66th Annual Forum*, Phoenix, AZ, May 2010.

[173] Overmeyer, A., Heineck, J. T., and Wolf, C., "Unsteady Boundary Layer Transition Measurements on a Rotor in Forward Flight," *American Helicopter Society 74th Annual Forum*, Phoenix, AZ, May 2018.

[174] Coder, J. G., "Standard Test Cases for Transition Model Verification and Validation in Computational Fluid Dynamics," *2018 AIAA Aerospace Sciences Meeting*, AIAA Paper 2018-0029, Kissimmee, FL, January 2018.

[175] Schaeffler, N., Allan, B., Lienard, C., and Le Pape, A., "Progress Towards Fuselage Drag Reduction via Active Flow Control: A Combined CFD and Experimental Effort," *36th European Rotorcraft Forum*, Paris, France, September 2010.

[176] Dagenhart, J. R., Saric, W. S., Mousseux, M. C., and Stack, J. P., "Crossflow-vortex Instability and Transition on a 45-degree Swept Wing," *20th Fluid Dynamics, Plasma Dynamics and Lasers Conference*, AIAA Paper 89-1892, Buffalo, NY, June 1989.

[177] Radeztsky, R. H., Jr., M. S., Reibert, and Saric, W. S., "Effect of Micron-Sized Roughness on Transition in Swept-Wing Flows," *AIAA Paper 1993-0076*, 1993.

[178] Kreplin, H.-P., Meier, H. U., and Maier, A., "Wind Tunnel Model and Measuring Techniques for the Investigation of Three-Dimensional Turbulent Boundary Layers," *10th AIAA Aerodynamic Testing Conference*, AIAA Paper 78-781, San Diego, CA, April 1978.

[179] Kreplin, H.-P., Vollmers, H., and Meier, H. U., "Wall Shear Stress Measurements on an Inclined Prolate Spheroid in the DFVLR 3 m x 3 m Low Speed Wind Tunnel," *Rept. IB 22-84 A 33*, DFVLR-AVA, Göttingen, 1985.

[180] Krimmelbein, N., and Krumbein, A., "Automatic Transition Prediction for Three-Dimensional Configurations with Focus on Industrial Application," *Journal of Aircraft*, Vol. 48, No. 6, 2011, pp. 1878-1887.

[181] Petzold, R., and Radespiel, R., "Transition on a Wing with Spanwise Varying Crossflow and Linear Stability Analysis," *AIAA Journal*, Vol. 53, No. 2, 2015, pp. 321-335.

[182] Nichols, R. H., and Buning, P. G., "User's Manual for OVERFLOW 2.2," NASA Langley Research Center, Hampton, VA, Aug. 2010.

[183] Pulliam, T. H., and Steger, J. L., "Implicit Finite-Difference Simulations of Three-Dimensional Compressible Flow," *AIAA Journal*, Vol. 18, No. 2, 1980, pp. 159-167.

[184] Nichols, R. H., Tramel, R. W., and Buning, P. G., "Evaluation of Two High-Order Weighted Essentially Nonoscillatory Schemes," *AIAA Journal*, Vol. 46, No. 12, 2008, pp. 3090-3102.

[185] Jiang, G.-H., and Shu, C.-W., "Efficient Implementation of Weighted ENO Schemes," *Journal of Computational Physics*, Vol. 126, 1996, pp. 202-228.

[186] Nichols, R. H., Tramel, R. W., and Buning, P. G., "Solver and Turbulence Model Upgrades to OVERFLOW 2 for Unsteady and High-Speed Applications," *AIAA 25th Applied Aerodynamics Conference*, AIAA 2006-2824, San Francisco, CA, June 2006.

[187] Klopfer, G. H., Van der Wijngaart, R. F., Hung, C. M., and Onufer, J. T., "A Diagonalized Diagonal Dominant Alternating Direction Implicit (D3ADI) Scheme and Subiteration Correction," *29th AIAA Fluid Dynamics Conference*, AIAA Paper 1998-2824, Albuquerque, NM, June 1998.

[188] Pulliam, T. H., and Chaussee, D. S., "A diagonal form of an implicit approximate-factorization algorithm," *Journal of Computational Physics*, Vol. 39, No. 2, 1981, pp. 347-363.

[189] Mack, L. M., "Transition and Laminar Instability," *NASA CR-153203*, 1977.

[190] Drela, M., and Youngren, H., "A User's Guide to MISES 2.63," MIT Aerospace Computational Design Laboratory, February 2008.

[191] Spalart, P. R., Deck, S., Shur, M. L., Squires, D., K., Strelets, Kh., M., and Travin, A., "A New Version of Detached-Eddy Simulation, Resistant to Ambiguous Grid Densities," *Theoretical and Computational Fluid Dynamics*, Vol. 20, No. 2, 2006, pp. 181-195.

[192] Hariharan, N., Abras, J., Jain, R., Narducci, B., and Wake, B., "AIAA Rotorcraft Hover Prediction Workshop Website," 2019. URL `https://aiaahover.wixsite.com/website-6/file-share`.

[193] Chan, W. M., Rogers, S. E., Pandya, S. A., Kao, D. L., Buning, P. G., Meakin, R. L., Boger, D. A., and Nash, S. M., "Chimera Grid Tools User's Manual," Moffett Field, CA, 2010.

[194] Hariharan, N., Egolf, A., R., N., and Sankar, L., "Helicopter Rotor Aerodynamic Modeling in Hover: AIAA Standardized Hover Evaluations," *53rd AIAA Aerospace Sciences Meeting*, AIAA Paper 2015-1242, Kissimmee, FL, January 2015.

[195] Meakin, R. L., "Object X-Rays for Cutting Holes in Composite Overset Structured Grids," *15th AIAA Computational Fluid Dynamics Conference*, AIAA Paper 2001-2537, Anaheim, CA, June 2001.

[196] Boger, D. A., and Dreyer, J. J., "Prediction of Hydrodynamic Forces and Moments for Underwater Vehicles Using Overset Grids," *44th AIAA Aerospace Sciences Meeting*, AIAA Paper 2006-1148, Reno, NV, January 2006.

[197] Tecplot, Inc., "Tecplot 360," , 2019. URL `http://download.tecplot.com/360/current/360_users_manual.pdf`.

[198] Vela Software International, "FieldView 18," , 2019. URL `https://fieldviewcfd.com/en/products/fieldview-18`.

[199] Taira, K., Brunton, S. L., Dawson, S. T. M., Rowley, C. W., Colonius, T., McKeon, B. L., Schmidt, O. T., Gordeyev, S., Theofilis, V., and Ukeiley, L. S., "Modal Analysis of Fluid Flows: An Overview," *AIAA Journal*, Vol. 55, No. 12, 2017.

[200] Lumley, J. L., "The Structure of Inhomogeneous Turbulent Flows," *Proceedings of the International Colloquium on the Fine Scale Structure of the Atmosphere and Its Influence on Radio Wave Propagation*, edited by A. M. Yaglam, and V. I. Tatarsky, Doklady Akademii Nauk SSSR, Nauka, Moscow, 1967.

[201] Kajishima, T., and Taira, K., *Computational Fluid Dynamics: Incompressible Turbulent Flows*, chapter and pages.

[202] Murray, N., Sällström, E., and Ukeiley, L., "Properties of Subsonic Open Cavity Flow Fields," *Physics of Fluids*, Vol. 21, No. 9, 2009.

[203] Denison, M., and Pulliam, T. H., "Implementation and Assessment of the Amplification Factor Transport Laminar-Turbulent Transition Model," *AIAA Aviation 2018*, AIAA Paper 2018-3382, Atlanta, GA, June 2018.

[204] Hunt, J. C. R., Wray, A. A., and Moin, P., "Eddies, streams, and convergence zones in turbulent flows," *Proceedings of the 1988 Summer Program*, Center for Turbulent Research Report CTR-S88, pp. 193–208, 1988.

[205] Carnes, J. A., and Coder, J. G., "Computational Assessment of the HVAB Rotor in Hover Using Laminar-Turbulent Transition Modeling," *AIAA SciTech 2019 Forum*, AIAA 2019-0285, San Diego, CA, January 2019.

[206] The MathWorks, Inc., "MATLAB," 2020. URL `https://www.mathworks.com/help/matlab/`.

[207] Jain, R., "Private communication," 2018.

Vita

Jared Carnes was born in 1995 in Dallas, Texas to the parents of Ed Carnes and Teresa Carnes. In 2001, he moved to Franklin, Tennessee and lived there until he graduated high school in 2014. He attended the University of Tennessee, majoring in Aerospace Engineering and minoring in Mechanical Engineering, receiving his Bachelor's Degree summa cum laude in May 2018. He continued his education at the University of Tennessee, graduating with a Master of Science degree in May 2020 under advisor Dr. James Coder. Outside of aerodynamics, Jared enjoys weightlifting, rock climbing, and watching hockey.